



SINGLE STAGE EXPERIMENTAL EVALUATION OF HIGH MACH NUMBER COMPRESSOR ROTOR BLADING PART 1 - DESIGN OF ROTOR BLADING

by

D.R. Seyler and L.H. Smith, Jr.

prepared for

NATIONAL AERONAUTICS AND SPACE ADMINISTRATION

CONTRACT NAS3-7617

N67-2507.8

FACILITY FORM 602

(ACCESSION NUMBER)	(THRU)
83	1
(PAGES)	(CODE)
CR-54581	01
(NASA CR OR TMX OR AD NUMBER)	(CATEGORY)

FLIGHT PROPULSION DIVISION

GENERAL  ELECTRIC

LYNN, MASSACHUSETTS/CINCINNATI, OHIO

NOTICE

This report was prepared as an account of Government sponsored work. Neither the United States, nor the National Aeronautics and Space Administration (NASA), nor any person acting on behalf of NASA:

- A.) Makes any warranty or representation, expressed or implied, with respect to the accuracy, completeness, or usefulness of the information contained in this report, or that the use of any information, apparatus, method, or process disclosed in this report may not infringe privately owned rights; or
- B.) Assumes any liabilities with respect to the use of, or for damages resulting from the use of any information, apparatus, method or process disclosed in this report.

As used above, "person acting on behalf of NASA" includes any employee or contractor of NASA, or employee of such contractor, to the extent that such employee or contractor of NASA, or employee of such contractor prepares, disseminates, or provides access to, any information pursuant to his employment or contract with NASA, or his employment with such contractor.

Requests for copies of this report should be referred to
National Aeronautics and Space Administration
Office of Scientific and Technical Information
Attention: AFSS-A
Washington, D.C. 20546

PRECEDING PAGE BLANK NOT FILMED.

NASA CR-54581
GE R66FPD321

SINGLE STAGE EXPERIMENTAL EVALUATION OF
HIGH MACH NUMBER COMPRESSOR ROTOR BLADING
PART I - DESIGN OF ROTOR BLADING

by

D. R. Seyler and L. H. Smith, Jr.

prepared for

NATIONAL AERONAUTICS AND SPACE ADMINISTRATION

April 1, 1967

CONTRACT NO. NAS3-7617

Technical Management
NASA Lewis Research Center
Cleveland, Ohio
John E. McAulay, Project Manager
Donald M. Sandercock, Research Advisor

ADVANCED TECHNOLOGY AND DEMONSTRATOR PROGRAMS DEPARTMENT
FLIGHT PROPULSION DIVISION
GENERAL ELECTRIC
LYNN, MASSACHUSETTS/CINCINNATI, OHIO

SINGLE STAGE EXPERIMENTAL EVALUATION OF HIGH MACH NUMBER COMPRESSOR ROTOR BLADING

PART I - DESIGN OF ROTOR BLADING

by

D.R. Seyler and L.H. Smith, Jr.

ABSTRACT

A set of four axial-flow medium-aspect-ratio compressor rotor blade rows was designed to provide a vehicle for experimental evaluation of the use of blade camberline shape to minimize blade element losses in the high-transonic Mach number region. One blade row was designed for a tip diffusion factor of 0.35 with a tip blade element ratio of supersonic to total camber of 0. The other three blade rows were designed for a tip diffusion factor of 0.45 with tip ratios of supersonic to total camber varying from 0 to 0.65, the value required for a double-circular arc blade element.

SUMMARY

A set of four axial-flow medium-aspect-ratio compressor rotor blade rows was designed to provide a vehicle for experimental evaluation of the use of blade camberline shape to minimize blade element losses in the high transonic Mach number region. One rotor, designated Rotor 1B, was designed to produce a tip diffusion factor of 0.35 and the other three, designated Rotors 2B, 2D and 2E, were designed to produce a tip diffusion factor of 0.45. Rotor 1B delivers a design total-pressure ratio of 1.60 and the Rotors 2 deliver a design total-pressure ratio of 1.76. The inlet hub-tip radius ratio is 0.50 for all four rotors and all were designed to pass a corrected weight flow of 29.66 lb/sec-sq ft frontal area at a rotor tip speed of 1400 ft/sec. Radially constant total pressure but radially varying losses were used in the construction of velocity diagrams. The loss selections resulted in weight-flow-averaged rotor adiabatic efficiencies of 0.858 for Rotor 1B and 0.837 for Rotors 2. The Rotors 2 were designed for three levels of the ratio of the camber in the front or supersonic portion of the blade element to the total camber. The smallest camber ratio was repeated in the design of Rotor 1B. The aspect ratio for all is about 2.5; part-span shrouds are employed to insure satisfactory aeromechanical performance. The tip diameter of the compressor is 36.5". For this diameter the design weight flow is 215.49 lb/sec. The compressor vehicle was designed to be compatible with the General Electric Lynn Component Test Operation House Compressor Test Stand.

Design parameters were selected for inlet screening to permit the study of effects of inlet flow distortion.

INTRODUCTION

Although early attempts to operate compressors with transonic Mach numbers were disappointing, the potential for substantial increases in stage pressure ratio with transonic compressors stimulated research in this area. In the early 1950's the National Advisory Committee for Aeronautics embarked on an extensive program to develop the performance of transonic compressor stages culminating with the conclusion (ref. 1) that there is no Mach number barrier for axial-flow compressors, but rather a continuous spectrum of performance as design Mach number is increased into the supersonic range.

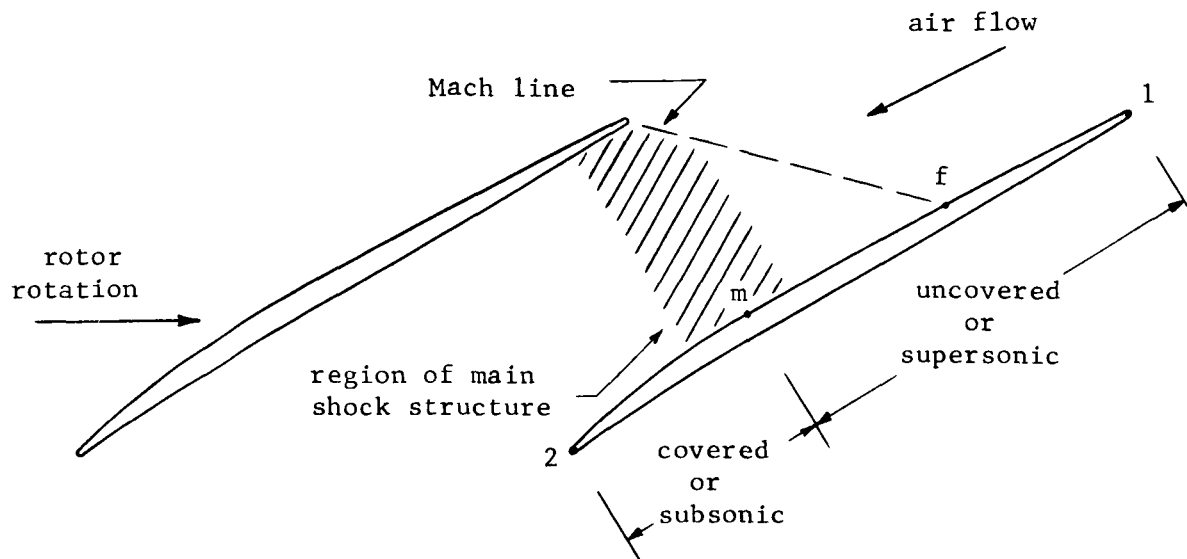
This work and paralleling experiments in the aircraft gas turbine industry led to temporarily accepted design limits for compressor front end stages which acknowledged the observations that:

1. Diffusion factor levels in excess of 0.4 in the rotor tip region are frequently accompanied by high losses.
2. Blade elements with relative Mach numbers in excess of 1.2 have the potential for high losses when simple blade shapes such as the double-circular-arc are employed.
3. Rotor tip solidities of less than 1.0 in conjunction with transonic relative Mach numbers accentuate the loss.

Isolated demonstrations, such as that in reference 2, probed further with reasonable results, but sufficient data and a reasonable model for the design of front stage rotors with tip speeds in excess of 1200 feet per second do not appear in the literature. The purpose of the designs reported herein is to obtain blade element data from rotor blades which operate at high-transonic Mach numbers.

Analyses of the origin of loss in transonic rotors, such as in reference 3, where the shock loss is considered separately from the profile or subsonic diffusion loss result in the observation that the shock loss can be a sizeable fraction of the total loss. Consideration of the relationship between the shock loss and supersonic expansion on the curved uncovered portion of the blade element led to the conclusion that the shape and direction of the suction surface in the uncovered portion plays an important role in minimizing the loss of transonic rotor blade elements.

It appears that, when high-transonic Mach numbers are employed, fundamentally different considerations apply to the selection of the shape of the uncovered forward portion of a blade element and the shape of the covered passage portion behind it. The uncovered portion, identified in sketch 1 as 1-m, may be further subdivided by the point, f, which represents the origin of the first Mach wave from the suction surface that is captured by the adjacent blade. Along the inlet portion, 1-f, expansion and compression waves, when they are



sketch 1

present, must be of such strength that the condition of no change in angular momentum of the flow along any blade-to-blade line forward of the leading edge is satisfied. A principal consideration in the selection of point, m , is the throat area requirement. This area is affected by starting conditions, streamtube contraction, boundary layer allowances and the change in choke flow area that occurs along a streamline because of changing radius in a rotating coordinate system. The shape of the covered portion, $m-2$, of the blade depends upon subsonic diffuser considerations and deviation angle requirements.

Finding the minimum blade element loss for high-transonic rotor blading seems to be most directly related to a search for a blade element shape which provides the best balance between shock loss and subsonic diffusion loss. A new method for developing blade elements, wherein the camberline consists of two circular arcs which are mutually tangent at the point where they join, was employed. The front arc is identified as the supersonic arc, and the rear arc is identified as the subsonic arc. The term, camber ratio, refers to the ratio of the camber of the supersonic arc to the total camber. Blade elements developed in this way are called multiple-circular-arc elements and provide a reasonable means for varying blade shapes between the two extremes of double-circular-arc elements and multiple-circular-arc elements with the smallest supersonic camber consistent with choke-free operation.

For the 0.35 rotor-tip-diffusion-factor design the differences in camberline shape for the extremes approached normal manufacturing tolerances. Therefore only the blade shape approaching the choke limit was designed. For the 0.45 rotor-tip-diffusion-factor design sufficient difference in camberline shape resulted so that the design of two extremes and an intermediate level of camber ratio was warranted. Other design parameter selections are made so that the resulting blade geometry is typical aerodynamically and mechanically of future engine front stage rotor blade rows.

The approach selected for these rotor designs is believed to offer the opportunity for advancement in compressor technology by using:

1. an axisymmetric procedure capable of calculating the flow field throughout the region of the blade row to accurately determine the flow direction at the blade edges and the distribution of meridional streamtube area through the blade row, and
2. blade element shapes of the type described in appendix B, Multiple- and Double-Circular-Arc Properties, where the camberline and surfaces are circular arcs of different curvature in the uncovered or supersonic portion and the covered or subsonic portion of the blade element.

This multiple-circular-arc-blade type is believed to be capable of good performance if the proportions are properly selected.

SYMBOLS

The following symbols are used in this report:

- A exponent in equation (B12), page 26
- A flow area, in²
- a distance along chord line to position where maximum perpendicular displacement between camberline and chord line occurs, in
- C_h enthalpy-equivalent static-pressure-rise coefficient,

$$C_h = \frac{2gJc_p t_1 \left[\left(\frac{p_2}{p_1} \right)^{\frac{\gamma-1}{\gamma}} - 1 \right] - (U_2^2 - U_1^2)}{V_1'^2}$$

C_p	static-pressure-rise coefficient, $C_p = \frac{p_2 - p_1}{p'_1 - p_1}$
c	blade chord length, in
c_p	specific heat at constant pressure, 0.2399 Btu/lb-°R
D	diffusion factor, equation (1), page 15
e	base of natural system of logarithm
F	body force per unit mass, ft/sec ²
f	frequency, cps
g	acceleration due to gravity, 32.174 ft/sec ²
h	displacement along radial direction between axisymmetric stream surfaces, in
i	incidence angle, difference between air angle and camber line angle at leading edge in cascade projection (see Rotor Blade Shape Design section), deg
J	mechanical equivalent of heat, 778.161 ft-lb/Btu
K_{bk}	total effective-area coefficient
K_{bkb}	effective-area coefficient due to blade blockage
K_{bks}	effective-area coefficient due to part-span shroud blockage
K_{bkw}	effective-area coefficient due to wall boundary layer blockage
L	length in cascade projection (see Rotor Blade Shape Design section) defined in appendix C, in
l_z	blade chord length projected to axial direction, in
M	Mach number
m	deviation coefficient, equation (2), page 7, and figure 9, page 54
N	rotational speed, rpm
N_b	number of rotor blades
P	total or stagnation pressure, psia

p	static or stream pressure, psia
R	gas constant, 53.342 ft-lb/lb-°R
r	radius, in
\bar{r}	mean radius, average of streamline leading-edge and trailing-edge radii, in
r_m	radius of curvature of projection of streamline on meridional plane, in
S	entropy, Btu/lb-°R
s	blade spacing, in
T	total or stagnation temperature, °R
t	static or stream temperature, °R
t	blade thickness, in
t_e	blade edge thickness, in; sketch 6 in appendix B
t_m	blade maximum thickness, in
U	rotor speed, ft/sec
u	circumferential displacement defined in equation (B19), page 30, in
V	air velocity, ft/sec
w	weight flow, lb/sec
X	empirical deviation angle adjustment, deg
z	displacement along compressor axis, in
β	air angle, angle whose tangent is the ratio of tangential to axial velocity, deg
γ	ratio of specific heats
γ°	blade-chord angle, angle in cascade projection (see Rotor Blade Shape Design section) between blade chord and axial direction, deg
δ°	deviation angle, difference between air angle and camber line angle at trailing edge in cascade projection (see Rotor Blade Shape Design section), deg

ϵ	meridional angle, angle between tangent to streamline projected on meridional plane and axial direction, deg
θ	angular displacement about compressor axis, deg
η_{ad}	adiabatic efficiency
\vec{i}_k	unit vector in direction of intersection of axisymmetric stream surface and blade mean surface
κ	angle between cylindrical projection of \vec{i}_k and axial direction, deg
λ	lean angle, angle in $z = \text{constant}$ plane between tangent to blade mean surface and radial direction, deg
ρ	static or stream density, $\text{lb-sec}^2/\text{ft}^4$
σ	solidity, ratio of chord to spacing
ϕ	camber angle, difference between angles in cascade projection (see Rotor Blade Shape Design section) of tangents to camberline at extremes of camberline arc, deg
ψ	stream function; $\psi_h = 0$, $\psi_c = 1$
$\bar{\omega}$	total-pressure-loss coefficient
$\bar{\omega}_z$	local loss-rate coefficient, equation (B3), page 24

Subscripts:

a	point on camber line where maximum camber line rise occurs
c	tip or casing at any station
cyl	in cylindrical section of blade
d	design
e	equivalent two-dimensional cascade
h	hub at any station
i	arbitrary axial station
i-1	preceding arbitrary axial station
id	ideal

m meridional direction
 m point on camberline where maximum thickness occurs
 r radial direction
 s suction surface
 sb subsonic or rear portion of blade element
 ss supersonic or front portion of blade element
 t tip at station 1.0
 t total when referring to blade element
 thr location in passage between adjacent blades where area bounded by adjacent blades and adjacent axisymmetric stream surfaces is minimum; appendix C
 z axial direction
 θ tangential direction
 1 leading edge
 1.0 $z = \text{constant}$ plane indicating station at inlet to blade row
 1.5 $z = \text{constant}$ plane indicating station at exit from blade row
 2 trailing edge
 Superscripts:
 * critical flow condition
 ' relative to rotor

ROTOR DESIGN

Overall Design Features

A set of four medium-aspect ratio high-transonic rotors was designed as a vehicle for experimental evaluation of the use of blade camber line shape to minimize blade element losses. All four rotors have some overall characteristics in common as listed below:

1. Rotor tip speed, 1400 ft/sec.
2. Inlet hub-tip radius ratio, 0.50.

3. Rotor inlet tip diameter, 36.5 in.
4. Corrected weight flow, 215.49 lb/sec.
5. Corrected weight flow per unit frontal area, 29.66 lb/sec-sq. ft.
6. Rotor tip solidity, 1.3 with chord radially constant.
7. Number of rotor blades, 44.

Two levels of loading result in differences in some of the overall characteristics as listed below:

	Rotor 1B	Rotors 2
Rotor tip diffusion factor	0.35	0.45
Total-pressure ratio, radially constant	1.60	1.76
Rotor blade aspect ratio	2.5	2.4
Rotor tip axial velocity ratio	.91	.91
Rotor tip relative Mach number	1.43	1.45
Tip blade element camber ratio	1 level	3 levels
Weight-flow averaged rotor adiabatic efficiency	0.858	0.837

The Rotor 1B tip diffusion factor of 0.35 is representative of common practice for stages with an inlet radius ratio of 0.5; the tip Mach number, 1.43, is greater than is commonly used. This combination provides a link with past experience and other current designs where similar diffusion factor levels have been used in conjunction with lower Mach number levels. The selection of the Rotors 2 tip diffusion factor, 0.45, was made with the thought that the diffusion losses associated with a loading level which is somewhat higher than common practice might be tolerable, if the shock losses are minimized. The three levels of the ratio of supersonic to total camber which characterize the difference between the three Rotors 2 are intended to provide a range inside which the minimum blade element loss will occur. One level of camber ratio for Rotor 2 was achieved by selecting double-circular-arc blade elements; the resulting blade is identified as Rotor 2D. The other two levels of camber ratio for Rotors 2 were achieved by using multiple-circular-arc blade elements. Rotor 1B also employs multiple-circular-arc blade elements. All rotors employ double-circular-arc blade elements in the hub region. Because Rotor 2D is a blade composed entirely of double-circular-arc blade elements, it provides a geometric link with past experience. The remaining items were selected as being typical of a fan or compressor front stage, the most likely application of a high-transonic rotor blade. The radial position of the part-span shroud (app. A) is sufficiently far removed from the high Mach number region so as not to interfere with the important blade element measurements. The rotor tip diameter was selected to be compatible with the General Electric Lynn Component Test Operation House Compressor Test Stand. The overall flowpath is shown in figure 1.

Method of Calculation for Rotor Design

The overall calculation procedure used for this design is outlined in Appendix B, Compressor Axisymmetric Flow Determination (CAFD), where the principal equations are listed.

A total of twenty-three calculation stations and ten equal-flow streamtubes were used to arrive at the design vector diagrams in the region of the rotor. Figure 2 shows the location of calculation stations in the neighborhood of the Rotors 2. The first calculation station, 0.1, was located approximately 15" forward of the rotor and the last calculation station, 2.0, was located approximately 15" aft of the rotor (the annulus height at rotor inlet station is 9.125"); the streamline slope and curvature boundary conditions were established at stations 19" forward and 23" aft of the rotor. Two of the calculation stations were located immediately upstream and downstream of the blade axial projection extremities (stations 1.0 and 1.5, respectively) and five additional calculation stations were spaced equally within these extremes. The additional interior stations improve the overall accuracy of the solution by including in fair detail the effects of blade thickness blockage on the slopes and curvatures at the blade inlet and exit stations and thereby enhance the execution of the rotor design.

In the overall CAFD calculation the change in angular momentum is distributed along axisymmetric stream surfaces in the axial space of the blade according to the first quarter cycle of a sine wave raised to the A power (eq. (B12), page 26). In the present design, A was given the value of 1.5. Based on past experience this selection provides a reasonably good representation of the expected rotor work input distribution; it is not a critical selection because the distribution does not have an important influence on the air angles at blade inlet and exit. Distributions of the change in angular momentum along two streamlines from Rotors 2 calculations are shown in figure 3. The dashed line in the region of the leading edge of the blade gives indication of the technique which is used to find modified axial derivatives of angular momentum that are used in the radial-equilibrium equation (eq. (B6)). Modifying the derivatives minimizes the abnormal influence of large changes from point-to-point in the calculation grid.

Effective-Area Coefficient

In application of the CAFD procedure to the present designs, no attempt was made to calculate the localized velocity variations that occur deep in the annulus wall boundary layers. Instead, the calculated free-stream flow distributions were continued to the annulus boundaries. The weight flow used at each station was related to the actual weight flow by an effective-area coefficient, K_{bkw} , that accounts for the displacement thickness of the wall boundary layers. Suitable values for the effective-area coefficient were selected on the basis of past experience; an effective-area coefficient of 0.98 was used at all stations forward of the rotor and 0.95 at all stations aft of the influence of the rotor and the part-span shroud.

At calculation stations where physical obstructions to the flow exist, such as stations internal to a blade row, a modifier must be included in the effective-area coefficient to reflect the reduction of flow area. This modifier is a function of radius since both the circumference and the tangential thickness of the blades are dependent upon radius. The presence of part-span shrouds in these designs was reflected at the internal blade calculation stations by distributing the resulting flow area reduction uniformly across the annulus; this method was judged most appropriate since an unusual and undesirable kink would have resulted from use of concentrated part-span shroud blockage. The blade thickness blockage was distributed radially as it actually occurred, however. The combined effects of boundary layer, blade thickness, and part-span shroud blockage resulted in minimum effective-area coefficients for the internal blade calculation stations varying from 0.85 at the tip to 0.73 at the hub for Rotors 2 and virtually the same values for Rotor 1B. Figure 4 shows the contributions of the three blockages which for a typical case make up the total effective-area coefficient. As is the case with the angular momentum derivatives, the dashed lines in the region of the leading and trailing edge are used to find modified axial derivatives of total effective area coefficient. In these calculations the shroud blockage effect was applied over a larger axial distance than the actual shroud length.

Annulus Shape and Axial Velocities

For given overall design requirements, usually specified by weight flow, pressure ratio, and blade speed, the annulus area is the primary factor in determining the level of axial velocity. When selecting axial velocity levels the following factors must be considered: (1) for a given value of blade loading parameter, such as diffusion factor, a reduction in axial velocity across the rotor tends to reduce the pressure ratio capability of the rotor, (2) a large increase in axial velocity tends to choke the annulus or to pose diffusion problems for succeeding blade rows, and (3) the slopes and curvatures of the casing and hub surfaces can sometimes be used effectively to yield axial velocity profiles that tend to strengthen the traditionally weak blade-end regions. An additional factor for consideration in this design is that the rotor is not immediately followed by a stator. Under this circumstance, annulus choke downstream of the rotor becomes an important consideration. For these designs it was decided that the tip axial velocity ratio should not be less than 0.9.

The hub and casing contours for both Rotor 1B and Rotors 2 annuli were established on the basis of the above considerations. In the course of the design calculations it became clear that it was possible to assign the same casing contour to both Rotor 1B and Rotors 2 and still maintain a reasonable axial velocity change near the casing for both. Accordingly as is seen in figure 1 only the hub contour is different for the two rotor types. Figure 2 is an enlargement of the flowpath in the neighborhood of the rotor. Included in this figure, for reference purposes, are the streamlines obtained from the design calculations for Rotors 2.

Total-Pressure Ratio and Loss Coefficients

The selection of diffusion factor, solidity, inlet relative velocity and, from the preceding section, axial velocity ratio permits calculation for the rotor tip of the change in angular momentum across this section of the rotor. The change in angular momentum and a suitable rotor total-pressure-loss coefficient determine the rotor total-pressure ratio. The total-pressure ratio was maintained constant over the radial height of the blade. The equations used for these calculations are given in reference 4, except the following definition of diffusion factor was used:

$$D = 1 - \frac{V'_2}{V'_1} + \frac{r_2 V_{\theta 2} - r_1 V_{\theta 1}}{2 \bar{r} \sigma V'_1} \quad (1)$$

This form is preferred when there is a change in radius as the flow passes through a blade row.

The profile loss portions of the rotor total-pressure-loss coefficients used in the CAFD calculations were determined from the loss correlation (ref. 4) which is the object of additional development at NASA Lewis Research Center. In reference 4 it is demonstrated that losses from rotor tests for all radial immersions except the immersion ten-percent from the tip correlate reasonably well on diffusion factor when the total-pressure-loss parameter is used. Data at the ten-percent immersion above a diffusion factor of 0.25 scatters over a wide range of total-pressure-loss parameter. The designer has the choice of selecting values within this broad band of variation. The minimum level of the total-pressure-loss parameter band for ten-percent immersion was used to guide the selection of tip profile losses for all rotors. Additive shock losses were calculated by the NASA method given in reference 3. The diffusion factors and Mach numbers used to calculate the total-pressure-loss coefficients were taken from immediately preceding CAFD rotor design calculation and were therefore slightly different from those calculated in the final design. Figure 5 shows the radial distributions of rotor total-pressure-loss coefficient that were employed. For Rotors 2 one loss curve was used to simplify the design calculations. As will be shown in a later section reasonable radial distributions of adiabatic efficiency and diffusion factor resulted from these assumptions.

Because it was decided to wash out the blockage influence of the part-span shroud downstream of the blade in a manner typical of the dissipation of a wake, it is necessary to provide some indication of the associated mixing loss. At the first calculation station, 1.54, where the part-span shroud blockage no longer exists a total-pressure loss was introduced. The loss was determined by use of the compressible dumping loss coefficient associated with the two percent change in the effective area of the shroud and the compressible velocity head at calculation station 1.5. The loss was distributed uniformly from hub to tip. Accordingly, the part-span shroud loss did not influence the shape of the rotor blading.

Rotor Blade Shape Design

Constant-chord rotors employing multiple-circular-arc blade elements in the tip region and double-circular-arc blade elements in the hub region were selected to fulfill the requirements of these designs. The camberline of a multiple-circular-arc element consist of two circular arcs which are mutually tangent at the point where they join. The method of development of the multiple-circular-arc elements used in these designs is described in appendix B, Multiple- and Double-Circular-Arc Properties. The front arc is identified as the supersonic arc and the rear arc is identified as the subsonic arc. Geometric description of the double-circular-arc elements follows the customary procedure of using one circular arc to represent the camberline and circular arcs of different radii, tangent to the maximum thickness and edge thickness circles, to form the surfaces. The center of the maximum thickness circle is located on the camberline mid-way between the leading and trailing edges. Distributions of the ratio of supersonic to total camber are shown in figure 6. Multiple-circular-arc-type elements extend inward to the radial location where the radii of the supersonic and subsonic arcs are equal. This radial location very nearly corresponds to the location of the part-span shrouds. Double-circular-arc-type elements are employed in the remaining radial length. Rotor 2D is composed of double-circular-arc-type elements along its entire radial length.

The design of the rotor elements was performed along axisymmetric stream surfaces using the projection recommended in reference 5. This projection cuts the blades along the axisymmetric surfaces but views the cut sections along a radial line. The incidence and deviation angles are defined in this projection (identified as the cascade projection) and the resulting blade angles are termed cascade angles.

The blade designs were based on the vector diagrams at the edges. In the hub region the inlet and exit calculation stations (1.0 and 1.5 in figure 2) are reasonably close to the leading and trailing edges. In the tip region however the edges are removed from the calculation stations by as much as twenty percent of the axial distance between the inlet and exit stations. The importance of properly accounting for this displacement will be seen later in this section. Rotor 1B design data is listed in table 1; Rotors 2 design data are listed in tables 2, 3 and 4. Although only one overall CAFD calculation was performed for Rotors 2, individual vector diagrams were established for each Rotor 2 type depending upon the axial position of each in the annulus. These differences are observed when comparing the data in tables 2, 3 and 4.

Design incidence angles were generally selected on the basis of past experience but subject to the additional criterion that the blade throat be adequate to preclude the condition of choking. The rotor geometry was checked for choking according to the method described in appendix C, Throat Area Parameter. In regions of elevated design inlet relative Mach number, it was intended that the design incidence angle be calculated according to the condition that the

suction surface angle at the leading edge be parallel to the upstream flow direction. When Rotor 2B was set according to this criterion and checked for choking, it was found that in the tip region less than 1% margin in throat area existed over the critical area associated with one normal shock at the upstream Mach number. In view of the uncalculated real flow effects this margin was judged to be insufficient to pass the design flow and accordingly the design incidence was increased. When the calculated design incidence for Rotor 2D was applied to Rotor 2B the margin shown in figure 7(a) resulted, and accordingly it was decided to use the Rotor 2D design incidence distribution to set the leading edge direction in the tip and pitch regions for all Rotors 2. Similar results were encountered when Rotor 1B tip blade elements were set to the desired incidence criterion and the design incidence for Rotor 1B was likewise increased to that level which would have been used if a rotor had been designed with double-circular-arc sections to the loading level of Rotor 1B. Figure 7(b) shows the final choke check results for Rotor 1B.

In the hub region, where the design inlet relative Mach number is near sonic, blade element losses are almost entirely related to diffusion requirements, and setting the suction surface at the leading edge parallel to the upstream flow direction is not a meaningful criterion. Design incidence angles were lowered to avoid excessive leading edge loading but limited by the additional consideration that the throat area be large enough to pass the design flow. The throat area ratio margin for the hub elements was selected to be about the same as the smallest margin for the tip elements.

The tabulations of blade setting data (tables 1 through 4) list the differences in direction, $\kappa'_{s1} - \kappa'_1$, between the camberline and the suction surface

at the leading edges. The incidence angles employed in these designs are shown in figure 8.

The deviation angles were obtained by applying an extension of Carter's Rule (fig. 9). The two curves in figure 9 for the positions of maximum camberline rise at forty and fifty percent of chord length are extracted from Carter's correlation of cascade data in reference 6. The three other curves were constructed by laying off at any blade-chord angle three increments in deviation coefficient equal to the increment between the forty percent and fifty percent curves. For each blade element an equivalent two-dimensional cascade was defined as is discussed in appendix B, Blade Setting. The deviation coefficient, m , was obtained from figure 9 using the blade-chord angle and position of maximum camberline rise of the actual cascade. The deviation angle was calculated from the camber of the equivalent two-dimensional cascade.

$$\delta^\circ = \frac{\beta'_1 - i - \beta'_{2e}}{\frac{\sqrt{\sigma}}{m} - 1} + X \quad (2)$$

The empirical adjustment, X , which is shown with the resulting deviation angles in figure 10 is derived from experience with aerodynamic design and performance synthesis for this general type of rotor.

Some pertinent design data which summarize the results of the final overall CAFD calculations appear in figures 11 through 15 for Rotor 1B and in figures 16 through 20 for Rotors 2. Solid lines indicate edge conditions and broken lines indicate station conditions. Examination of the graphs gives indication of the importance of properly accounting for the displacement between the stations and the edges. As an illustration, for Rotor 1B the relative inlet air angle at the blade edge is up to two degrees different from that at calculation station 1.0 (fig. 13). The difference in design data (tables 2, 3 and 4) for Rotors 2 are small enough so that with the scales selected they cannot always be clearly indicated in the graphs. Some indication of the design requirements for a stationary blade row to follow close onto the designed rotors is given in the graphs of absolute air conditions at the rotor exit calculation station (figs. 21 and 22).

A layout on a cascade projection of a typical blade element from Rotor 2B is shown in figure 23. A portion of the pressure surface of the next blade in the counter-rotor-wise direction is included; this surface at any axial location is constructed with the correct circumferential displacement and its shape is therefore not identical with that of the first blade. The construction of the throat width and upstream capture width which is performed to arrive at the Throat Area Parameter is included. Although this method of throat area determination is approximate, studies have shown that it is quite accurate except when the meridional angle, ϵ , is very large and the number of blades is very small.

The radial distributions of adiabatic efficiency (fig. 24) are obtained directly from the overall CAFD calculations. But in keeping with the planned method for reduction of aerodynamic test data, where measured quantities will be corrected from the measurement planes to the blade edges, radial distributions of other performance indicators, diffusion factor, axial velocity ratio, relative turning angle, static-pressure-rise-coefficient and enthalpy-equivalent static-pressure-rise-coefficient (figures 25 through 29), were calculated from the design vector diagrams at the edges.

The multiple-circular-arc and double-circular-arc blade elements were specified in the cascade projection and the conversion from this projection to cylindrical sections was accomplished by means of the calculation routine which is discussed in appendix B, Special Airfoil Generator. Figure 30 is included to reveal the difference between cylindrical and cascade blade-edge angles for a typical case. In the hub region, differences as large as 3.5 degrees occur, and thereby illustrate the importance of using the cascade projection.

For the purpose of manufacturing the blading, the developed cylindrical sections are interpreted as plane sections normal to the stacking axis, since the error involved is negligible.

TEST VEHICLE

Inlet Ducting

The conditions of zero inlet swirl and moderately thin casing boundary layer require incorporation of a flow straightener in the vehicle inlet and provision for a large area contraction into the test vehicle; see figure 1. The flow straightener has honeycomb type cells which are approximately equivalent to a 7/8" diameter; the length of the cells is 8". An incompressible axisymmetric flux plot of the inlet contraction region yields the casing velocity distribution shown in figure 31; the presence of the four struts was ignored for purposes of this calculation. The lack of adverse velocity gradients on both walls suggests conditions conducive to healthy boundary layers.

Outlet Guide Vanes

The same set of outlet guide vanes (figure 1) which was designed for the Contract NAS3-7618 vehicle (ref. 7) will be used for this vehicle. Since the performance of the rotor is of primary interest, the purpose of the outlet guide vane system is to remove swirl and decrease Mach number so that the exhaust system pressure drop will be minimized when the discharge Mach number is high. The outlet guide vanes were designed to the calculations which were performed as a part of the Contract NAS3-7618 design. Check calculations were performed, and it was determined the outlet guide vane design performed under Contract NAS3-7618 would fulfill the needs of the test vehicle for Rotor 1B and Rotors 2. Since the outlet guide vanes have variable stagger, any problems associated with their high incidence operation on the high-pressure part of the characteristic can be readily eliminated.

The outlet guide vane sections employ a modified NACA 65-series thickness distribution and a circular-arc camberline. The hub solidity is 1.4, and the chord is constant radially. The aspect ratio is approximately 2.

Distortion Screens

Radial and circumferential distortion screens were designed to provide a total-pressure loss of 15% at the rotor inlet instrumentation station. The circumferential screen will cover a 90° arc of the inlet annulus while the radial screen will cover the outer 40% of the inlet annulus. The solidity of the screens for both types of distortion was determined to be 0.54. This value of solidity was arrived at utilizing test data of reference 8 which approximates the desired design, and a correlation of screen total-pressure-loss coefficient with screen solidity and screen inlet Mach number (ref. 9).

A screen with approximately 0.016 inch wire diameter and 20 mesh will provide the required 0.54 solidity. These distortion screens will be supported by a screen covering the entire annulus whose wire diameter is about 0.092 inches and which has a 3/4 inch mesh.

APPENDIX A

ROTOR BLADE AEROMECHANICAL CONSIDERATIONS

by

P. Chifos and C.E. Danforth

Summary

The selected configuration for these rotors, titanium blading of aspect ratio of about 2.5 with part-span shroud at about 60-percent blade height, gives the most reasonable expectation of fulfilling the aeromechanical design objectives. Designs without part-span shrouds would have required aspect ratios as low as 1.5. Although the reduced velocities* for the selected designs are in the range of reduced velocities for current blading operating successfully in General Electric engines, it is possible that self-excited blade vibration may be encountered in the 80-percent design speed region before stall is attained while the test vehicles are operated with circumferential inlet distortion.

Resonant Vibration

Two aeromechanical considerations governed the selection of the rotor blade designs:

1. The avoidance of two per-rev resonance with the first flexural frequency of the blades at high speed.
2. The attempt to guard against self-excitation as the incidence angle increases when stall is approached.

While it is usually desirable to avoid integral order per-rev resonance in the low per-rev range and occasionally even higher order per-rev resonance, the avoidance of two per-rev resonance with the first flexural mode is generally mandatory for engine designs and for research vehicles which must be operated with circumferential distortion. Inlet systems for aircraft engines frequently

*(Velocity relative to the blade/semi-chord times torsional frequency), dimensionless, varies approximately inversely with aspect ratio.

deliver one per-rev and two per-rev distortions, either of which can excite the first flexural vibration modes. The avoidance of two per-rev resonance may be achieved in either of two ways:

1. Design for two per-rev flexural resonance at low speeds where excitation energy levels are correspondingly low, obtaining a blade with natural frequency at high speed between one- and two-per-rev. There are such designs which are currently successful. Aspect ratios are moderately high.
2. Design to have a first flexural frequency above the two per-rev with adequate margin at high speeds, a result achieved by use of low aspect ratios or of moderate-to-high aspect ratios with shrouding of an appropriate type.

There are compromises in each approach. The low-speed resonance approach with correspondingly appreciable aspect ratios is workable only if the aerodynamic environment has been especially tailored to avoid those conditions conducive to instability in the comparatively high reduced velocity levels that naturally follow. The second approach of exceeding two per-rev frequencies demands a comparatively low aspect ratio (flexural frequency going up approximately as the chord) and a weight/size penalty.

But the low aspect ratio achieving the flexural frequency margin over two per-rev carries with it a reduction in the reduced velocity which increases the design's incidence migration range that is free from instability. However, for the present aerodynamic designs this second approach would require an aspect ratio of about 1.5 with a conventional dovetail and no shrouding. Designs to the originally desired aspect ratio of three (3) imply the need for shrouding.

After it became clear that part-span shrouds should be considered, parametric studies were made to assess the desirable spanwise location for the shroud. Figure 32 illustrates the choices available to avoid integral order resonance with the first flexural frequency. Resonance with two per-rev excitation is not a problem for any reasonable shroud location. The proposed Rotor 1B design yields a first flexural frequency at about 3.6 per-rev at design speed (1400 ft/sec tip speed, 8791 rpm). Campbell diagrams are shown in Figures 33 and 34 for Rotors 1B and 2B, respectively.

Self-Excitation

A detailed examination of torsional frequency and corresponding reduced velocity variation was made for aspect ratios 3.0 and 2.5. Primary emphasis was placed on Rotor 1B which, because of its lower root camber and higher aspect ratio, has the lowest torsional frequencies. Whereas at 80-percent design speed, where the incidence margin appears to be the smallest, the aspect ratio 3.0 design yielded a 1° incidence margin between clean inlet stall and self-

excitation, the aspect ratio 2.5 design results in a 3° incidence margin. Because of the necessity to operate with inlet distortion and the unavoidable blade-to-blade manufacturing differences, the aspect ratio 3.0 design was considered too risky. The aspect ratio 2.5 design was chosen.

Steady Stress and Material Selection

Calculations listed in Table 5 point clearly to the use of the titanium alloy, 6Al-4V-Ti, which has the greatest service experience, on the basis of the following considerations:

1. Part-span shroud restraint and the resulting root warping stress together with the stress components due to centrifugal and air loads combine to produce an untilted root edge stress of approximately 100,000 psi for steel, practically the yield point for typical blading material such as 403 stainless. This is an unreasonable choice in the event that any unanticipated vibration or malfunction be encountered. Calculations indicate an untilted root edge stress of 69,000 psi for titanium, which has a yield strength of 111,000 psi. This stress reduces to 13,500 psi for Rotor 1B with tilting, as is shown in Table 5.
2. High tip speed and the related large blade pull makes the blade dovetail design difficult with steel but relatively straightforward with titanium which has about the same strength but only 56% of the dead load.
3. Elastic untwist and outer panel (the portion outside of the part-span shroud) stall stress without resonance appear to be acceptable.

APPENDIX B

DIGITAL COMPUTER PROGRAMS USED IN DESIGN

Compressor Axisymmetric Flow Determination (CAFD)

The name, Compressor Axisymmetric Flow Determination, and the abbreviation for it, CAFD, refer to a digital computer program which describes the axisymmetric flow field in the region of turbomachinery blading.

The overall calculation scheme may be summarized as follows: The flow is considered at a number of axial stations ($z = \text{constant}$ planes), and the radial-equilibrium equation, energy equation, and continuity condition are employed at each of them to determine the distribution of flow properties from hub to casing. It is necessary, however, that these distributions obtained separately

at each station be consistent from station to station and that the radial acceleration which a fluid particle undergoes as it passes from station to station be accounted for in the radial-equilibrium equation. This is done by assuming that the shape of a meridional streamline is adequately represented by a spline constrained at each axial station consistent with the continuity condition and at upstream and downstream boundary stations by a selected orientation and shape. The radial acceleration is expressed in terms of the meridional streamline slope and curvature.

An iterative method of solution is implied. Meridional streamline shapes are assumed based on results from the previous iteration and flow distributions at each axial station are found. These imply new meridional streamline shapes, and this iterative calculation is allowed to continue until the changes in streamline shapes between two successive calculations are small enough to satisfy the user.

An interesting feature of the computer program is the inclusion of terms in the radial-equilibrium equation which represent the blade action by a distributed body force field and the blade thickness by distributed blockage. The equation, which appears in reference 10, wherein physical interpretation of the individual terms is rendered, is restated here:

$$\frac{144}{\rho} \frac{\partial p}{\partial r} = \frac{1 - M_z^2}{1 - M_m^2} \left(\frac{V_\theta^2}{r} - \frac{D^2 r}{Dz^2} V_z^2 \right) + \frac{V_r V_z}{1 - M_m^2} \left[\frac{\partial(r \tan \epsilon)}{r \partial r} + \frac{1}{K_{bkb}} \frac{DK_{bkb}}{Dz} \right] - \frac{F_\theta}{12} \frac{M_r M_\theta}{1 - M_m^2} + \frac{F_r}{12} \quad (B1)$$

The heat addition term has been omitted since it does not appear in compressor design: in the absence of transients the blade surface and the fluid adjacent to it are at the same temperature.

It is suggested (ref. 10) that a term be added to represent the heating effect of internal fluid friction, which encompasses all loss sources including shock waves:

$$- \frac{V_r V_z}{1 - M_m^2} \left(1 - \frac{p}{p'} \right) \frac{\bar{\omega}'_z}{1_z} \quad (B2)$$

The loss-rate coefficient, $\bar{\omega}'_z$, is defined as follows:

$$\bar{\omega}'_z = - \frac{1}{P - p} \frac{z}{Dz} \left(\frac{DP'}{Dz} - \frac{DP'_{id}}{Dz} \right), \quad (B3)$$

and is distinguished from the loss-coefficient, $\bar{\omega}'$, in that the loss-rate coefficient is concerned with the manner in which the entropy increases inside of the blade row whereas the loss coefficient merely acknowledges that the entropy has increased across the blade row.

The radial and tangential components of the blade force may be expressed in terms of the axial change in angular momentum by means of the following relationships:

$$F_\theta = 12 \frac{V_z}{r} \frac{D(rV_\theta)}{Dz}, \quad (B4)$$

$$\text{and} \quad F_r = F_\theta \tan \lambda. \quad (B5)$$

By using the fact that the second derivative of the meridional streamline shape can be related to the meridional streamline curvature, $\frac{1}{r_m}$, and trigonometry to relate velocity components, equation (B1) may be rewritten as follows:

$$\begin{aligned} \frac{144}{\rho} \frac{\partial p}{\partial r} = \frac{1 - M_z^2}{1 - M_m^2} \left\{ \frac{V_\theta^2}{r} + \frac{V_z^2 \sec^3 \epsilon}{r_m} + \frac{V_z^2 \tan \epsilon}{1 - M_z^2} \left[\frac{\partial(r \tan \epsilon)}{r \partial r} - \left(1 - \frac{p}{P'} \right) \frac{\bar{\omega}'_z}{\Delta z} \right] \right\} \\ + \frac{1}{1 - M_m^2} \left\{ V_z^2 \tan \epsilon \frac{1}{K_{bkb}} \frac{DK_{bkb}}{Dz} + \left[M_z^2 (U - V_\theta) \tan \epsilon \right. \right. \\ \left. \left. + (1 - M_m^2) V_z \tan \lambda \right] \frac{1}{r} \frac{D(rV_\theta)}{Dz} \right\}. \quad (B6) \end{aligned}$$

The particular grouping of terms on the right-hand side of equation (B6) is intentional: the first braces include terms which are present anywhere in the flow field while the second braces include terms which occur only when calculations inside the axial extent of a blade row are desired. The attention of the reader is again invited to reference 10 where a numerical example illustrates the relative magnitude of each term in equation (B6).

At each axial station where the rotating blade row is influential the enthalpy of the fluid is related to the fluid swirl velocity by the energy equation which may be found in reference 11:

$$(UV_{\theta})_i - (UV_{\theta})_{i-1} = gJc_p (T_i - T_{i-1}) , \quad (B7)$$

where

$$T = t + \frac{v^2}{2gJc_p} . \quad (B8)$$

The static condition of the fluid is described by use of the equation of state,

$$p = \frac{1}{144} g \rho R t , \quad (B9)$$

and the specific heats are assumed to be constant. Application of the continuity condition in the form which may also be found in reference 11,

$$w = \frac{2\pi g}{144} \int_{r_h}^{r_c} K_{bk} \rho V_z r dr , \quad (B10)$$

in combination with the previous four equations yields a complete description of the flow at each axial station.

Because a form of the radial-equilibrium equation employing static pressure was used, an entropy gradient term does not appear explicitly. The entropy variations that result from radially non-constant losses are correctly accounted for, however, through the use of

$$\frac{T_i}{T_{i-1}} = \left(\frac{p_i}{p_{i-1}} \right)^{\frac{\gamma-1}{\gamma}} e^{\frac{S_i - S_{i-1}}{c_p}} , \quad (B11)$$

which results from the definition of entropy and the assumption of a perfect gas.

With the flow field completely described, loading parameters, such as diffusion factor and static-pressure-rise coefficient, and forces on the blading and walls are calculated from station data using geometric characteristics of the system where required.

Intra-Blade Energy Distribution (IBED)

This digital computer program provides the stagnation pressure and temperature and the derivative of the product of radius and tangential velocity with respect to the axial direction along a streamline at desired axial locations in the region of a rotor blade row. The upstream and downstream stagnation pressure and temperature and the axial locations of the blade edges are specified. The axial variation of energy addition is calculated according to the following equation:

$$\frac{rV_{\theta} - r_1V_{\theta 1}}{r_2V_{\theta 2} - r_1V_{\theta 1}} = \sin^A \left[\frac{\pi}{2} \left(\frac{z - z_1}{z_2 - z_1} \right) \right], \quad (B12)$$

which allows analytical evaluation of the axial derivative of energy addition,

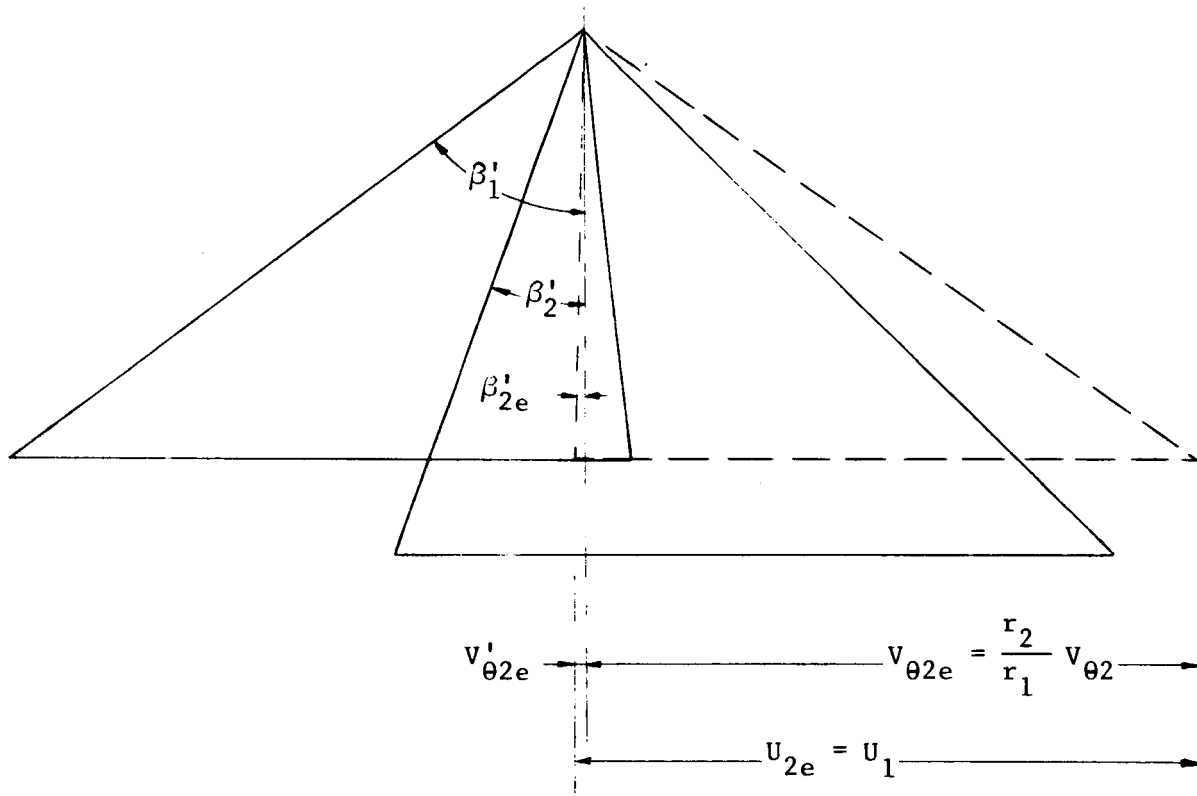
$$\begin{aligned} \frac{d(rV_{\theta})}{dz} = A \frac{\pi}{2} \frac{r_2V_{\theta 2} - r_1V_{\theta 1}}{z_2 - z_1} \sin^{A-1} \left[\frac{\pi}{2} \left(\frac{z - z_1}{z_2 - z_1} \right) \right] \\ \cos \left[\frac{\pi}{2} \left(\frac{z - z_1}{z_2 - z_1} \right) \right]. \end{aligned} \quad (B13)$$

The stagnation temperature is determined from the energy equation, (B7), and the stagnation pressure is found by assuming a constant polytropic efficiency at the value associated with the downstream pressure and temperature. The value of A is selected from past experience to give a representative rate of energy addition consistent with expected blade surface velocity distributions.

Blade Setting (BLAST)

In this blade setting procedure, after the axisymmetric flow field is established and the incidence and blade solidity are selected, the camberline orientation is calculated using Carter's correlation (ref. 6). When changes in radius and axial velocity are present along a streamline across a blade row, the deviation angle is found by using the camber which is derived from an equivalent two-dimensional cascade of the same absolute circulation as is required along the streamline.

Sketch 2 shows a typical velocity diagram. The exit velocity diagram of the equivalent two-dimensional case appears in dashed lines. For the equivalent diagram to have the same circulation as the actual diagram, the equivalent absolute tangential velocity must be larger than the actual absolute tangential velocity by the ratio of the exit radius to the inlet radius.



sketch 2

Addition of vectors in the tangential direction results in the following statement:

$$v'_{\theta 2e} = U_1 - \frac{r_2}{r_1} v_{\theta 2} \quad (B14)$$

By substitution of the velocity diagram relationships,

$$V_{\theta} = U - V_z \tan \beta' \quad , \quad (B15)$$

and

$$V_z \tan \beta' = V_{\theta}' \quad , \quad (B15a)$$

and rearrangement, an expression relating the equivalent and actual relative fluid exit angles is obtained:

$$\beta'_{2e} = \arctan \left[\frac{U_1}{V_{z1}} - \frac{r_2}{r_1} \left(\frac{U_2}{V_{z1}} - \frac{V_{z2}}{V_{z1}} \tan \beta'_2 \right) \right] \quad . \quad (B16)$$

When stators are calculated the absolute fluid angle relationship is obtained by setting the wheel speed to zero.

Carter's formula,

$$\delta^{\circ} = \frac{m \phi_e}{\sqrt{\sigma}} \quad , \quad (B17)$$

may be expressed in terms of relative fluid angles and the incidence angle as follows:

$$\delta^{\circ} = \frac{\beta'_1 - i - \beta'_{2e}}{\frac{\sqrt{\sigma}}{m} - 1} \quad . \quad (B18)$$

The unguided portion of the fluid at the exit of the cascade is more closely related to the actual blade-chord angle than the blade-chord angle of the equivalent cascade and therefore the deviation coefficient, m , is determined by entering the functional relationship (shown graphically in figure 10) with the actual blade-chord angle. The trailing edge angle is calculated by application of the deviation angle from equation (B18) to the actual fluid exit angle. Iteration is required to arrive at the correct deviation coefficient. The iterative calculation is stopped when the blade-chord angle from the successive calculations differs by less than 0.01 degrees.

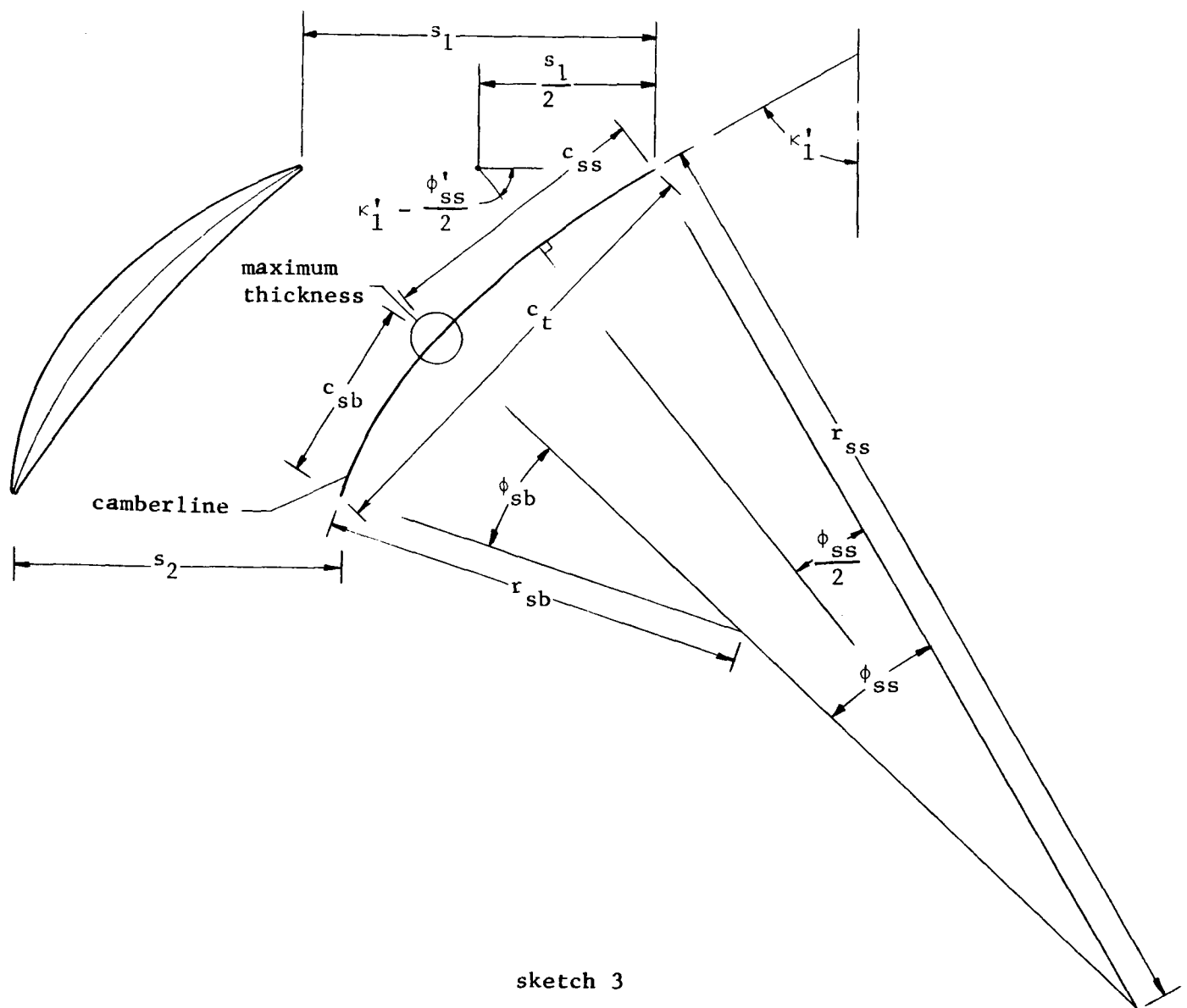
Occasionally, past experience suggests the need for additional allowance in deviation angle, and an empirical adjustment, X , is provided in equation (B18). The form used in this design is given in equation (2).

Multiple- and Double-Circular-Arc Properties (MADCAP)

For input to the Special Airfoil Generator computer program (described later in this Appendix) an accurate description of the blade camberline shape and thickness distribution is required. The MADCAP computer program provides for determination of the point at which two circular arcs join when multiple-

circular-arc blade elements are selected. In addition, the direction of the camberline and the circumferential displacement of the camberline are calculated at preselected axial locations. After the trailing edge is located, the blade-chord angle is calculated. The angle between the camberline and the suction surface at the leading edge and the position along the chord line at which the maximum rise of the camberline occurs (in percent of chord) are also calculated.

A section through a blade (sk. 3) is obtained by cutting the blade along a stream surface but viewing it in the radial direction as recommended in



sketch 3

reference 5. This is called the cascade projection. The circumferential displacement of any point on the camberline from the leading edge in the cascade projection is defined as follows:

$$u = \int_{\theta_1}^{\theta} r d\theta \quad . \quad (B19)$$

In sketch 3 and other sketches in this section u is measured perpendicular to the compressor axis in the plane of the paper.

The camberline of a multiple-circular-arc blade is made up of two circular arcs in this projection. The maximum thickness exists at the point where the two arcs join. The camber bisector of the forward or supersonic portion intersects the line of leading edges at a point midway between adjacent leading edges as shown.

From knowledge of the inlet and exit air angles, the incidence angle and a tentative deviation angle, the leading edge direction, κ'_1 , and the total camber, ϕ_t , are found. The value of camber ratio, $\frac{\phi_{ss}}{\phi_t}$, is specified and the total chord, c_t , and leading edge spacing, s_1 , are known from preliminary design selections. The camber of the supersonic and subsonic portions are found simply by multiplication and subtraction. The chord of the supersonic portion may then be found from

$$c_{ss} = s_1 \sin \left(\kappa'_1 - \frac{\phi_{ss}}{2} \right) \quad . \quad (B20)$$

By application of the law of cosines the subsonic chord may be found from

$$c_{sb} = \left[c_{ss}^2 \cos^2 \left(\frac{\phi_{ss}}{2} + \frac{\phi_{sb}}{2} \right) + c_t^2 - c_{ss}^2 \right]^{\frac{1}{2}} - c_{ss} \cos \left(\frac{\phi_{ss}}{2} + \frac{\phi_{sb}}{2} \right) \quad . \quad (B21)$$

With the supersonic and subsonic chords calculated the radii of both arcs may be found from

$$r_{ss} = \frac{c_{ss}}{2 \sin \frac{\phi_{ss}}{2}} \quad (B22)$$

and

$$r_{sb} = \frac{c_{sb}}{2 \sin \frac{\phi_{sb}}{2}} \quad (B22a)$$

When double-circular-arc blade elements are selected, specification of the value of camber ratio, $\frac{\phi_{ss}}{\phi_t}$, is not required; it can be determined from the observation that the radius of the camberline is the same in both the supersonic and subsonic portions of the blade element,

$$r_{ss} = r_{sb} = \frac{c_t}{2 \sin \frac{\phi_t}{2}} \quad (B22b)$$

and the use of equations (B20) and (B22):

$$\frac{\phi_{ss}}{\phi_t} = \frac{2}{\phi_t} \arctan \frac{s_1 \sin \kappa'_1 \sin \frac{\phi_t}{2}}{c_t + s_1 \cos \kappa'_1 \sin \frac{\phi_t}{2}} \quad (B23)$$

The camber angles of the supersonic and subsonic portions may be found simply by multiplication and subtraction, and the supersonic and subsonic chords may be found from rearrangement of equations (B22) and (B22a).

The blade-chord angle of the blade element is the direction of the chord line, a straight line passing through the leading edge and trailing edge points, with respect to the axis of the compressor, and is found as follows:

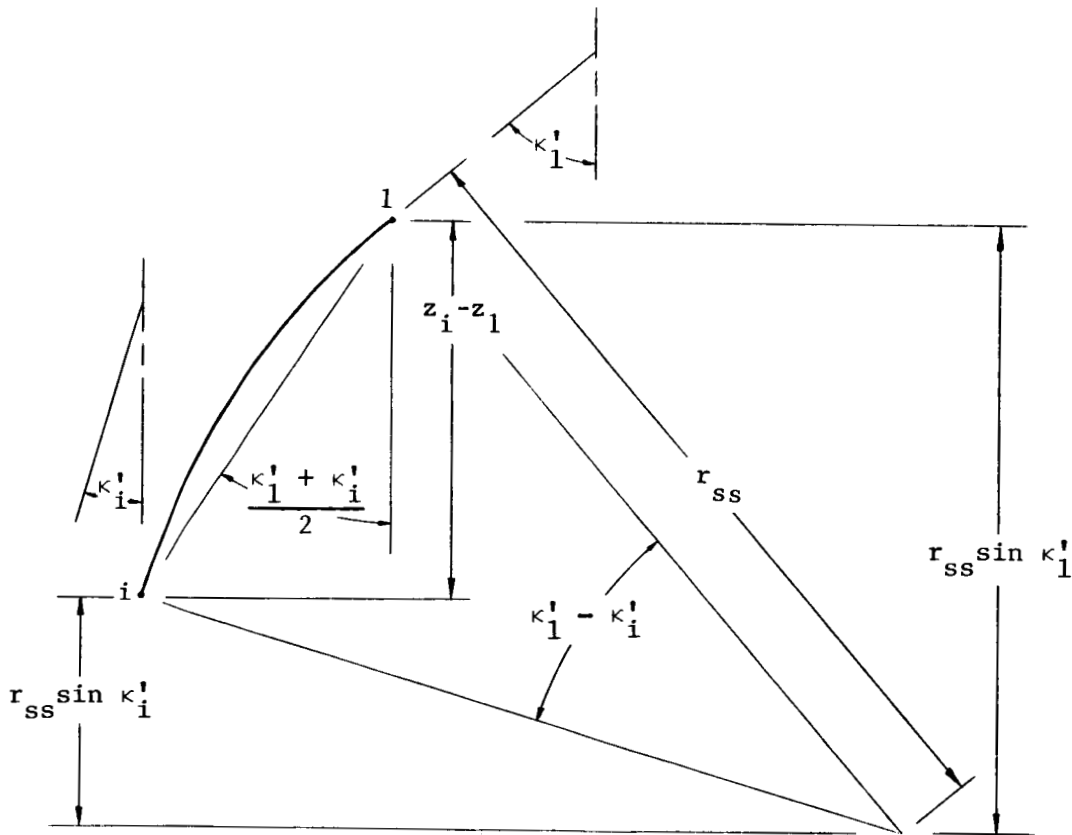
$$\gamma^\circ = \arctan \frac{u_2}{z_2 - z_1} \quad (B24)$$

where the numerator and denominator are the summations of the projections of the supersonic and subsonic chords in the circumferential and axial directions:

$$u_2 = c_{ss} \sin \left(\kappa'_1 - \frac{\phi_{ss}}{2} \right) + c_{sb} \sin \left(\kappa'_1 - \phi_{ss} - \frac{\phi_{sb}}{2} \right), \quad (B25)$$

and
$$z_2 - z_1 = c_{ss} \cos \left(\kappa'_1 - \frac{\phi_{ss}}{2} \right) + c_{sb} \cos \left(\kappa'_1 - \phi_{ss} - \frac{\phi_{sb}}{2} \right). \quad (B26)$$

The direction of the camberline at a preselected axial location on the supersonic arc, point i, is determined using the method outlined in sketch 4.



sketch 4

Summation of the indicated lengths in the axial direction yeilds:

$$r_{ss} \sin \kappa'_i + (z_i - z_1) = r_{ss} \sin \kappa'_1 \quad , \quad (B27)$$

or rearranging:

$$\kappa'_i = \arcsin \left(\sin \kappa'_1 - \frac{z_i - z_1}{r_{ss}} \right) . \quad (B27a)$$

The circumferential displacement from the leading edge may be determined in a similar manner:

$$u_i = r_{ss} (\cos \kappa'_i - \cos \kappa'_1) \quad . \quad (B28)$$

To avoid numerical difficulty equation (B22) is substituted into equation (B27a) yielding the following preferred form:

$$\kappa'_i = \arcsin \left[\sin \kappa'_1 - \frac{2}{c_{ss}} \sin \frac{\phi_{ss}}{2} (z_i - z_1) \right] , \quad (B27b)$$

and an alternate form is introduced for equation (B28):

$$u_i = (z_i - z_1) \tan \frac{\kappa'_i + \kappa'_1}{2} \quad . \quad (B28a)$$

On the subsonic arc the following equations apply:

$$\kappa'_i = \arcsin \left[\sin (\kappa'_1 - \phi_{ss}) - \frac{(z_i - z_1) - c_{ss} \cos \left(\kappa'_1 - \frac{\phi_{ss}}{2} \right)}{r_{sb}} \right] , \quad (B29)$$

$$\text{and} \quad u_i = c_{ss} \sin \left(\kappa'_1 - \frac{\phi_{ss}}{2} \right) + r_{sb} \left[\cos \kappa'_1 - \cos (\kappa'_1 - \phi_{ss}) \right] \quad . \quad (B30)$$

Again alternate equations are introduced to avoid numerical difficulty:

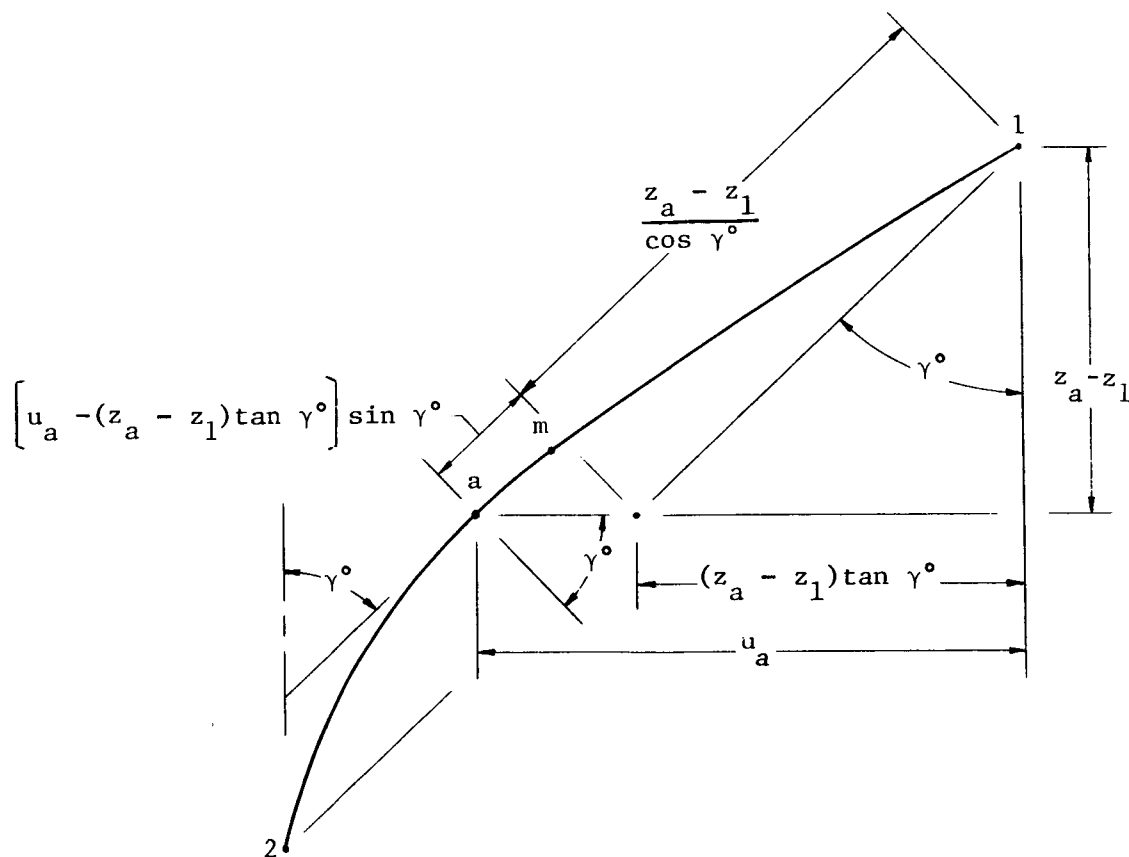
$$\kappa'_i = \arcsin \left\{ \sin (\kappa'_1 - \phi_{ss}) - \frac{2}{c_{sb}} \sin \frac{\phi_{sb}}{2} \left[(z_i - z_1) - c_{ss} \cos \left(\kappa'_1 - \frac{\phi_{ss}}{2} \right) \right] \right\} \quad (B29a)$$

and

$$u_i = c_{ss} \sin \left(\kappa'_1 - \frac{\phi_{ss}}{2} \right) + \left[(z_i - z_1) - c_{ss} \cos \left(\kappa'_1 - \frac{\phi_{ss}}{2} \right) \right] \tan \frac{\kappa'_i + \kappa'_1 - \phi_{ss}}{2} . \quad (B30a)$$

$$z_a - z_1 = c_{ss} \cos \left(\kappa_1' - \frac{\phi_{ss}}{2} \right) - r_{sb} \left[\sin \gamma^\circ - \sin (\kappa_1' - \phi_{ss}) \right] , \quad (B31)$$

$$u_a = c_{ss} \sin \left(\kappa_1' - \frac{\phi_{ss}}{2} \right) + r_{sb} \left[\cos \gamma^\circ - \cos (\kappa_1' - \phi_{ss}) \right]. \quad (B32)$$



sketch 5

Sketch 5 shows the case where the maximum camberline rise occurs toward the trailing edge with respect to the point, m, where the arcs join, or

$$\gamma^\circ < (\kappa_1' - \phi_{ss}) . \quad (B33)$$

For the case where the maximum camberline rise occurs towards the leading edge with respect to the point where the arcs join, or

$$\gamma^\circ > (\kappa_1' - \phi_{ss}) , \quad (B34)$$

the axial and circumferential displacements may be calculated using equations (B27) and (B28):

$$z_a - z_1 = -r_{ss}(\sin \gamma^\circ - \sin \kappa_1') , \quad (B35)$$

and

$$u_a = r_{ss}(\cos \gamma^\circ - \cos \kappa_1') . \quad (B36)$$

The displacement along the chord direction from the leading edge to the maximum camberline rise is obtained by addition of the two lengths indicated in sketch 5 and therefore

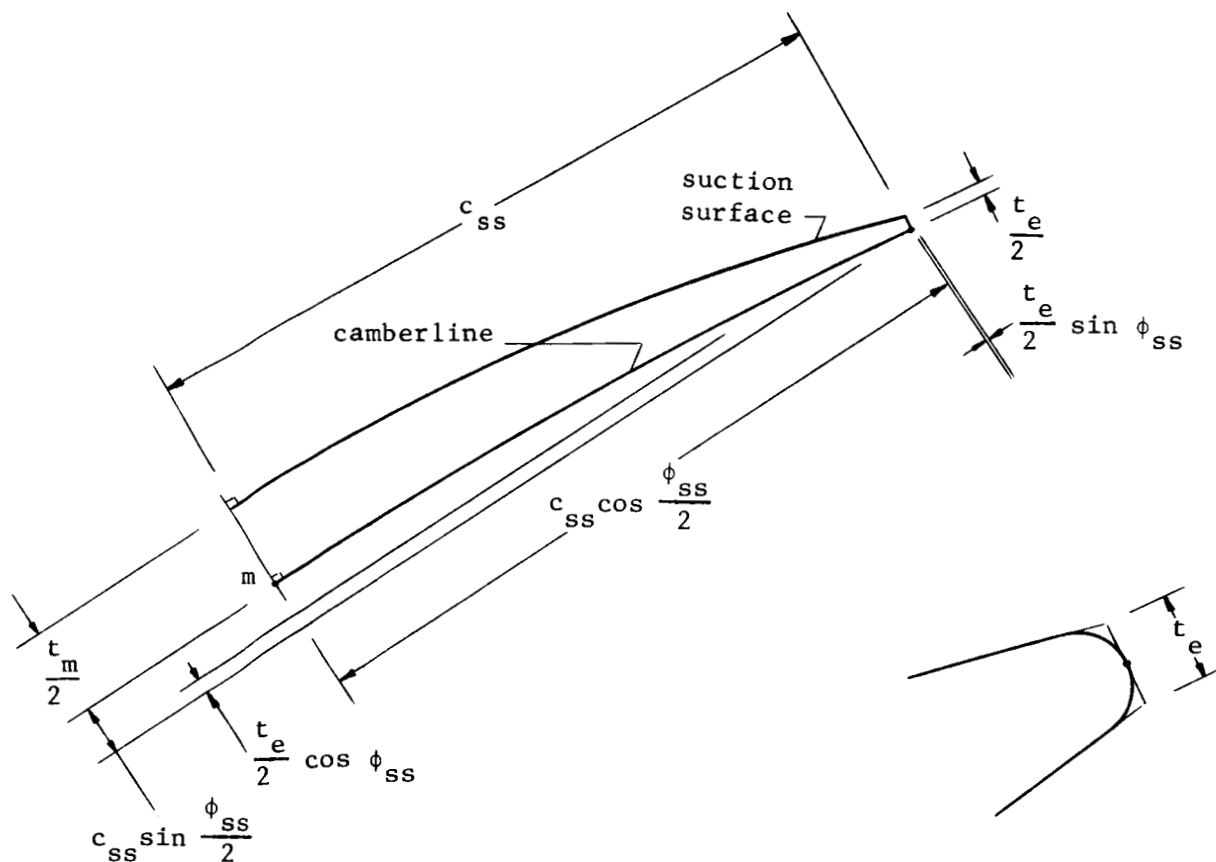
$$\frac{a}{c_t} = \frac{1}{c_t} \left\{ \frac{z_a - z_1}{\cos \gamma^\circ} + \left[u_a - (z_a - z_1) \tan \gamma^\circ \right] \sin \gamma^\circ \right\} . \quad (B37)$$

The difference in direction at the leading edge between the suction surface and the camberline is calculated following the method outlined in sketch 6. The edge thickness is considered to exist perpendicular to the camberline edge direction and at the edge; the suction and pressure surfaces are closed by a circular arc which passes through the camberline-edge point and is tangent to both surfaces. On the maximum thickness line the suction surface arc and the camberline arc have the same direction. The incidence angle required to set the suction surface at the leading edge parallel to the upstream flow direction is therefore just the difference in camber in the supersonic portion between the suction surface arc and the camberline arc:

$$i = \phi_{sss} - \phi_{ss} . \quad (B38)$$

Since

$$\tan \frac{\phi_{sss}}{2} = \frac{c_{ss} \sin \frac{\phi_{ss}}{2} + \frac{t_m}{2} - \frac{t_e}{2} \cos \phi_{ss}}{c_{ss} \cos \frac{\phi_{ss}}{2} + \frac{t_e}{2} \sin \phi_{ss}} , \quad (B39)$$



sketch 6

$$i = 2 \arctan \left(\frac{c_{ss} \sin \frac{\phi_{ss}}{2} + \frac{t_m}{2} - \frac{t_e}{2} \cos \phi_{ss}}{c_{ss} \cos \frac{\phi_{ss}}{2} + \frac{t_e}{2} \sin \phi_{ss}} \right) - \phi_{ss} \quad (B40)$$

Calculation of incidence angles for double-circular-arc blade elements cannot be performed using equation (B40), because, unlike the multiple-circular-arc case, the positions on the camberline of the rear terminus of the supersonic arc and the maximum thickness do not coincide. Suppose in sketch 6 that the point where the supersonic and subsonic arcs join were moved rearward (as is

the case in the tip region for Rotor 2D); the camber of the arc between the leading edge and the maximum thickness points can then be designated ϕ_m , and the chord of the arc, c_m , in both sketch 6 and equation (B40). By observing that for double-circular-arc elements the following relationships exist:

$$\phi_m = \frac{\phi_t}{2} \quad \text{and} \quad c_m = \frac{c_t}{2 \cos \frac{\phi_m}{2}}, \quad (\text{B41})$$

for the double-circular arc equation (B40) may be written

$$i = 2 \arctan \left(\frac{c_t \tan \frac{\phi_t}{4} + t_m - t_e \cos \frac{\phi_t}{2}}{c_t + t_e \sin \frac{\phi_t}{2}} \right) - \frac{\phi_t}{2}. \quad (\text{B42})$$

Special Airfoil Generator
(SAG)

With this program the description of the blade as a series of cascade projections for the several axisymmetric stream surfaces is converted to a description on cylindrical surfaces from which the blade can be manufactured. The blade is stacked and lean angles, λ , are calculated in the event additional axisymmetric flow field calculations are desired.

At each grid point (intersection of meridional streamline and axial station) cylindrical blade angles are calculated from

$$\kappa'_{\text{cyl}} = \arctan (\tan \kappa' - \tan \epsilon \tan \lambda) \quad , \quad (\text{B43})$$

and curve-fit radially so that values may be found on the desired cylindrical surfaces.

From knowledge of the axial locations of the blade edges, edge angles are calculated and an analytical description of the camberline angle versus z on the cylindrical surface is obtained. The effective-area coefficient due to the blade blockage and the edge thickness are curve-fit radially and values on the desired cylindrical surfaces are found. Coordinates for the camberline are obtained by integrating the camberline angle equation using additional axial locations for more complete description of the blade section. Surface coordinates are found by calculating the thickness distribution from

$$\frac{t}{c_t} = \frac{(1 - K_{\text{bkb}}) 2\pi r \cos \kappa'_{\text{cyl}}}{N_b c_t} \quad , \quad (\text{B44})$$

and applying it normal to the camberline.

After the centers-of-area of the sections are determined the sections are displaced axially and circumferentially to obtain the desired relationship of each section to a radial line. Lean angles are calculated at the desired axial planes by differentiation of the functional relationship between circumferential position and radius. The sign convention for lean angle, λ , is that which yields a positive angle when a point moving along the blade moves opposite to the direction of rotor rotation as it moves outward along the blade.

APPENDIX C

THROAT AREA PARAMETER

The knowledge of the details of the axisymmetric flow field inside a transonic rotor blade row allows an approximate calculation which measures the capability of any rotor blade element to pass the flow for which it was designed. The result of this calculation is named the Throat Area Parameter; it is defined as follows:

$$\frac{\left(\frac{A}{A^*}\right)_{thr}}{\left(\frac{A}{A^*}\right)_1} = \frac{A_1^*}{A_{thr}^*} \frac{K_{bkthr}}{h_1} \frac{h_{thr}}{L_1} \frac{L_{thr}}{L_1} \quad (C1)$$

The radial stream tube height, h , is obtained from overall CAFD calculations. The capture width, L_1 , is just the product, $s_1 \cos \beta'$. The throat width,

L_{thr} is the distance between the pressure and suction surfaces of a cascade in the cascade projection at the location where the area found by the product, $\frac{Lh}{A_{thr}^*}$, is minimum. An example of the construction used to provide information for Throat Area Parameter calculations appears in figure 23. Trial-and-error is required to arrive at the throat location. The pressure surface of the next blade in the counter-rotor-wise direction is constructed with the correct circumferential spacing and its shape is therefore not identical with that of the first blade.

The effective area coefficient, K_{bkthr} , is introduced as a modifier on the throat stream tube height to provide for inclusion of any influence on the throat area which is not otherwise introduced. In these designs the blockage of the part-span shroud was distributed equally over the annulus height and accordingly resulted in no additional contraction of the axisymmetric stream-tube. The two percent blockage (fig. 4) of the part span shroud was used in all calculations (figs. 7(a) and 7(b)) involving equation (C1).

The change in critical flow area between the leading edge and the throat results from the change in relative stagnation conditions as the streamline radius changes. The ratio of critical areas may be expressed as follows:

$$\frac{A_1^*}{A_{thr}^*} = \left(\frac{P'_{thr}}{P'_1} \right)_{id}^{\frac{\gamma+1}{2\gamma}} \quad (C2)$$

where the ideal relative stagnation-pressure ratio is given by a rearrangement of an equation found in reference 11,

$$\left(\frac{P'_{thr}}{P'_1} \right)_{id} = \left\{ 1 + \left(\frac{U_1}{V'_1} \right)^2 \left(\frac{\frac{\gamma-1}{2}}{1 + \frac{\gamma-1}{2} M_1'^2} \right) \left[\left(\frac{r_{thr}}{r_1} \right)^2 - 1 \right] \right\}^{\frac{\gamma}{\gamma-1}} \quad (C3)$$

The Throat Area Parameter is usually plotted against inlet relative Mach number as in figures 7(a) and 7(b). On these coordinates, curves of throat area required for one-dimensional isentropic flow and for flow with the loss in relative stagnation pressure associated with one normal shock at the inlet relative Mach number may be constructed. A Throat Area Parameter in excess of the one-normal-shock curve is preferred because the procedure for checking the throat area does not account for the following real flow effects which tend to require more throat area:

1. build-up of blade boundary layer,
2. build-up of annulus wall boundary layers from the leading edge to the blade throat,
3. shock losses in excess of those associated with one normal shock at the inlet relative Mach number, and
4. lack of uniform flow in the free stream at the blade throat.

REFERENCES

1. Lieblein, Seymour and Johnsen, Irving A.: Résumé of Transonic-Compressor Research at NACA Lewis Laboratory, Journal of Engineering for Power, Trans. ASME, Series A, Vol. 83, July 1961, Page 219.
2. Klapproth, John F., Jacklitch, John J., Jr., and Tysl, Edward R.: Design and Performance of a 1400-Foot-per-Second-Tip-Speed Supersonic Compressor Rotor, NACA RM E55A27, 1955.

3. Miller, Genevieve R., Lewis, George W., Jr., and Hartmann, Melvin J.: Shock Losses on Transonic Compressor Blade Rows, Journal of Engineering for Power, Trans. ASME, Series A, Vol. 83, July 1961, Page 235.
4. Robbins, William H., Jackson, Robert J., and Lieblein, Seymour: Blade-Element Flow in Annular Cascades, Aerodynamic Design of Axial-Flow Compressors, NASA SP-36, Chapt. VII, 1965, pp. 227-254.
5. Smith, Leroy H., Jr., and Yeh, Hsuan: Sweep and Dihedral Effects in Axial-Flow Turbomachinery, Journal of Basic Engineering, Trans. ASME, Series D, Vol. 85, 1963, pp. 401-416.
6. Carter, A.D.S.: The Low Speed Performance of Related Aerofoils in Cascade; National Gas Turbine Establishment, Report Number R55, September 1949, Aeronautical Research Council, C.P. No. 29, (12883).
7. Giffin, R.G., and Smith, L.H., Jr.: Experimental Evaluation of Outer Case Blowing or Bleeding of Single Stage Axial Flow Compressor, Part I - Design of Rotor and Bleeding and Blowing Configurations, NASA CR-54587, April 20, 1966.
8. Robbins, William H., and Glaser, Fredrick: Experimental Investigation of the Effect of Circumferential Inlet Flow Distortion on the Performance of a Five-Stage Axial-Flow Research Compressor with Transonic Rotors in all Stages, NACA RM E57J17, 1957.
9. Cornell, W.G.: ASME Paper No. 57-F-19, ASME Transactions, Vol. 80, #4, Page 791-799.
10. Smith, L.H., Jr.: The Radial Equilibrium Equation of Turbomachinery, Journal of Engineering for Power, Trans. ASME, Series A, Vol. 88, 1966, pp. 1-12.
11. Giamati, Charles C., Jr., and Finger, Harold B.: Design Velocity Distribution in Meridional Plane, Aerodynamic Design of Axial-Flow Compressors, NASA SP-36, Chapt. VIII, 1965, pp. 255-278.

Table 1. - Cascade Projection Data for Rotor 1B Blade Setting

ψ	$\frac{r_1}{r_t}$	β'_1	i	κ'_1	$\kappa'_{s1} - \kappa'_1$	$\frac{t_{e1}}{c_t}$
1.0	.9955	65.13	3.25	61.88	2.46	.0060
.9	.9586	63.74	3.68	60.06	2.91	.0063
.8	.9202	62.57	4.10	58.47	3.41	.0066
.7	.8807	61.48	4.54	56.94	4.03	.0069
.6	.8388	60.36	4.99	55.37	4.75	.0072
.5	.7947	59.29	5.48	53.81	5.47	.0076
.4	.7473	57.88	5.88	52.00	5.98	.0080
.3	.6963	56.50	6.02	50.48	6.51	.0084
.2	.6404	55.12	6.06	49.06	7.02	.0089
.1	.5768	53.74	6.22	47.52	7.54	.0094
0	.5000	52.39	7.08	45.31	8.02	.0100

ψ	$\frac{r_2}{r_t}$	β'_2	δ°	κ'_2	β'_{2e}	$\frac{t_{e2}}{c_t}$
1.0	.9804	58.63	3.70	54.93	56.77	.0058
.9	.9484	58.19	3.47	54.72	54.62	.0062
.8	.9135	57.08	3.55	53.53	52.36	.0065
.7	.8768	55.38	3.47	51.91	50.03	.0069
.6	.8385	53.10	3.41	49.69	47.29	.0072
.5	.7980	50.12	3.36	46.76	44.07	.0076
.4	.7547	46.21	3.95	42.26	39.96	.0080
.3	.7092	41.12	4.92	36.20	34.93	.0085
.2	.6607	34.57	6.22	28.35	28.32	.0090
.1	.6096	25.46	7.97	17.49	18.62	.0094
0	.5557	13.60	10.74	2.86	.37	.0100

ψ	$\frac{t_m}{c_t}$	γ°	$\frac{a}{c_t}$	σ	ϕ_t
1.0	.0350	60.77	.731	1.3062	6.95
.9	.0387	58.89	.696	1.3534	5.34
.8	.0425	57.07	.658	1.4075	4.94
.7	.0467	55.17	.616	1.4685	5.03
.6	.0509	52.94	.562	1.5387	5.68
.5	.0554	50.29	.500	1.6204	7.05
.4	.0604	47.13	.500	1.7183	9.74
.3	.0658	43.34	.500	1.8363	14.28
.2	.0714	38.71	.500	1.9836	20.71
.1	.0778	32.51	.500	2.1754	30.03
0	.0850	24.09	.500	2.4447	42.45

Table 2. - Cascade Projection Data for Rotor 2B Blade Setting.

ψ	$\frac{r_1}{r_t}$	β'_1	i	κ'_1	$\kappa'_{s1} - \kappa'_1$	$\frac{t_{e1}}{c_t}$
1.0	.9959	64.14	3.29	60.85	2.48	.0060
.9	.9597	62.60	3.68	58.92	2.95	.0062
.8	.9227	61.60	4.10	57.50	3.47	.0066
.7	.8840	60.60	4.52	56.08	4.06	.0069
.6	.8434	59.61	4.94	54.67	4.84	.0072
.5	.8005	58.55	5.35	53.20	5.45	.0076
.4	.7540	57.27	5.82	51.45	5.91	.0079
.3	.7046	56.20	6.10	50.10	6.36	.0083
.2	.6492	55.53	6.09	49.44	6.80	.0088
.1	.5850	56.18	5.90	50.28	7.23	.0093
0	.4995	61.18	5.70	55.48	7.56	.0100

ψ	$\frac{r_2}{r_t}$	β'_2	δ°	κ'_2	β'_{2e}	$\frac{t_{e2}}{c_t}$
1.0	.9800	54.58	5.70	48.88	52.91	.0060
.9	.9488	54.20	5.66	48.54	49.94	.0063
.8	.9160	52.77	5.38	47.39	47.54	.0066
.7	.8813	50.75	5.17	45.58	45.02	.0070
.6	.8456	47.97	5.22	42.75	41.83	.0074
.5	.8070	44.05	5.05	39.00	37.76	.0078
.4	.7675	39.12	5.73	33.39	32.78	.0082
.3	.7257	33.36	6.71	26.65	27.15	.0086
.2	.6824	26.32	8.21	18.11	19.68	.0091
.1	.6378	18.34	10.70	7.64	8.52	.0095
0	.5912	10.18	16.32	-6.64	-19.05	.0100

ψ	$\frac{t_m}{c_t}$	γ°	$\frac{a}{c_t}$	σ	ϕ_t
1.0	.0350	58.86	.726	1.3062	11.97
.9	.0387	56.41	.685	1.3523	10.38
.8	.0426	54.32	.642	1.4036	10.11
.7	.0466	52.00	.593	1.4620	10.50
.6	.0510	49.11	.533	1.5280	11.87
.5	.0556	46.10	.500	1.6055	14.20
.4	.0604	42.42	.500	1.6963	18.06
.3	.0655	38.37	.500	1.8044	23.45
.2	.0708	33.77	.500	1.9382	31.33
.1	.0770	28.96	.500	2.1106	42.64
0	.0850	24.42	.500	2.3663	62.12

Table 3. - Cascade Projection Data for Rotor 2E Blade Setting.

ψ	$\frac{r_1}{r_t}$	β'_1	i	κ'_1	$\kappa'_{s1} - \kappa'_1$	$\frac{t_{e1}}{c_t}$
1.0	.9963	64.67	3.29	61.38	2.49	.0060
.9	.9600	62.87	3.68	59.19	2.96	.0063
.8	.9229	61.79	4.10	57.69	3.48	.0066
.7	.8840	60.74	4.52	56.22	4.10	.0069
.6	.8433	59.66	4.94	54.72	4.84	.0072
.5	.8005	58.55	5.35	53.20	5.45	.0076
.4	.7540	57.27	5.82	51.45	5.91	.0079
.3	.7046	56.20	6.10	50.10	6.36	.0083
.2	.6492	55.53	6.09	49.44	6.80	.0088
.1	.5850	56.18	5.90	50.28	7.23	.0093
0	.4995	61.18	5.70	55.48	7.56	.0100

ψ	$\frac{r_2}{r_t}$	β'_2	δ°	κ'_2	β'_{2e}	$\frac{t_{e2}}{c_t}$
1.0	.9801	54.58	4.96	49.62	53.33	.0060
.9	.9489	54.41	4.79	49.62	50.47	.0063
.8	.9159	53.00	4.61	48.39	48.09	.0066
.7	.8815	50.84	4.69	46.15	45.17	.0070
.6	.8454	47.78	4.76	43.02	41.66	.0074
.5	.8070	44.05	5.05	39.00	37.76	.0078
.4	.7675	39.12	5.73	33.39	32.78	.0082
.3	.7257	33.36	6.71	26.65	27.15	.0086
.2	.6824	26.32	8.21	18.11	19.68	.0091
.1	.6378	18.34	10.70	7.64	8.52	.0095
0	.5912	10.18	16.82	-6.64	-19.05	.0100

ψ	$\frac{t_m}{c_t}$	γ°	$\frac{a}{c_t}$	σ	ϕ_t
1.0	.0350	57.40	.660	1.3058	11.76
.9	.0387	55.58	.621	1.3520	9.57
.8	.0426	53.85	.585	1.4036	9.30
.7	.0467	51.83	.562	1.4618	10.07
.6	.0510	49.30	.534	1.5283	11.70
.5	.0556	46.10	.500	1.6055	14.20
.4	.0604	42.42	.500	1.6963	18.06
.3	.0655	38.37	.500	1.8044	23.45
.2	.0708	33.77	.500	1.9382	31.33
.1	.0770	28.96	.500	2.1106	42.64
0	.0850	24.42	.500	2.3663	62.12

Table 4. - Cascade Projection Data for Rotor 2D Blade Setting.

ψ	$\frac{r_1}{r_t}$	β'_1	i	κ'_1	$\kappa'_{s1} - \kappa'_1$	$\frac{t_{e1}}{c_t}$
1.0	.9963	64.65	3.29	61.36	3.30	.0059
.9	.9600	62.76	3.68	59.08	3.71	.0062
.8	.9228	61.74	4.10	57.64	4.11	.0065
.7	.8841	60.66	4.52	56.14	4.50	.0069
.6	.8435	59.64	4.94	54.70	4.97	.0072
.5	.8005	58.55	5.35	53.20	5.45	.0076
.4	.7540	57.27	5.82	51.45	5.91	.0079
.3	.7046	56.20	6.10	50.10	6.36	.0083
.2	.6492	55.53	6.09	49.44	6.80	.0088
.1	.5850	56.18	5.90	50.28	7.23	.0093
0	.4995	61.18	5.70	55.48	7.56	.0100

ψ	$\frac{r_2}{r_t}$	β'_2	δ°	κ'_2	β'_{2e}	$\frac{t_{e2}}{c_t}$
1.0	.9794	54.52	3.48	51.04	53.41	.0060
.9	.9485	54.13	3.72	50.41	50.18	.0063
.8	.9157	52.77	3.92	48.85	47.77	.0066
.7	.8815	50.72	4.15	46.57	45.09	.0070
.6	.8454	47.78	4.57	43.21	41.71	.0074
.5	.8070	44.05	5.05	39.00	37.76	.0078
.4	.7675	39.12	5.73	33.39	32.78	.0082
.3	.7257	33.36	6.71	26.65	27.15	.0086
.2	.6824	26.32	8.21	18.11	19.68	.0091
.1	.6378	18.34	10.70	7.64	8.52	.0095
0	.5912	10.18	16.82	-6.64	-19.05	.0100

ψ	$\frac{t_m}{c_t}$	γ°	$\frac{a}{c_t}$	σ	ϕ_t
1.0	.0350	56.19	.500	1.3063	10.33
.9	.0387	54.74	.500	1.3523	8.67
.8	.0426	53.24	.500	1.4038	8.79
.7	.0466	51.35	.500	1.4618	9.57
.6	.0510	48.95	.500	1.5281	11.49
.5	.0556	46.10	.500	1.6055	14.20
.4	.0604	42.42	.500	1.6963	18.06
.3	.0655	38.37	.500	1.8044	23.45
.2	.0708	33.77	.500	1.9382	31.33
.1	.0770	28.96	.500	2.1106	42.64
0	.0850	24.42	.500	2.3663	62.12

Table 5. - Aeromechanical Data for Rotor Blading

	<u>Rotor 1B</u>	<u>Rotor 2B</u>
<u>Design speed stresses (psi)</u>		
Average root centrifugal stress	29,600	28,600
Total stress at root		
Convex side	59,500	27,000
Trailing edge	13,500	27,000
Total stress at shroud		
Convex side	16,900	15,500
Trailing edge	11,000	12,500
Maximum estimated stall vibratory stress at shroud (% endurance)		
Convex side	8,400 (22)	12,300 (31)
Trailing edge	7,600 (18)	5,300 (13)
<u>Blade natural frequencies at design speed (cps)</u>		
1st flexural	525	575
2nd flexural	1910	2150
1st torsional	1205	1340
<u>Tip untwist at design speed (deg)</u>	0.8	0.7
<u>Design speed reduced velocity</u>	1.33	1.19
<u>Material</u>	6Al-4V-Ti titanium alloy	

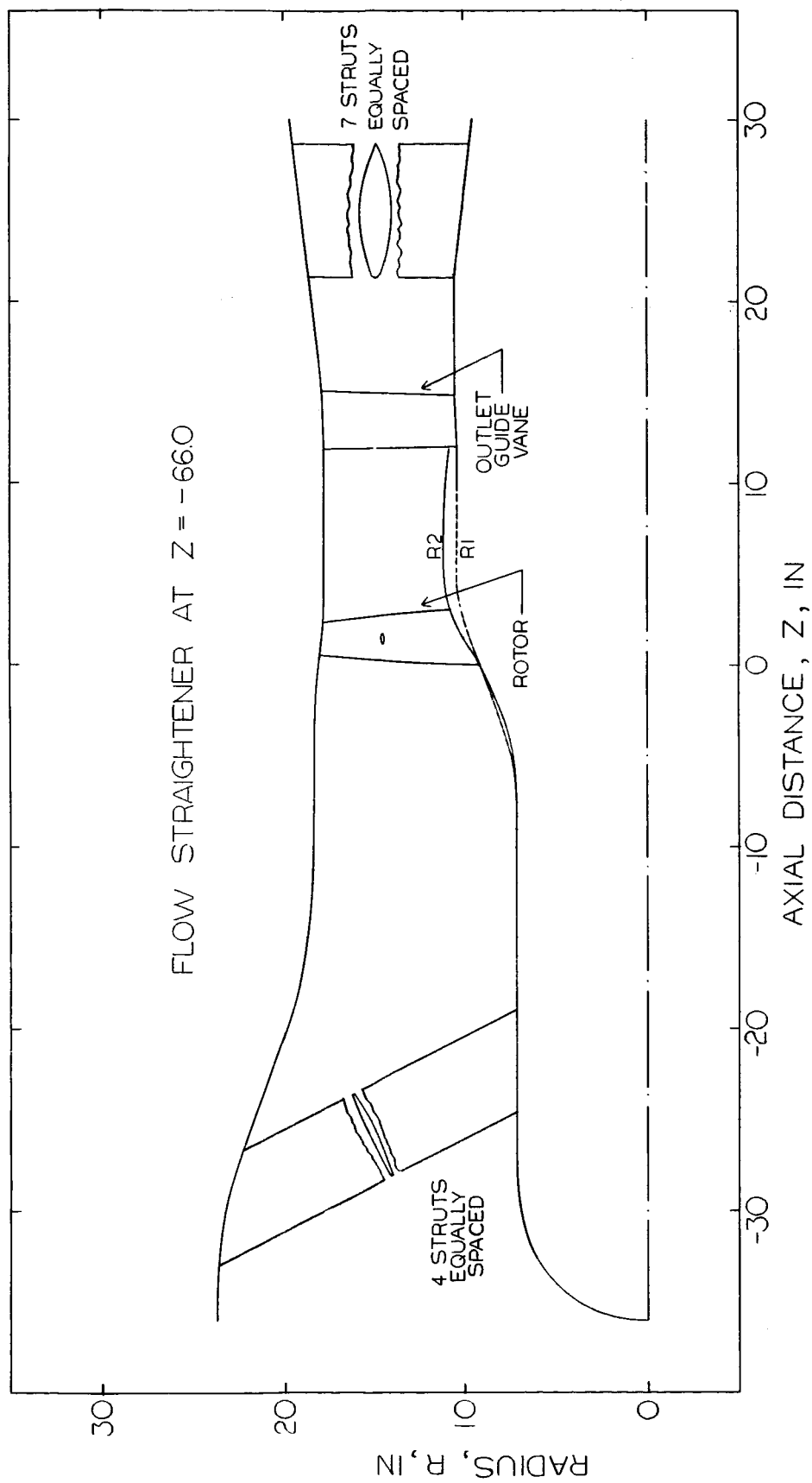


FIGURE 1. COMPRESSOR FLOWPATH

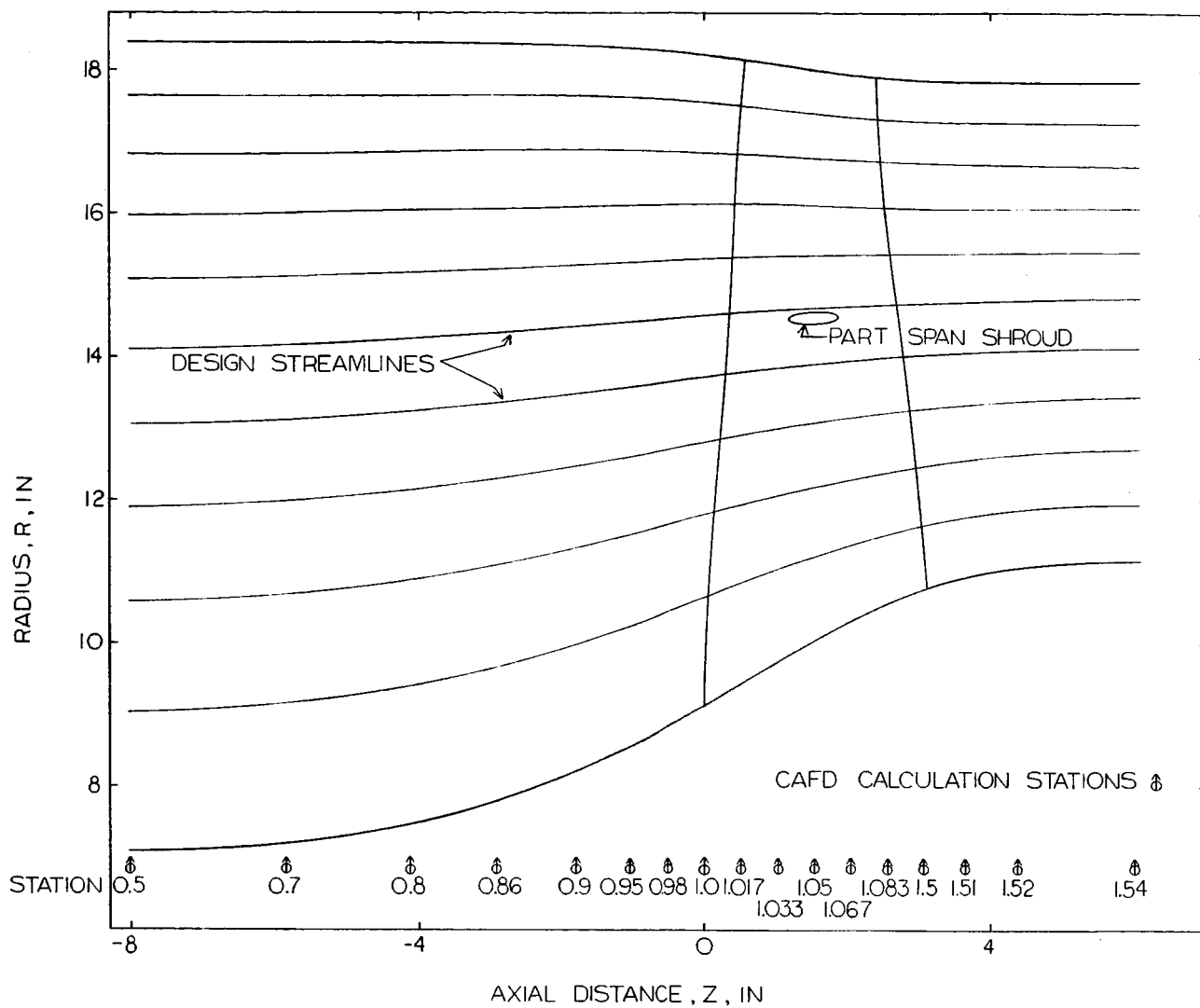


FIGURE 2. DESIGN FLOW FIELD FOR ROTORS 2

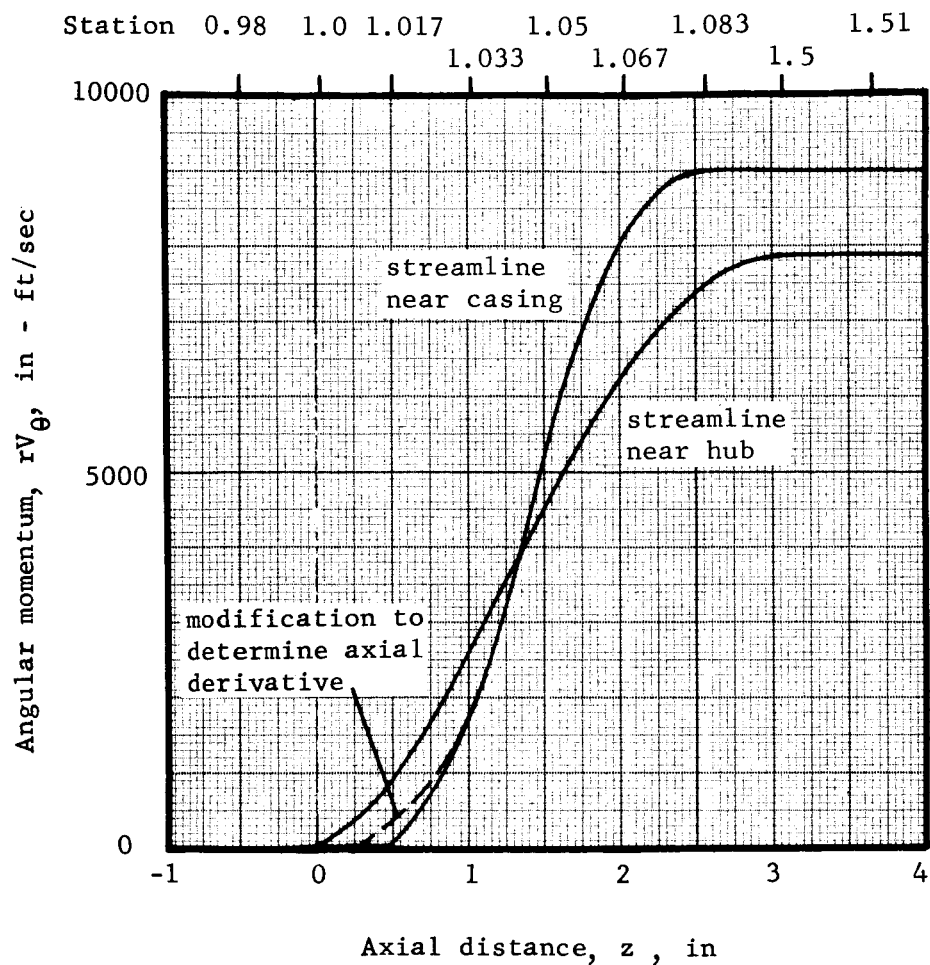


Figure 3. - Typical axial variation of angular momentum.

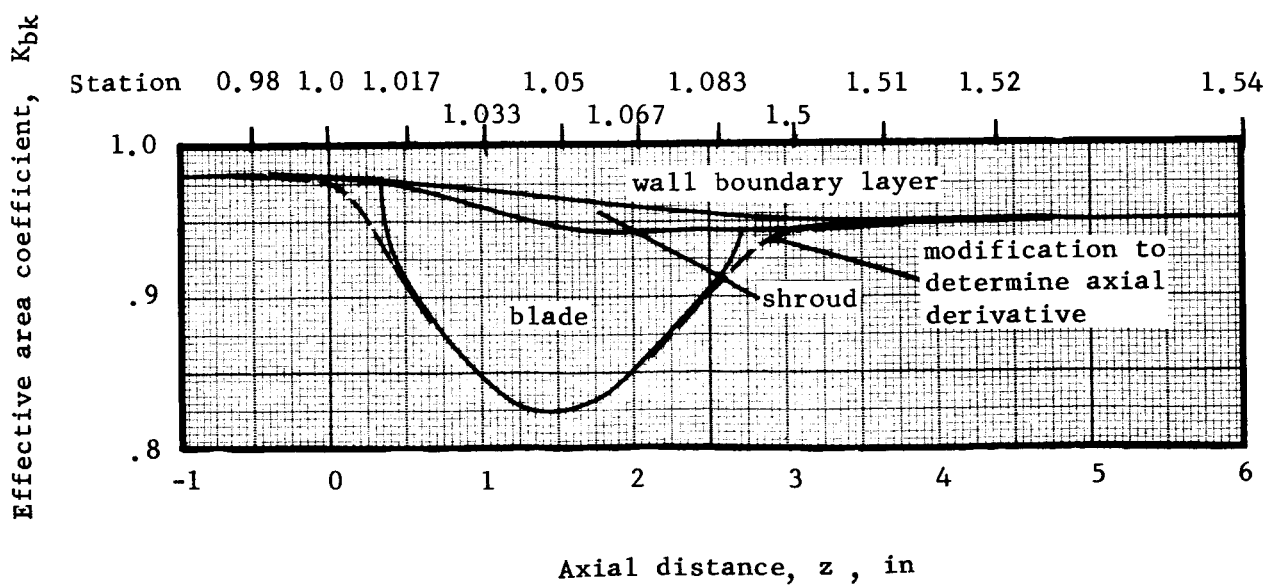


Figure 4. - Typical axial variation of effective area coefficient.

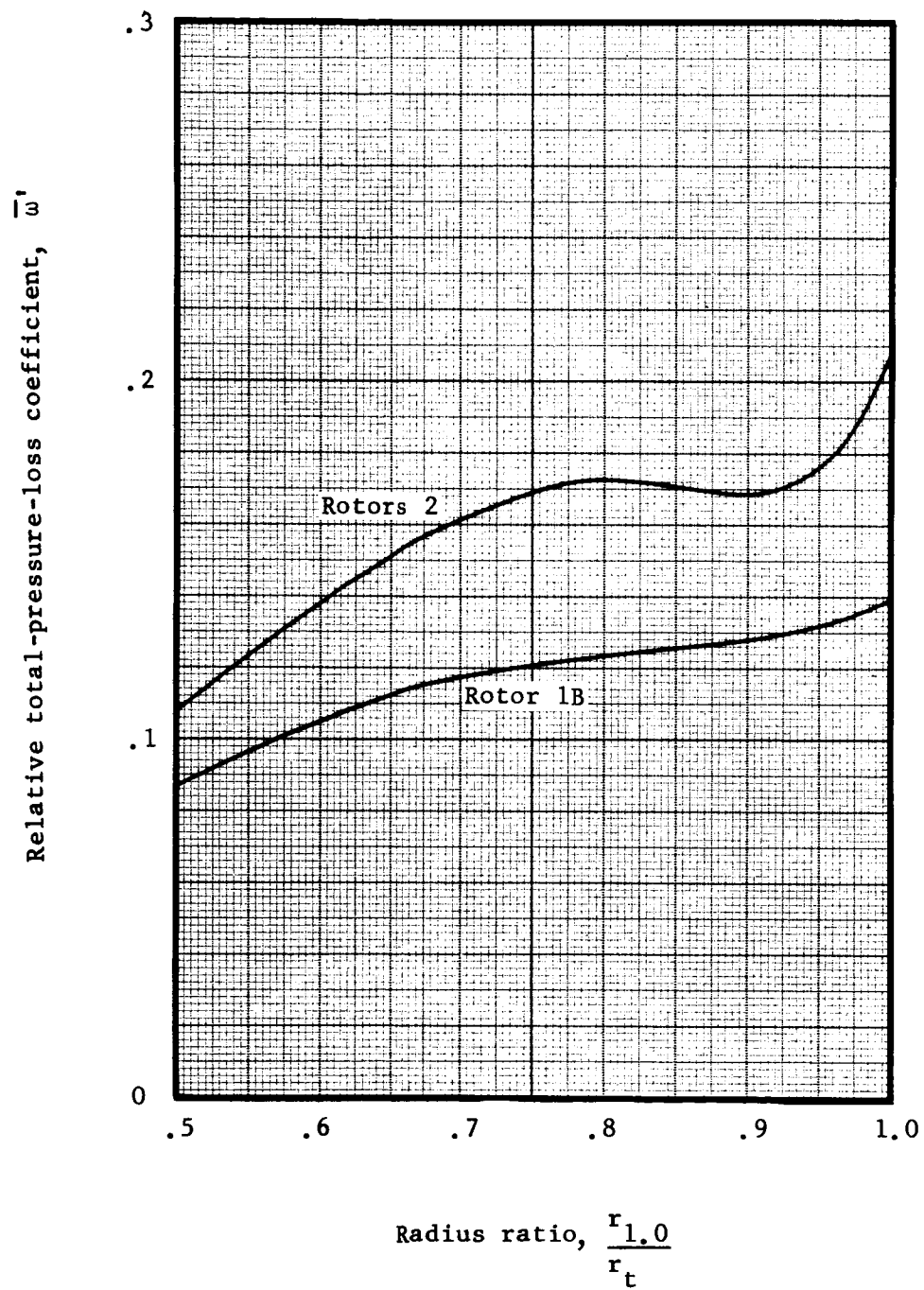


Figure 5. - Radial variation of design relative total-pressure-loss coefficients.

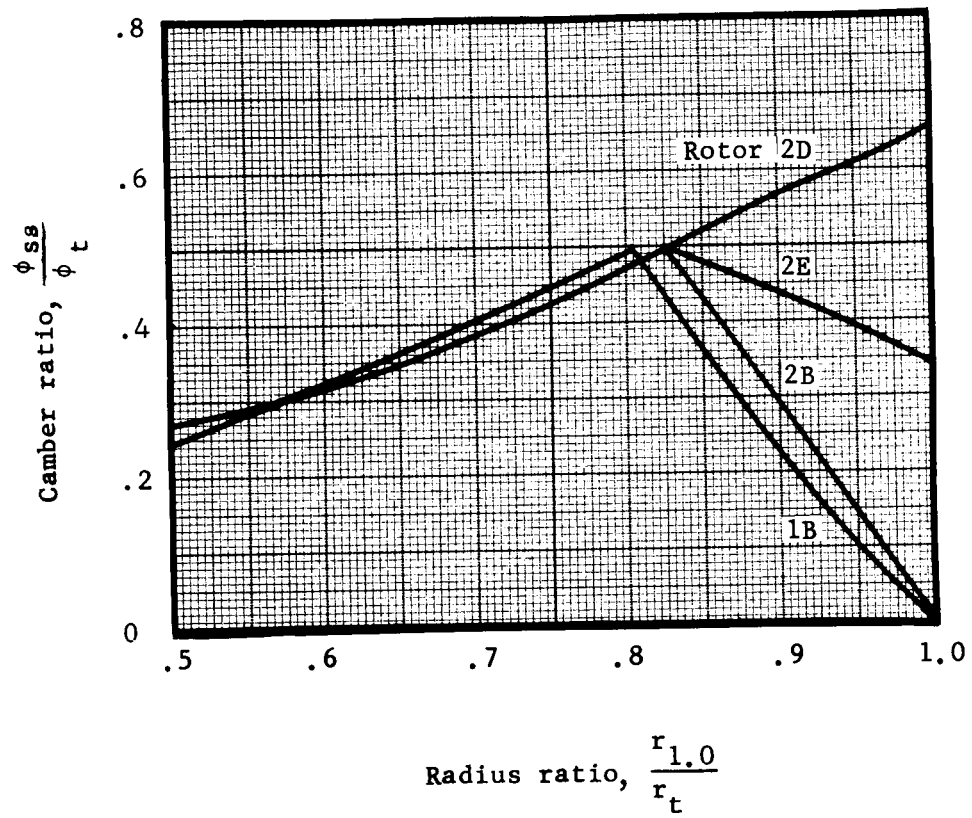


Figure 6. - Radial variation of design ratio of supersonic to total blade camber.

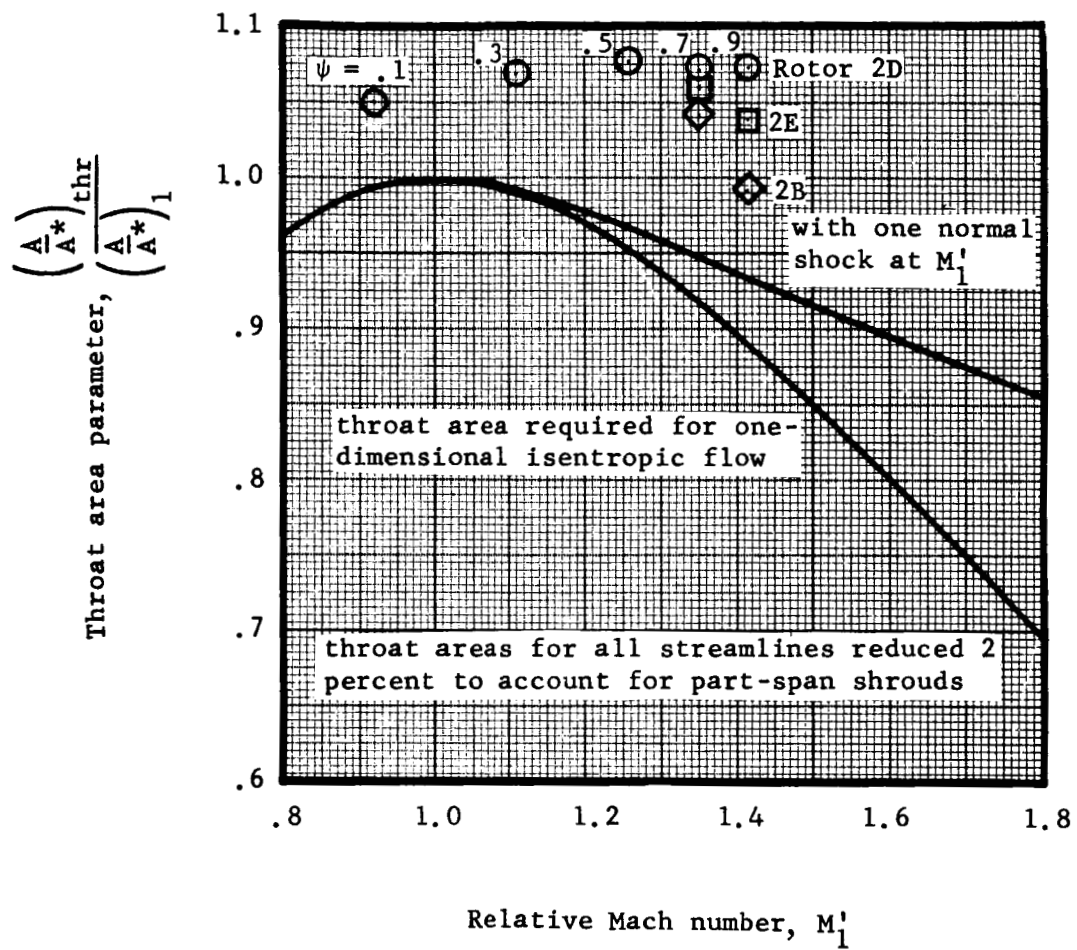


Figure 7(a). - Rotors 2 design choke check.

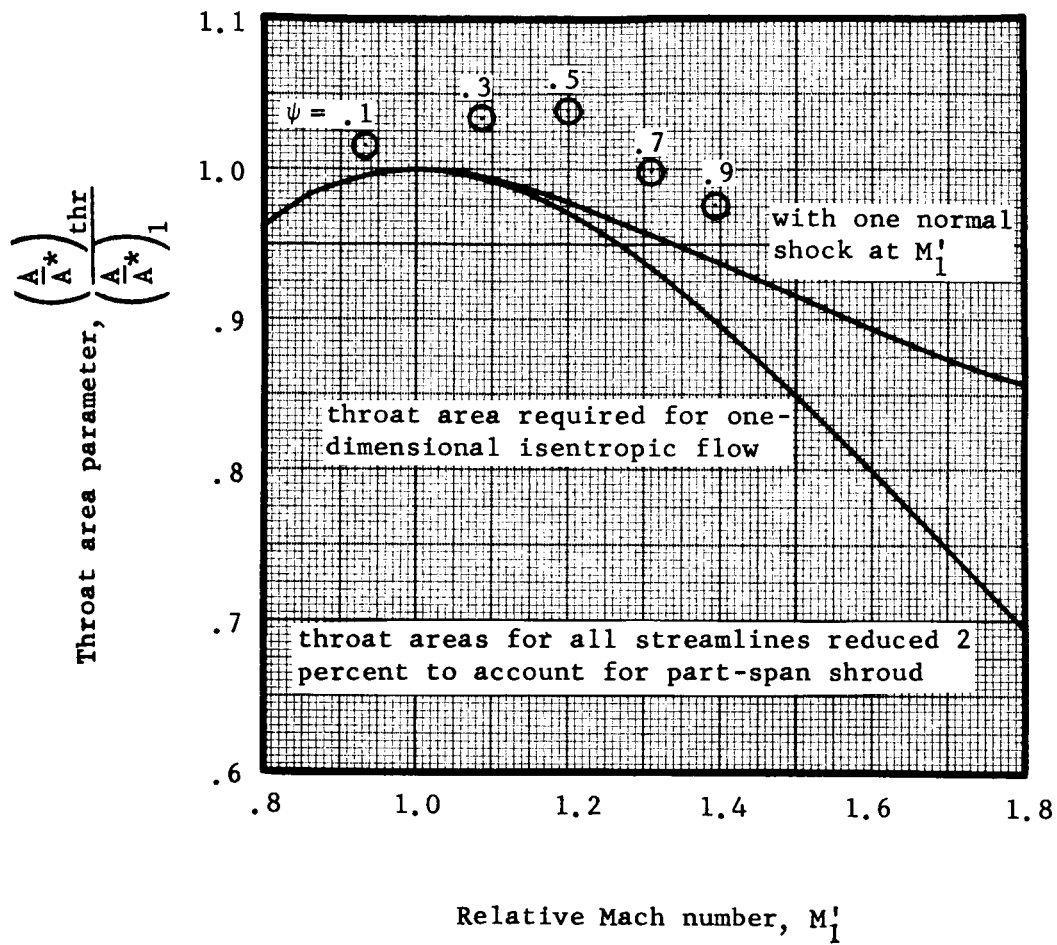


Figure 7(b). - Rotor 1B design choke check.

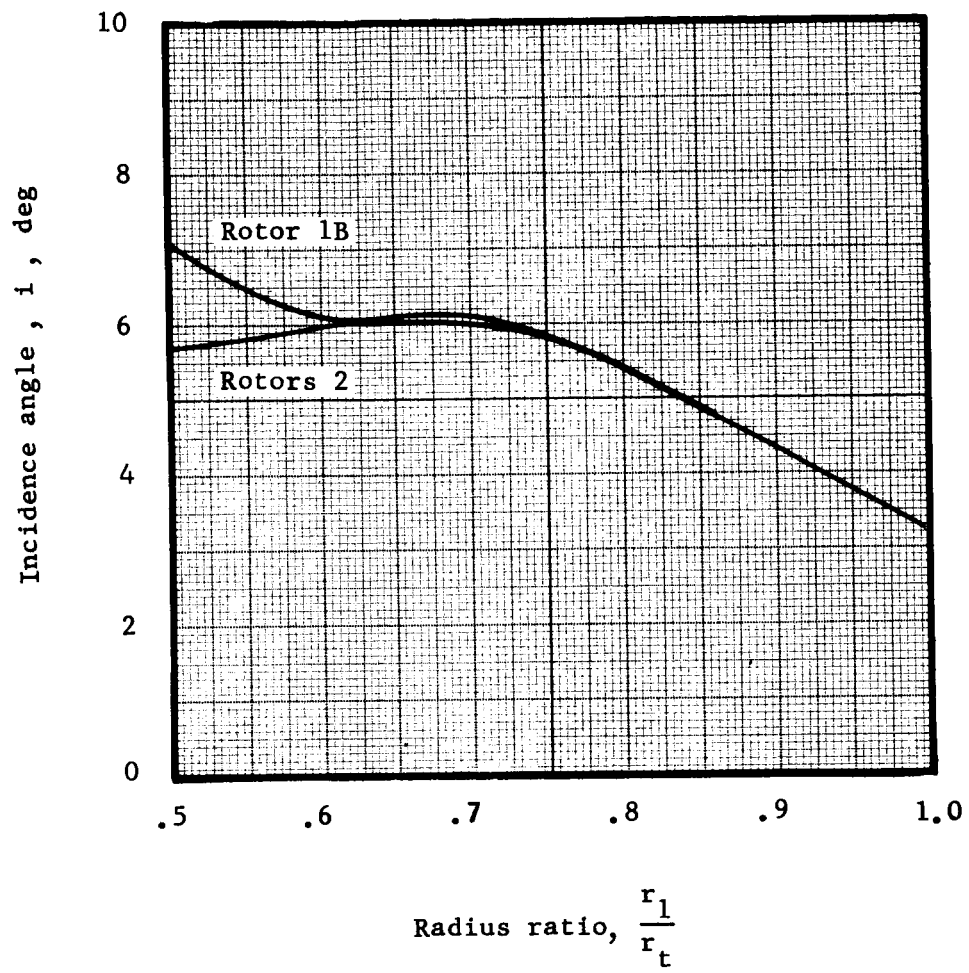


Figure 8. - Radial variation of design incidence angle.

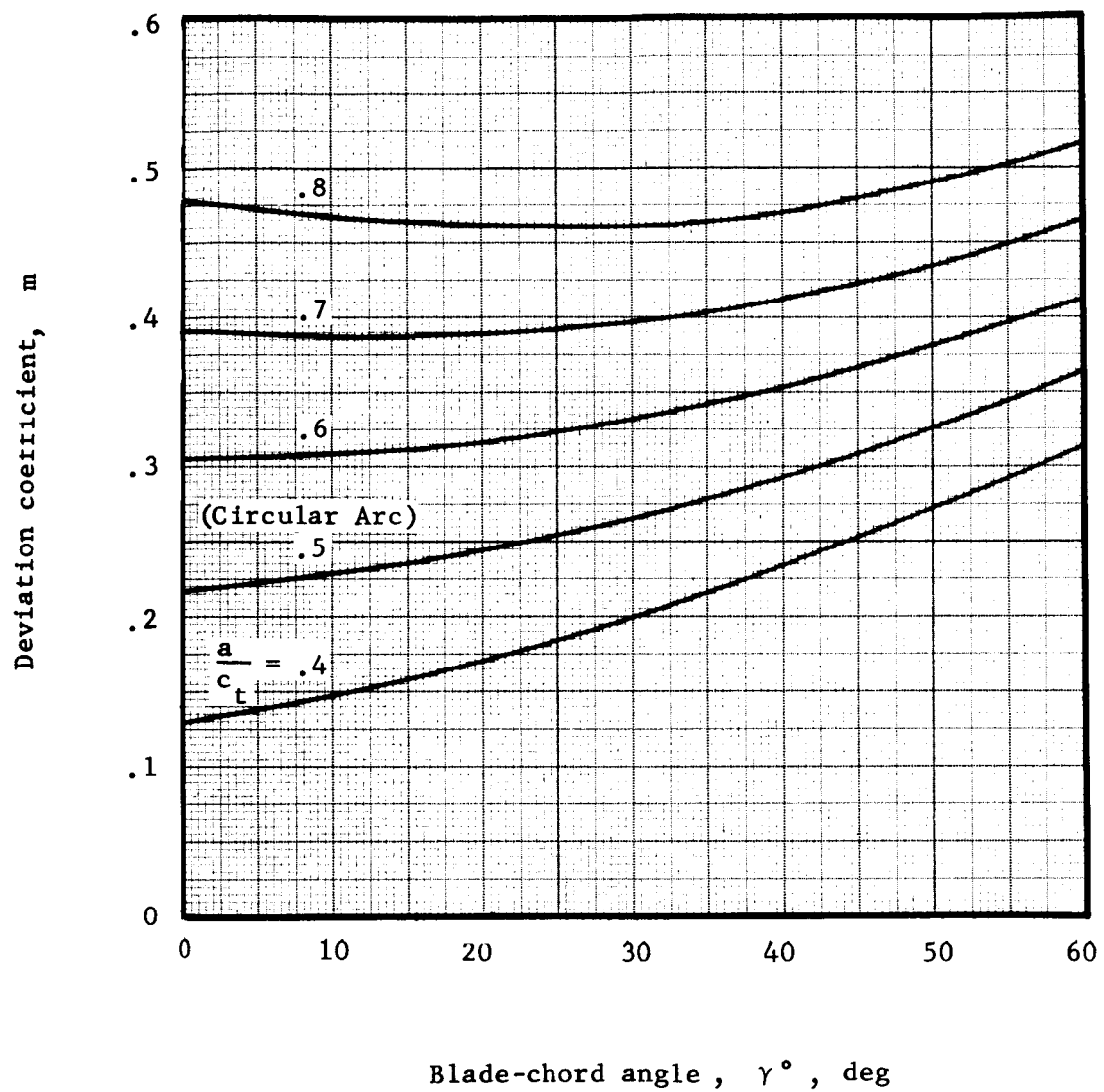


Figure 9. - Coefficients for design deviation angle rule.

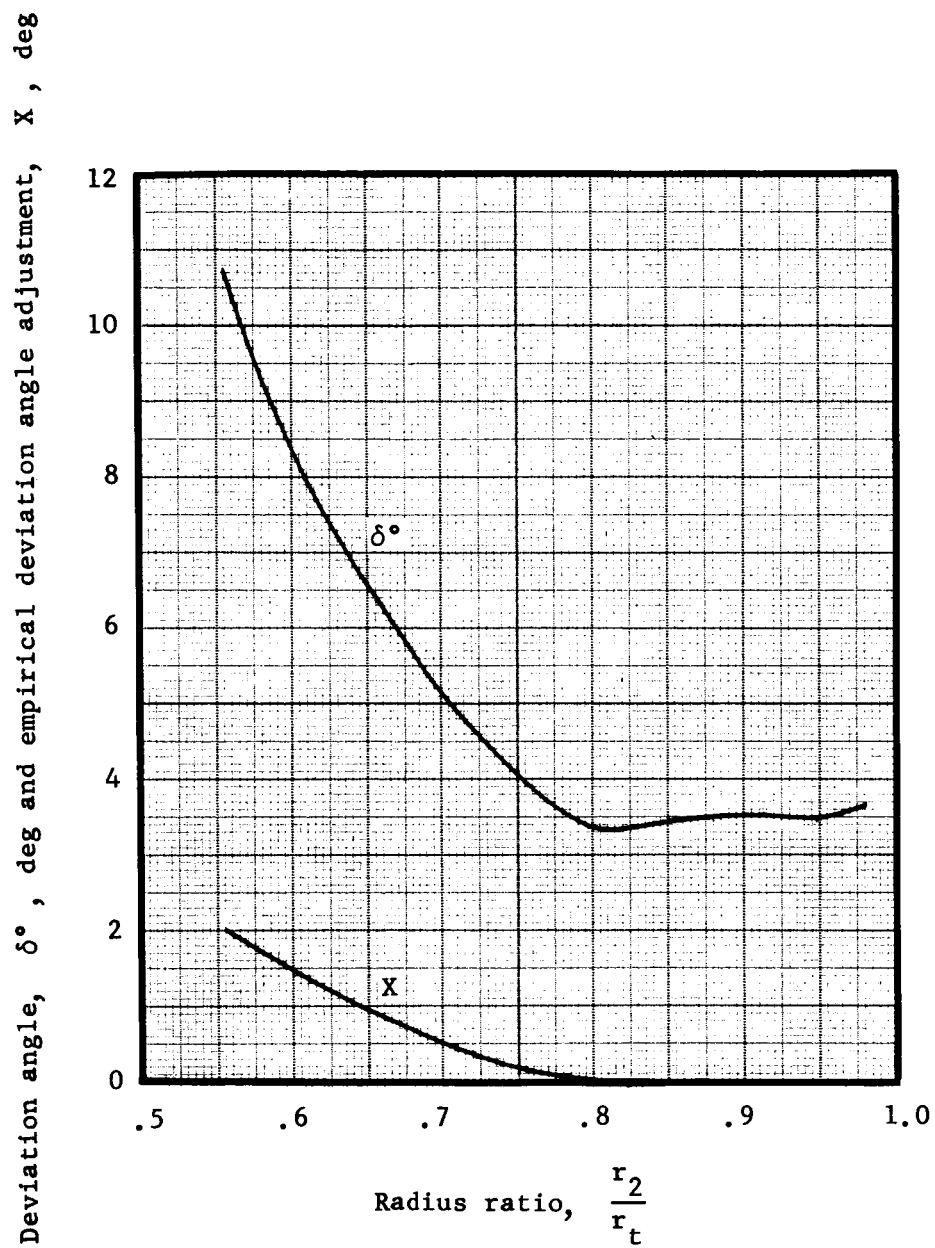


Figure 10(a). - Radial variation of Rotor 1B design deviation angle and empirical deviation angle adjustment.

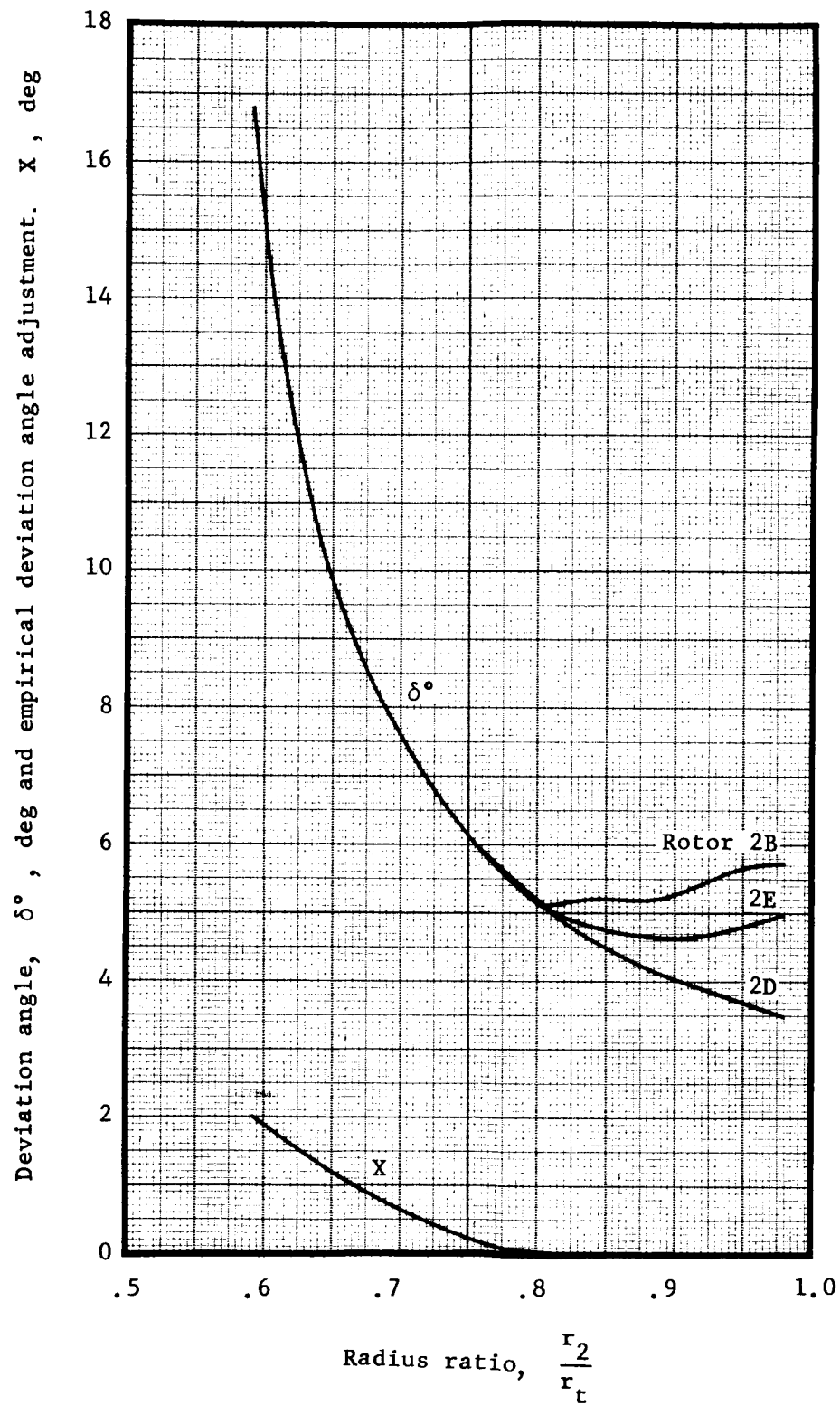


Figure 10(b). - Radial variation of Rotors 2 design deviation angle and empirical deviation angle adjustment.

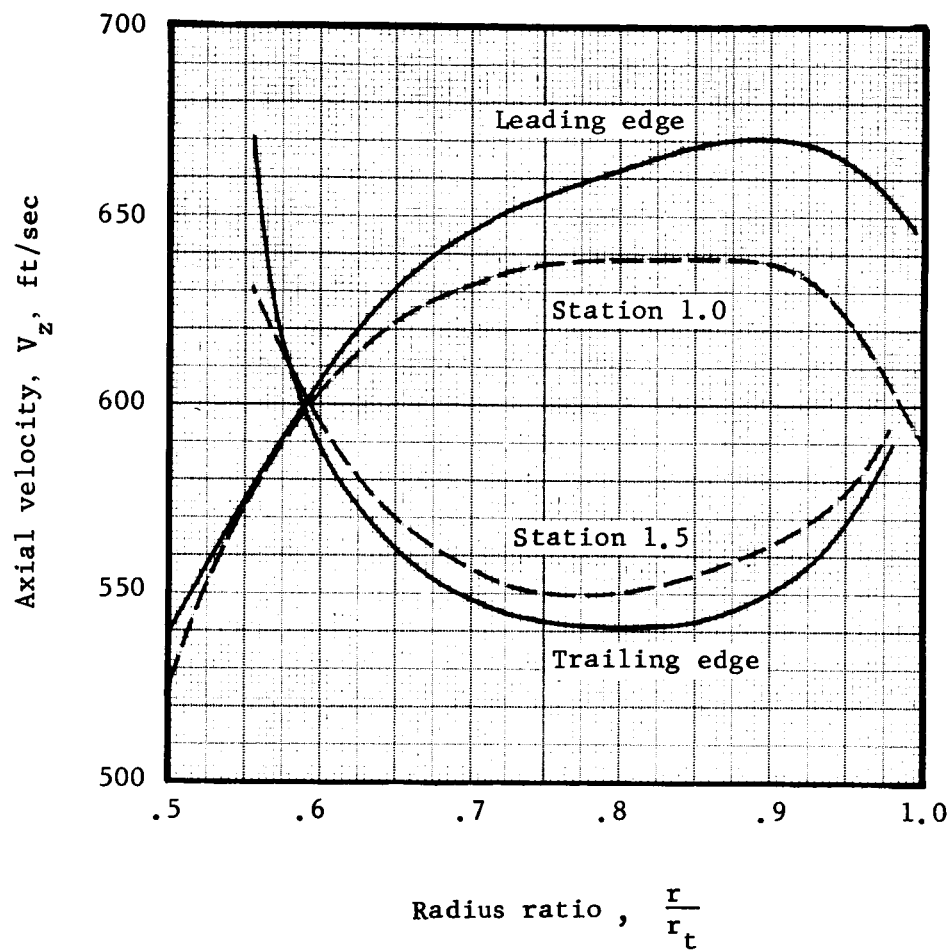


Figure 11. - Radial variation of Rotor 1B design axial velocity.

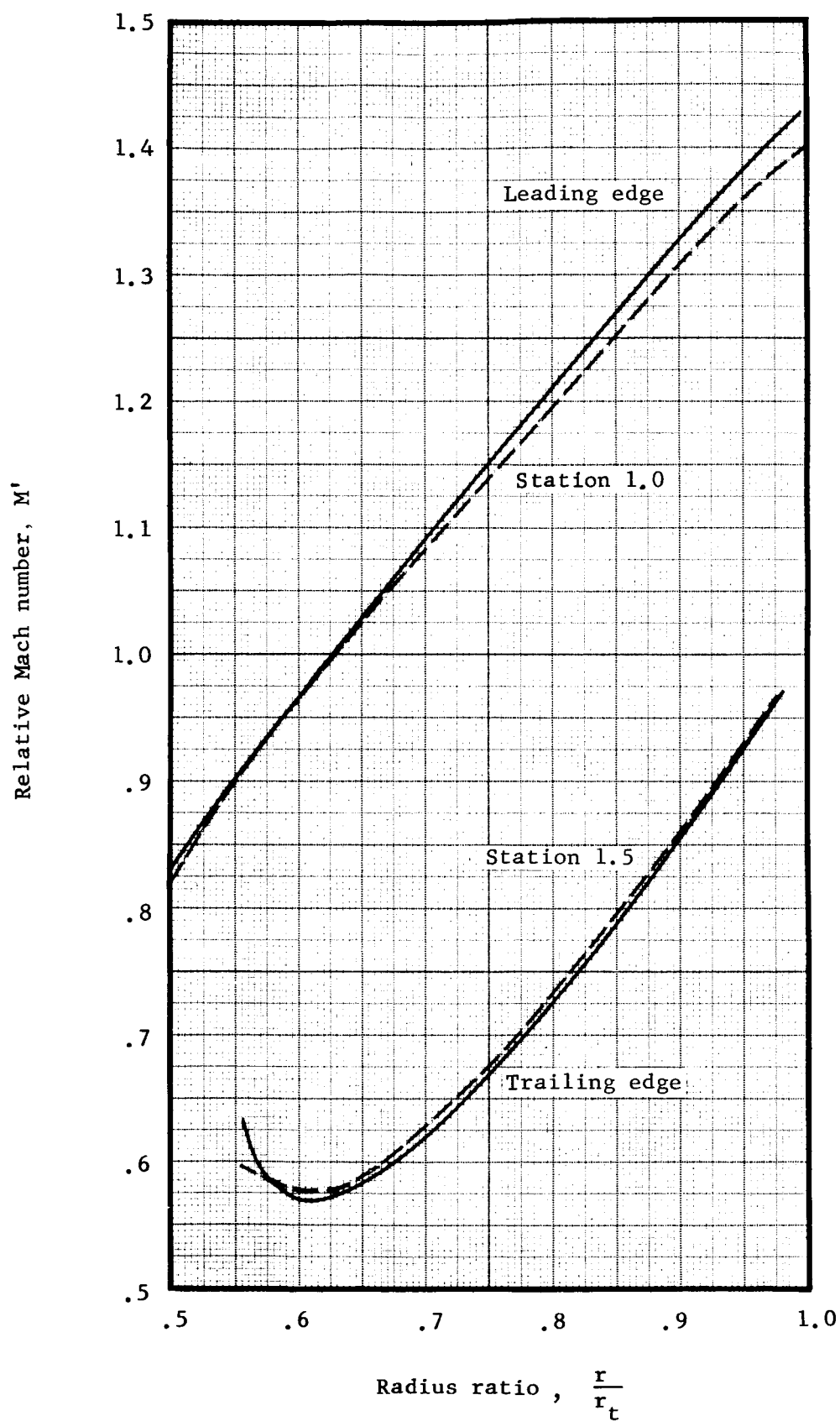


Figure 12. - Radial variation of Rotor 1B design relative Mach number.

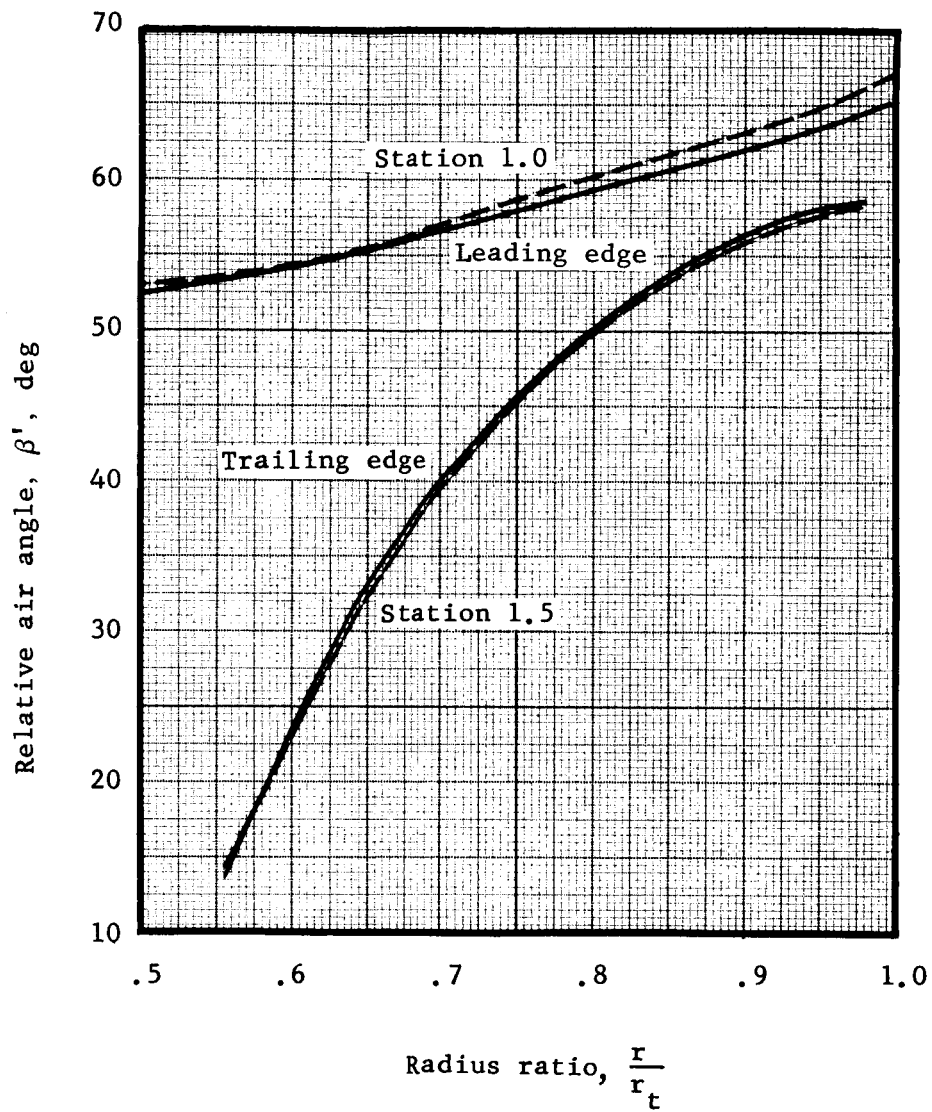


Figure 13. - Radial variation of Rotor 1B design relative air angle.

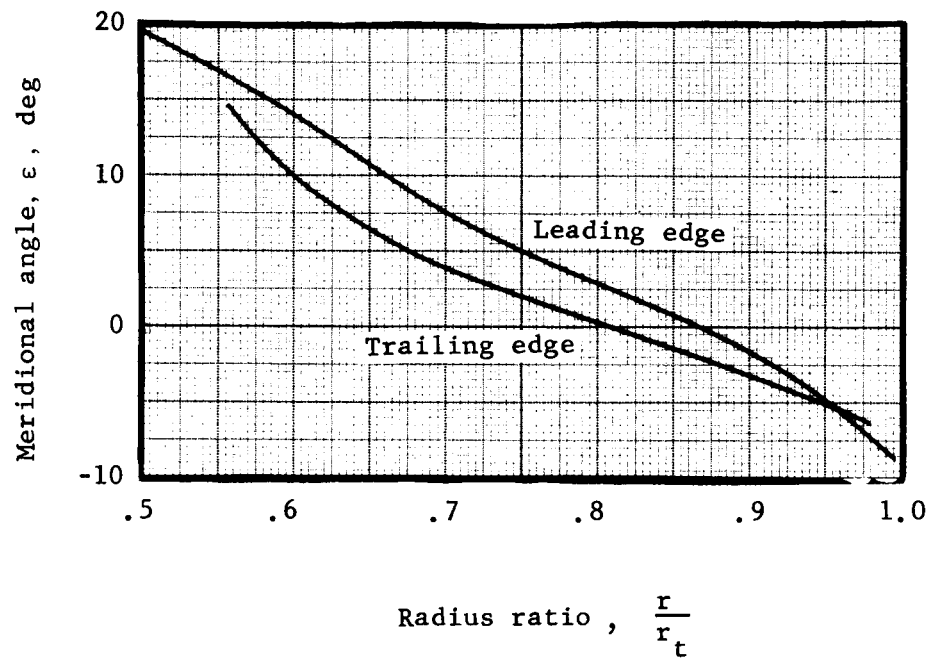


Figure 14. - Radial variation of Rotor 1B design streamline meridional angle.

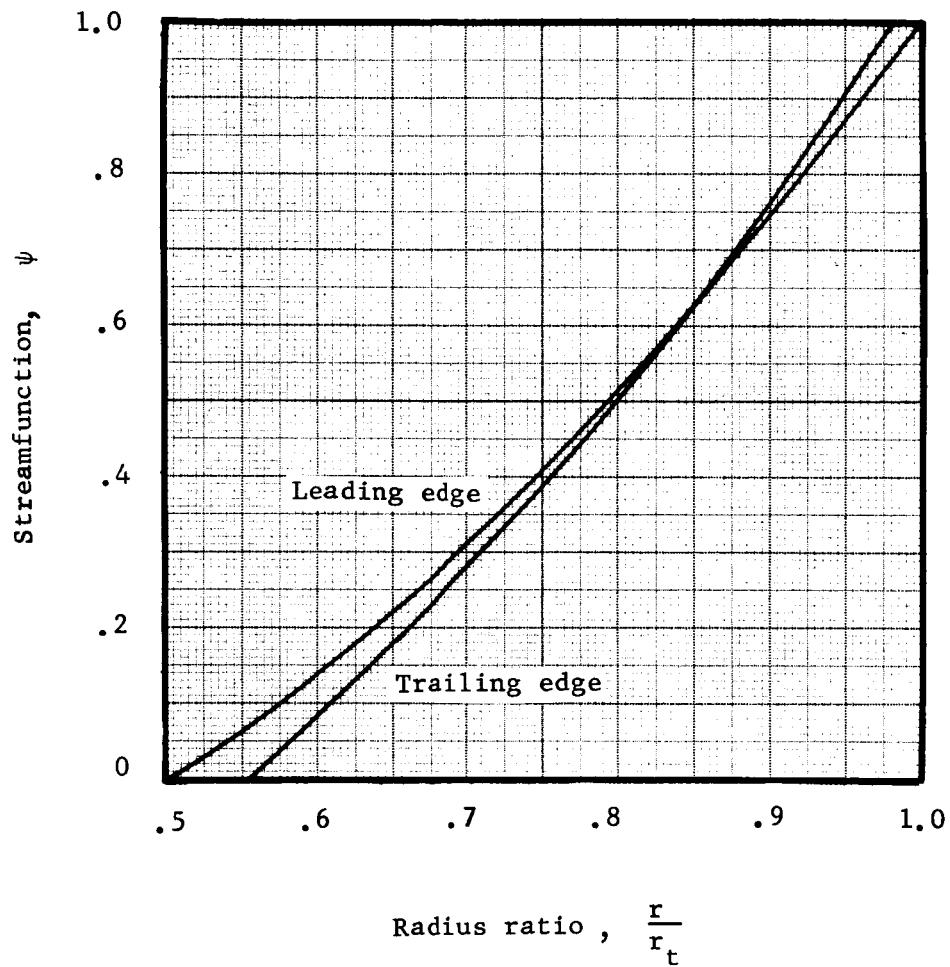


Figure 15. - Radial variation of Rotor 1B design streamfuction.

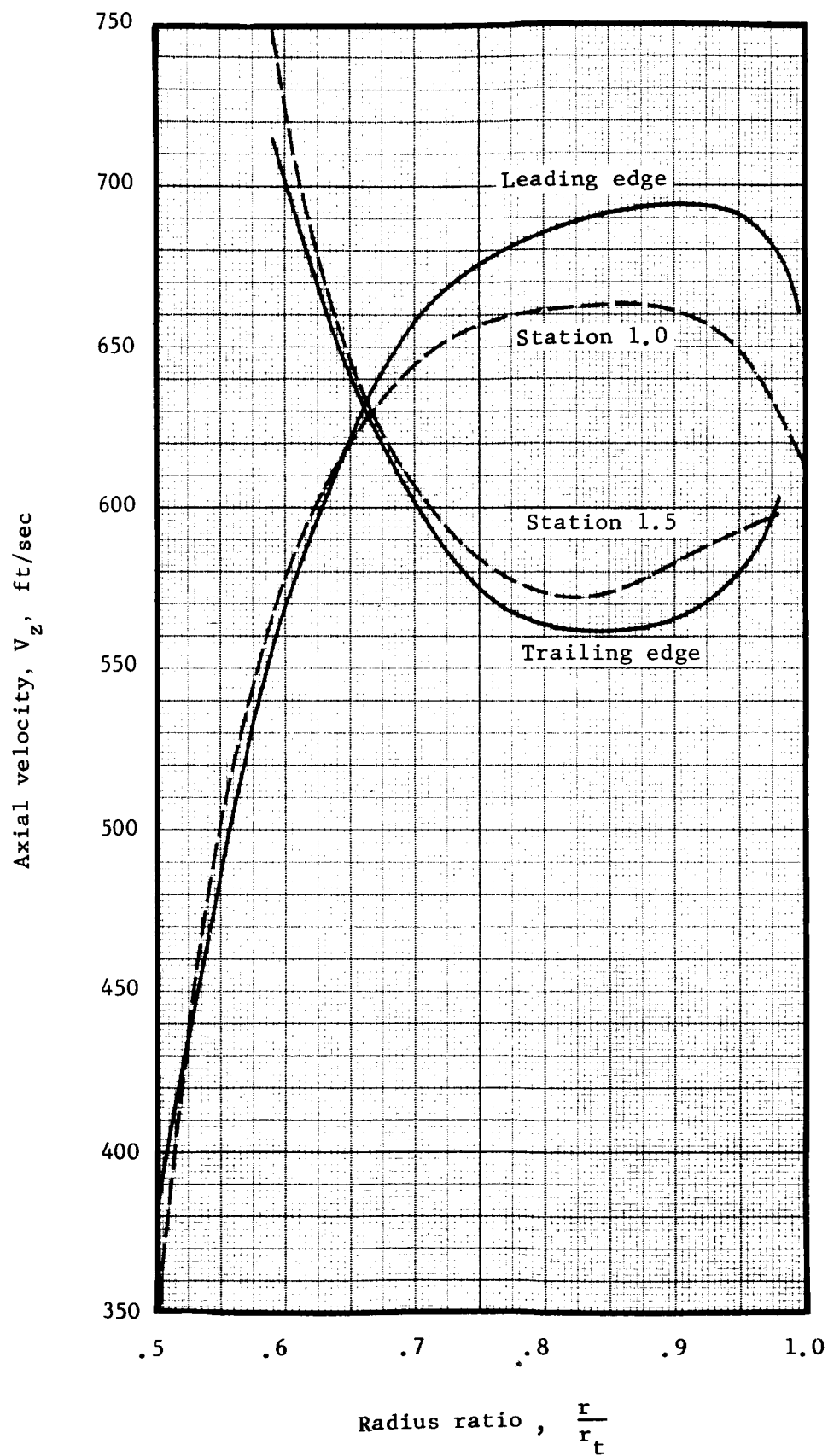


Figure 16. - Radial variation of Rotors 2 design axial velocity.

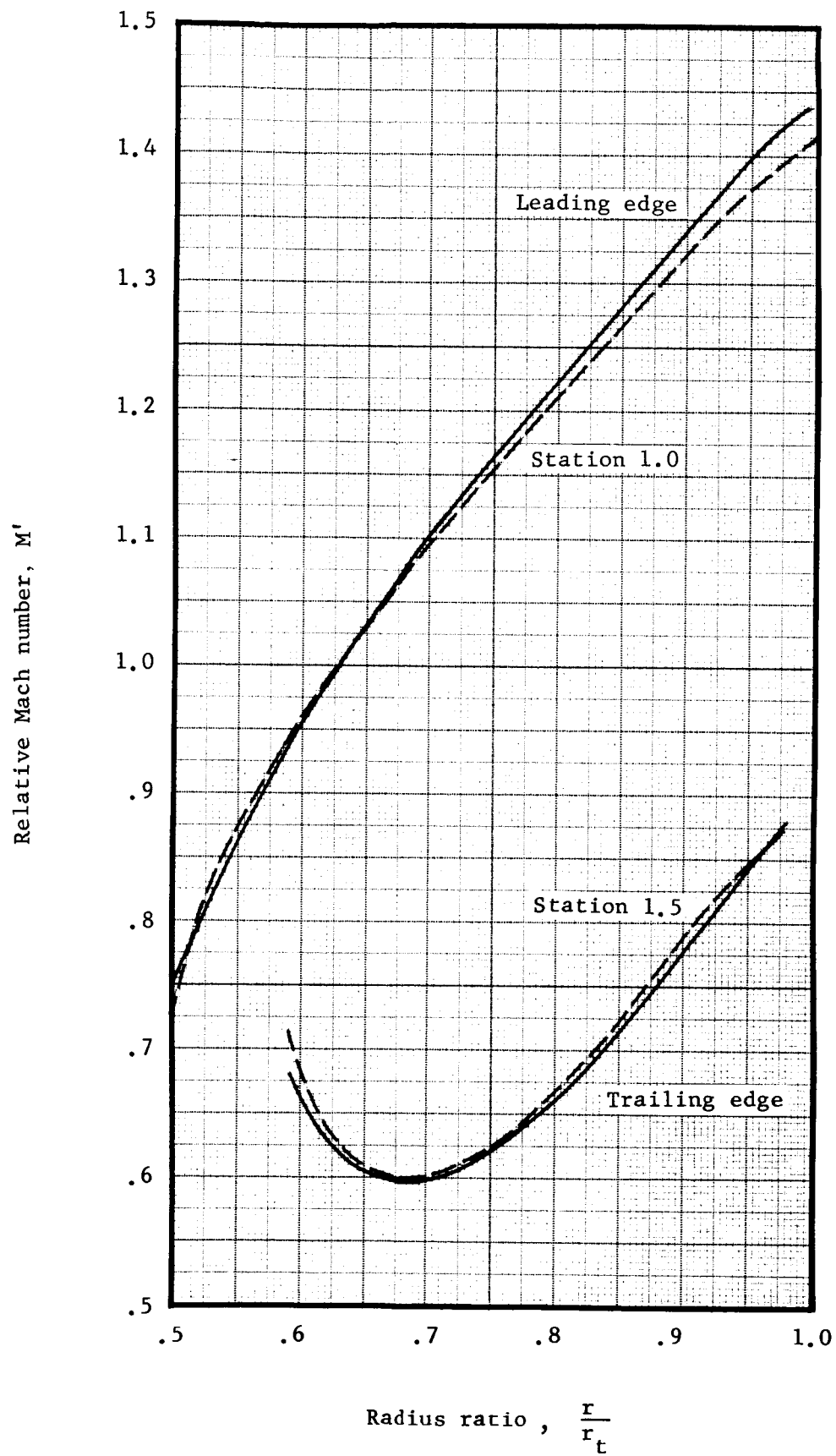


Figure 17. - Radial variation of Rotors 2 design relative Mach number.

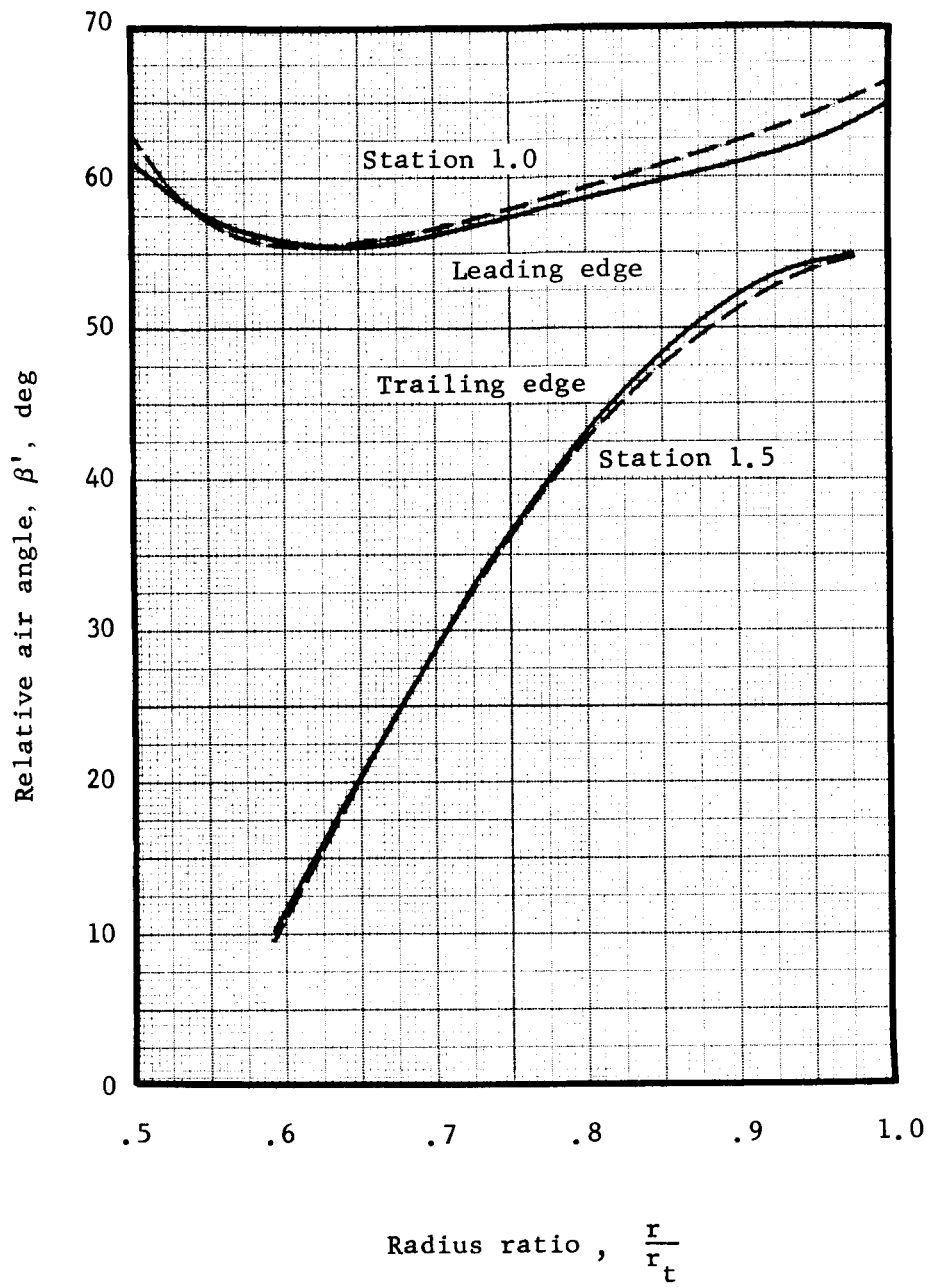


Figure 18. - Radial variation of Rotors 2 design relative air angle.

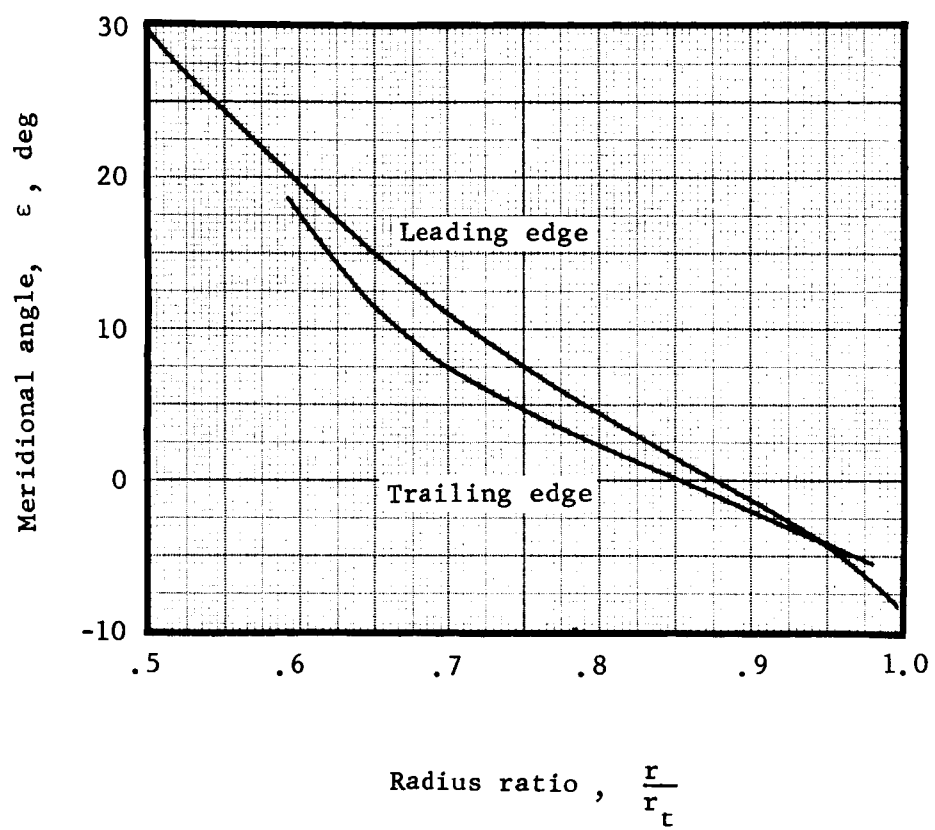


Figure 19. - Radial variation of Rotors 2 design streamline meridional angle.

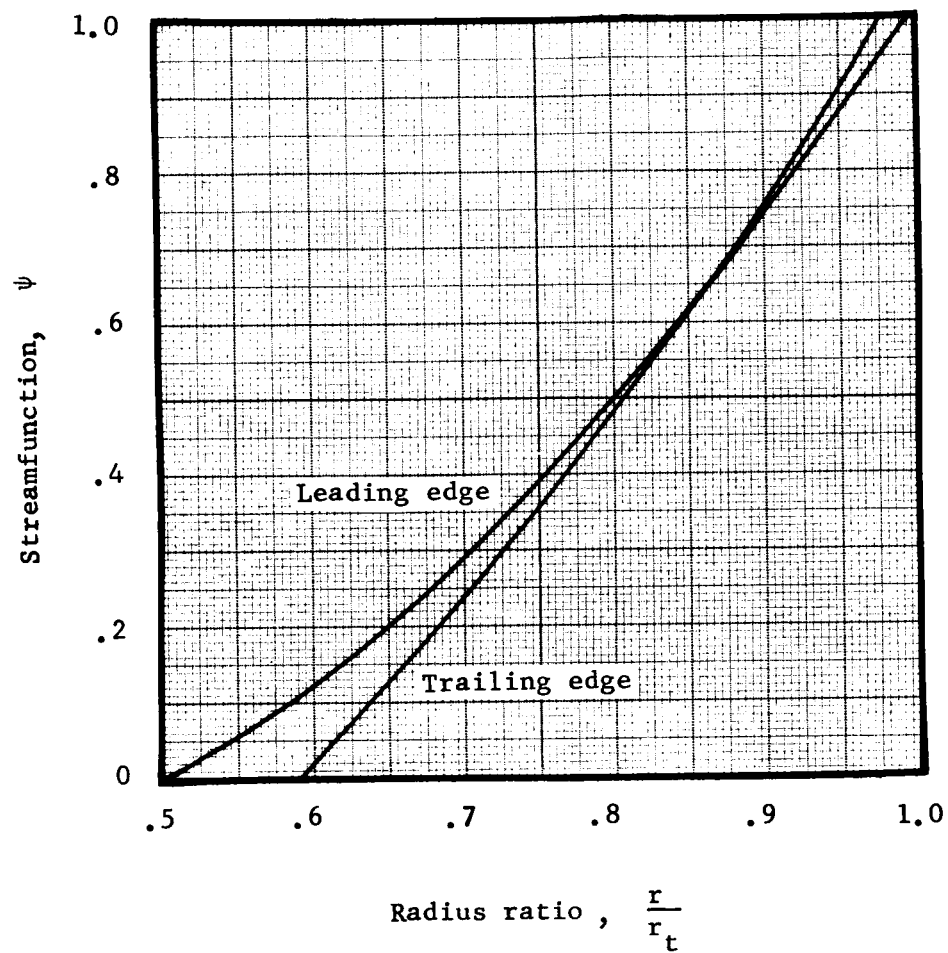


Figure 20. - Radial variation of Rotors 2 design streamfuction.

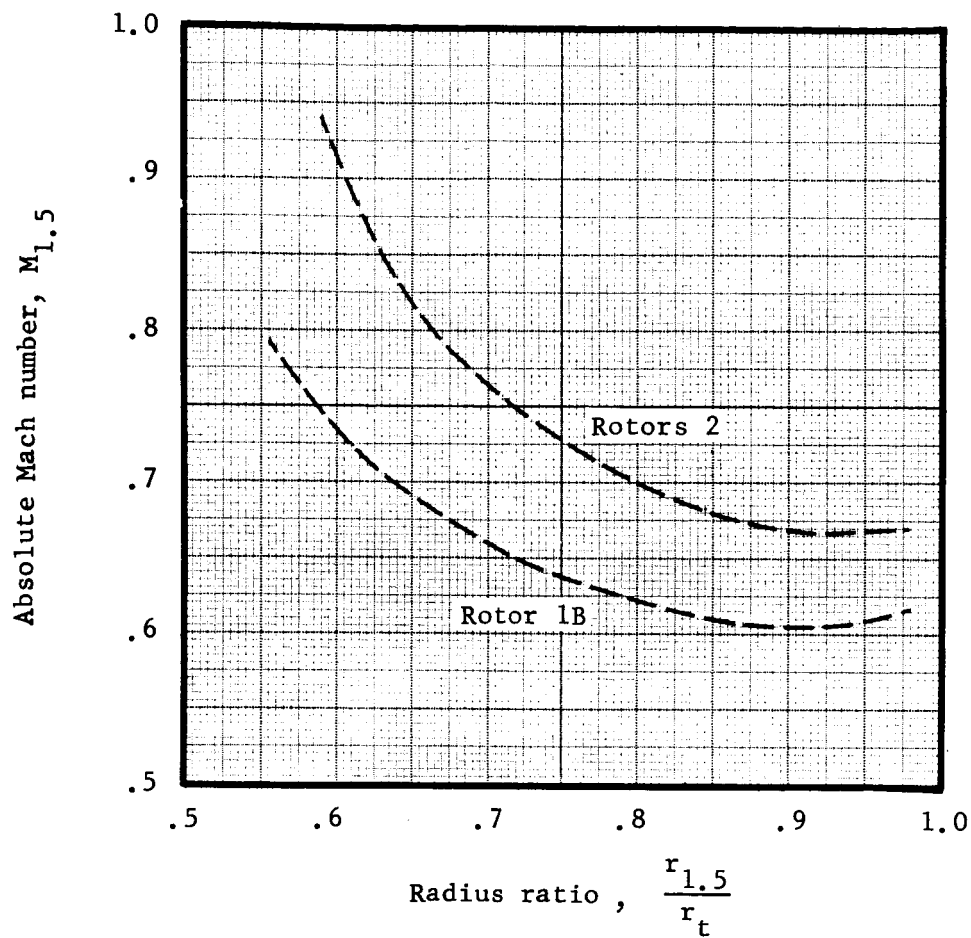


Figure 21. - Radial variation rotor exit absolute Mach number.

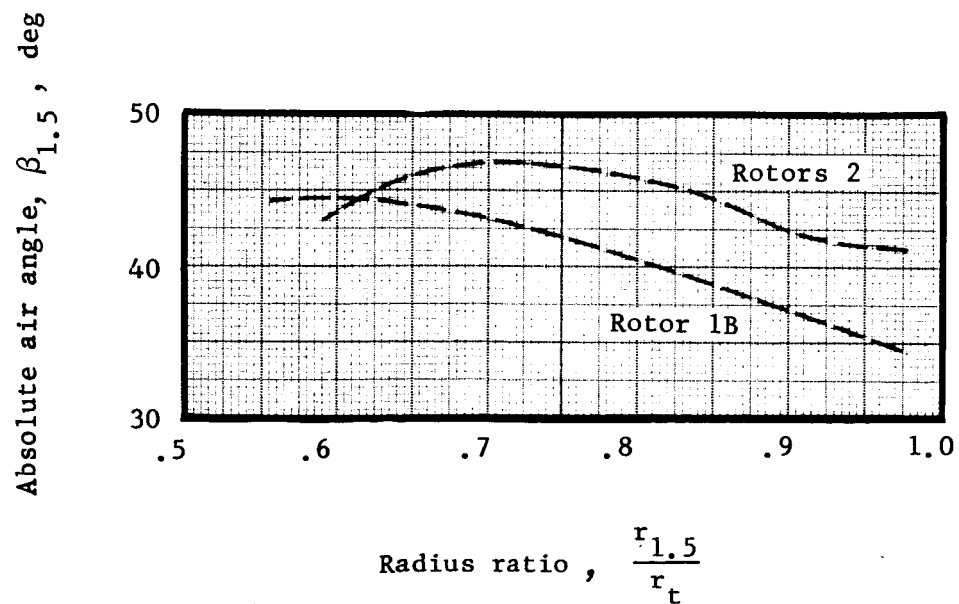


Figure 22. - Radial variation rotor exit absolute air angle.

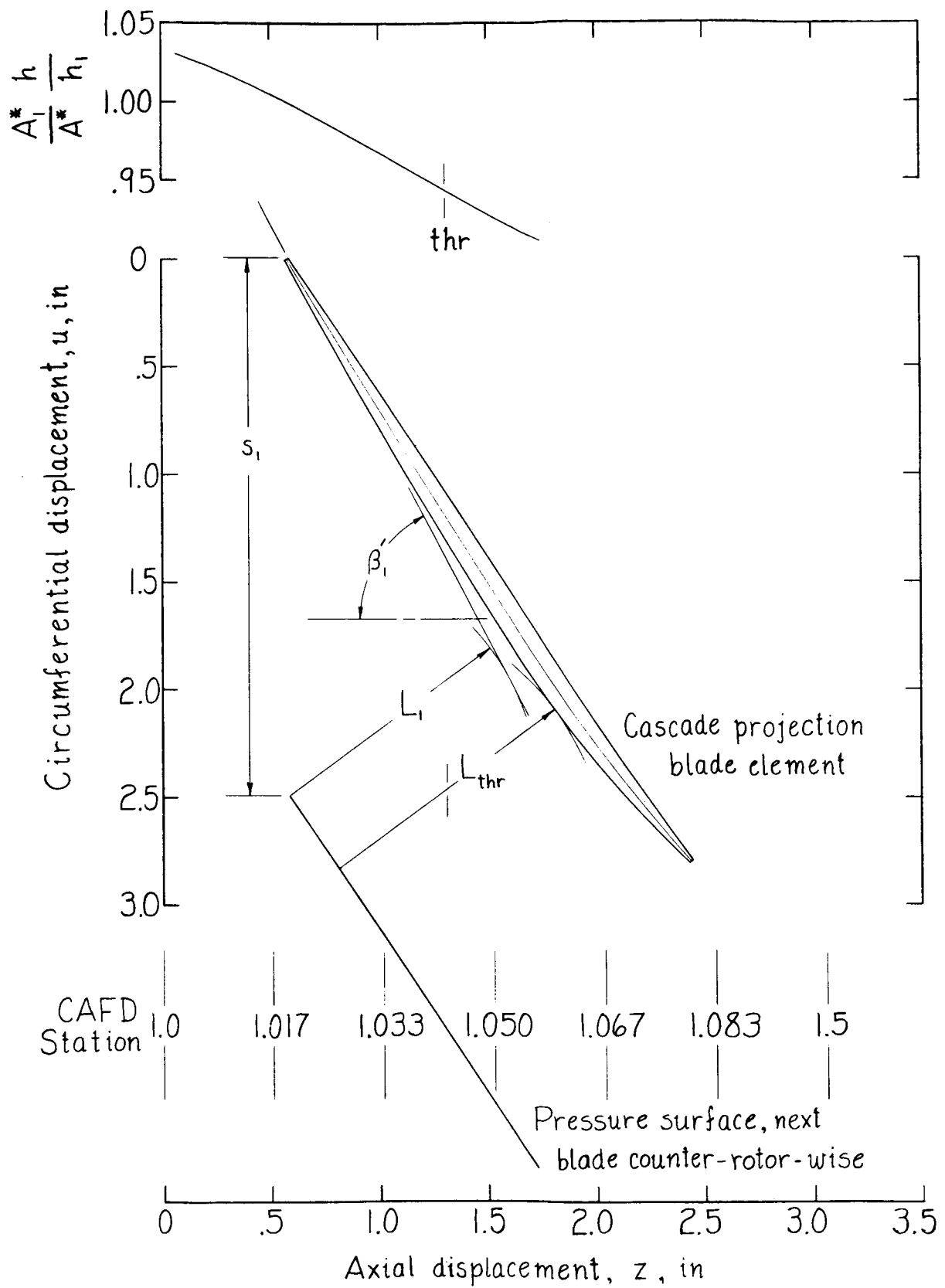


Figure 23. - Typical cascade projection layout

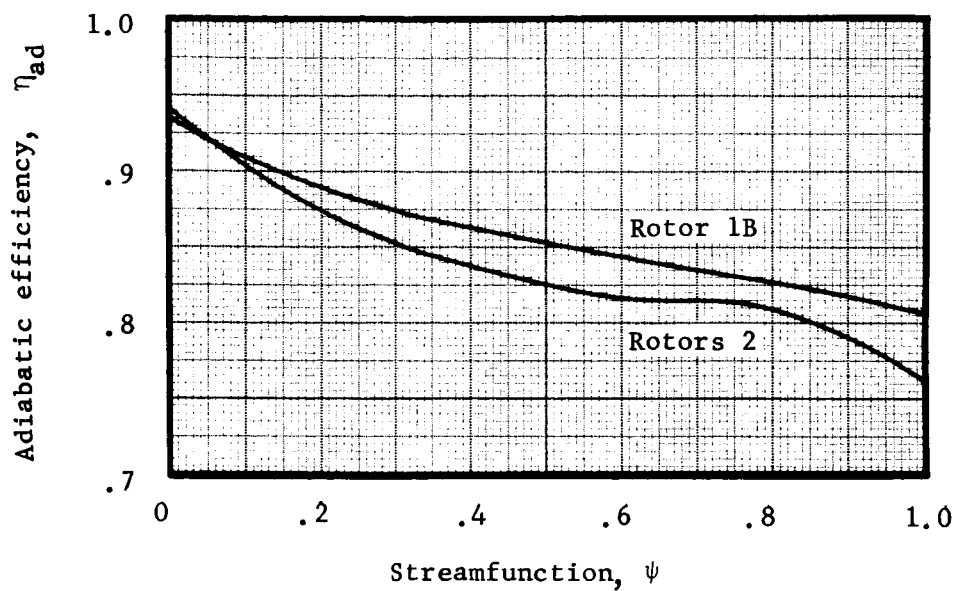


Figure 24. - Radial variation of design adiabatic efficiency.

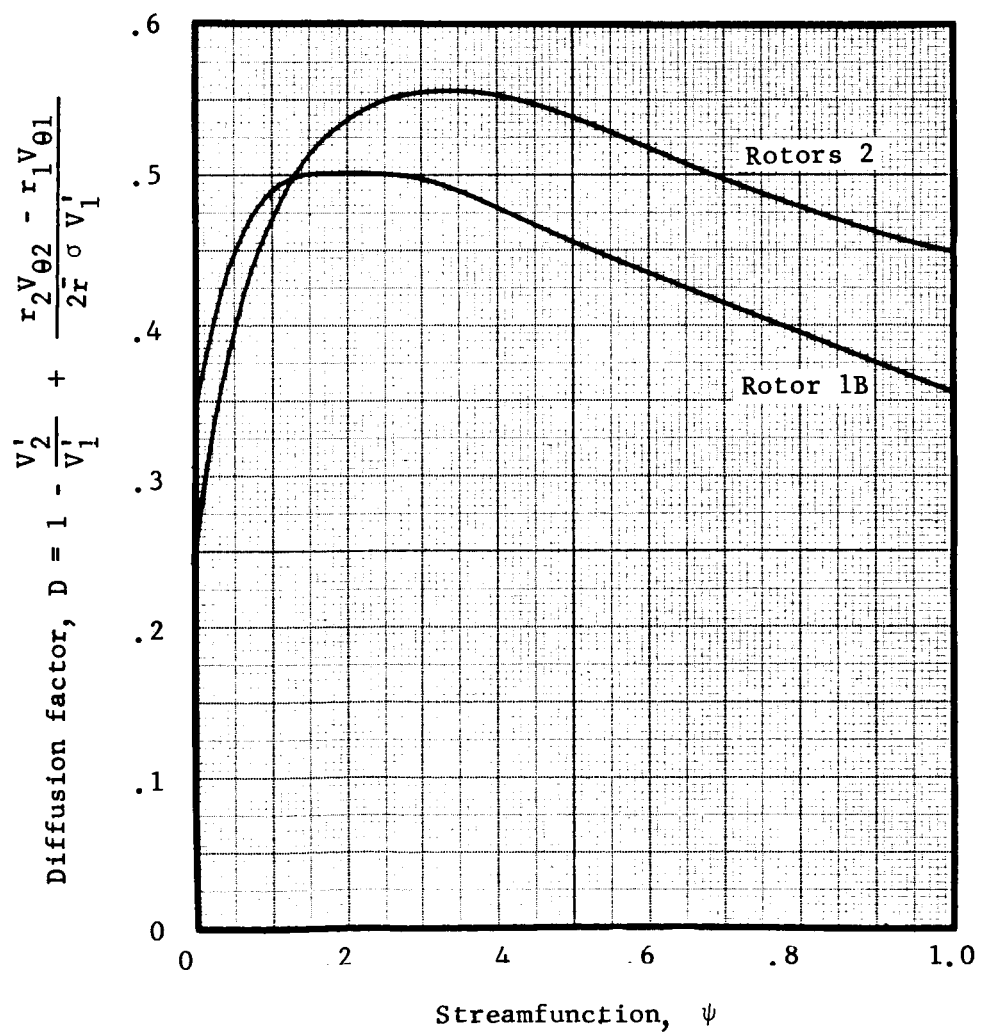


Figure 25. - Radial variation of design diffusion factor.

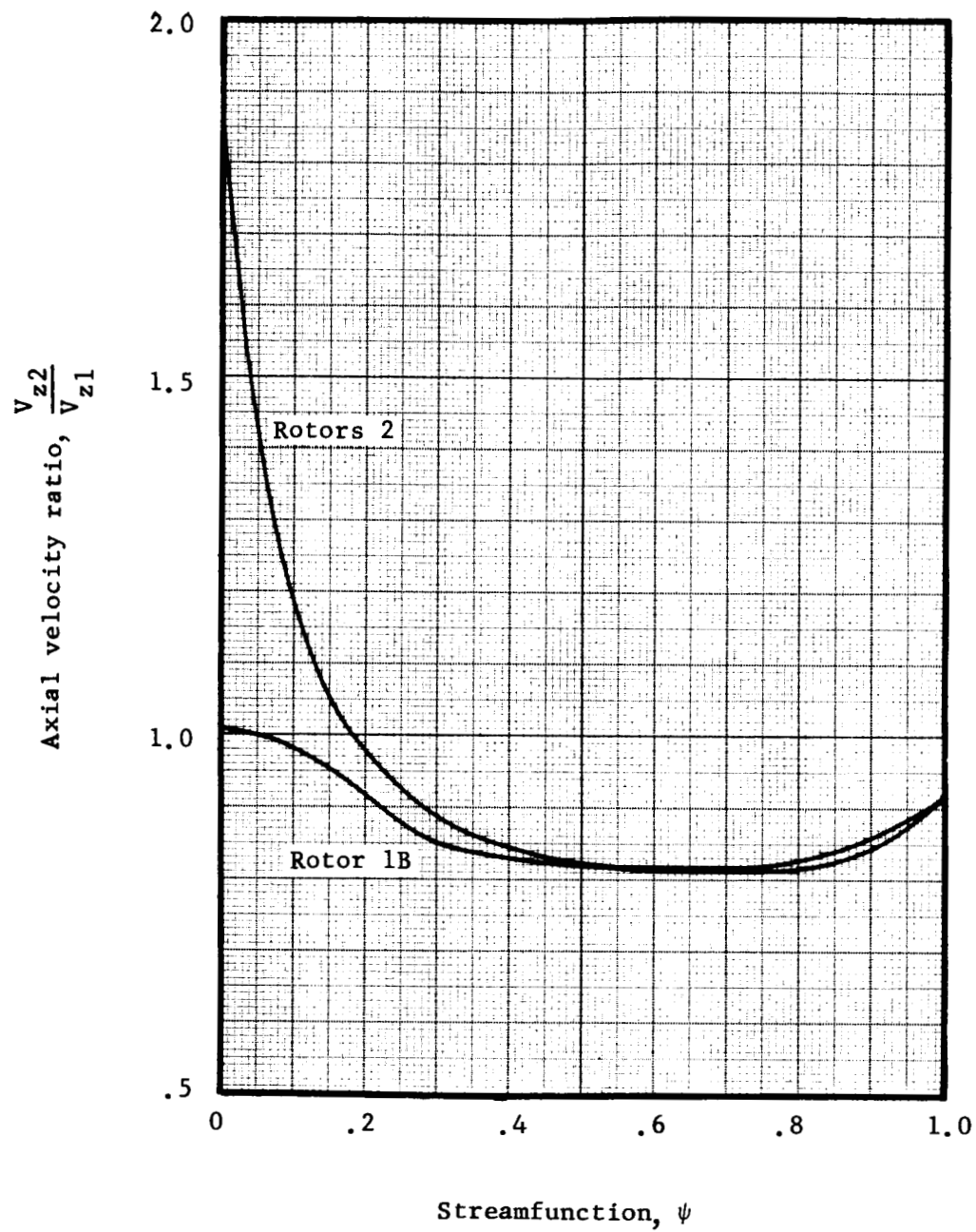


Figure 26. - Radial variation of design axial velocity ratio.

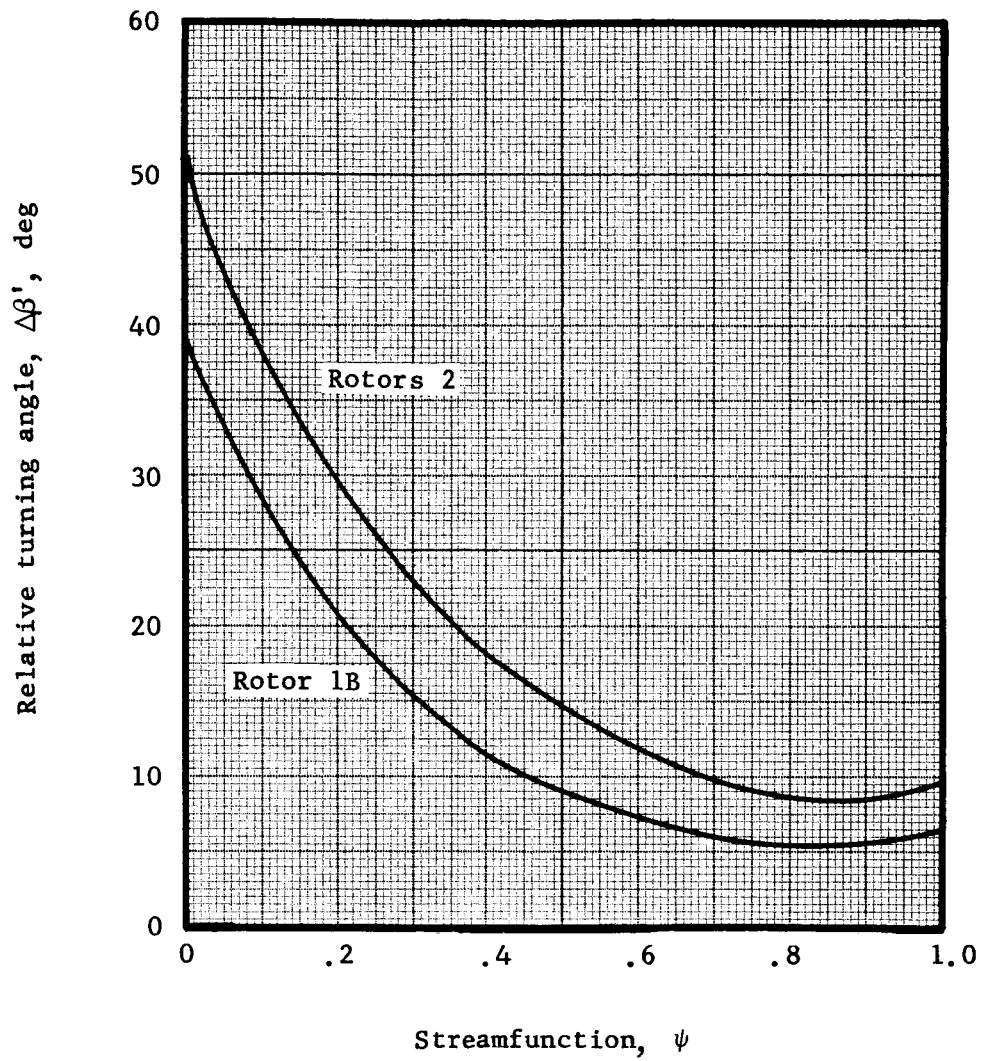


Figure 27. - Radial variation of design relative turning angle.

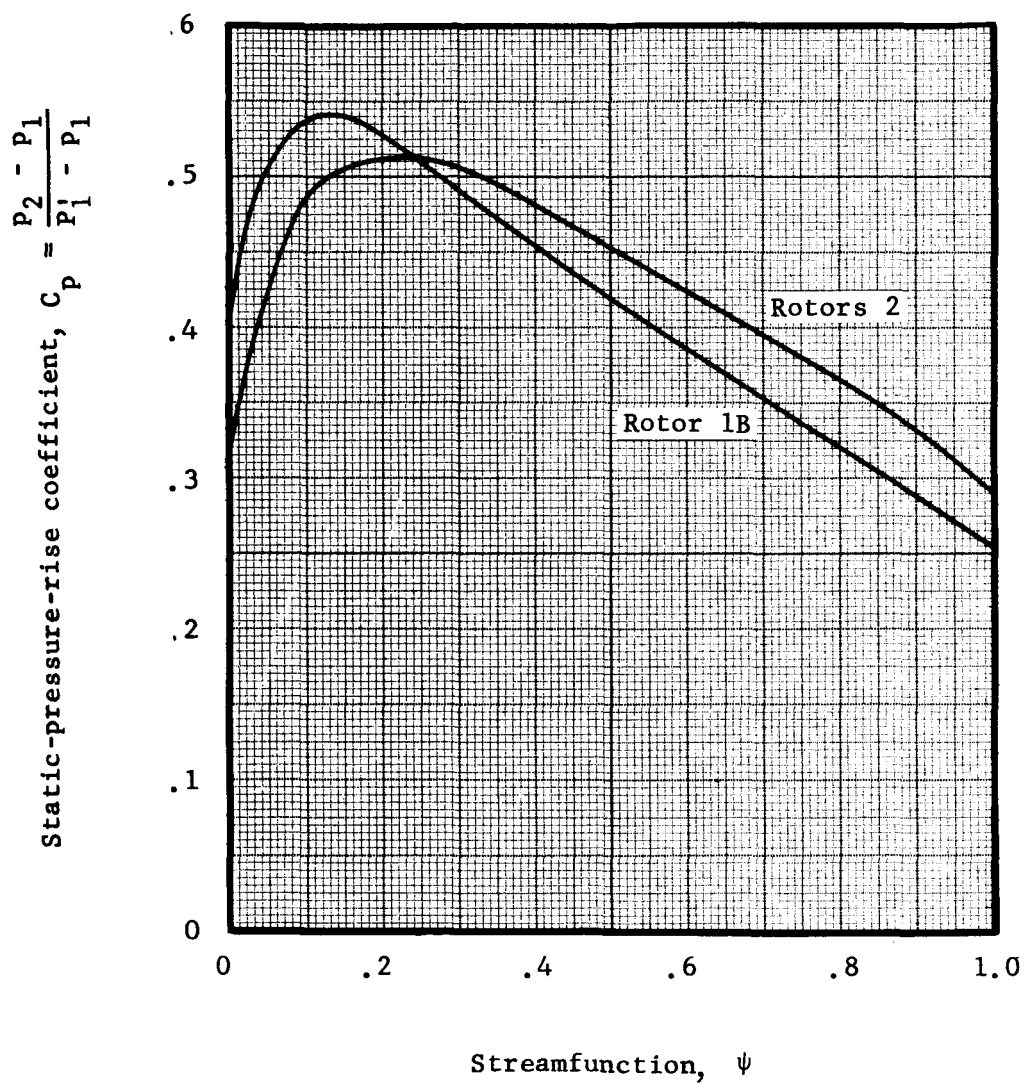


Figure 28. - Radial variation of design static-pressure-rise coefficient.

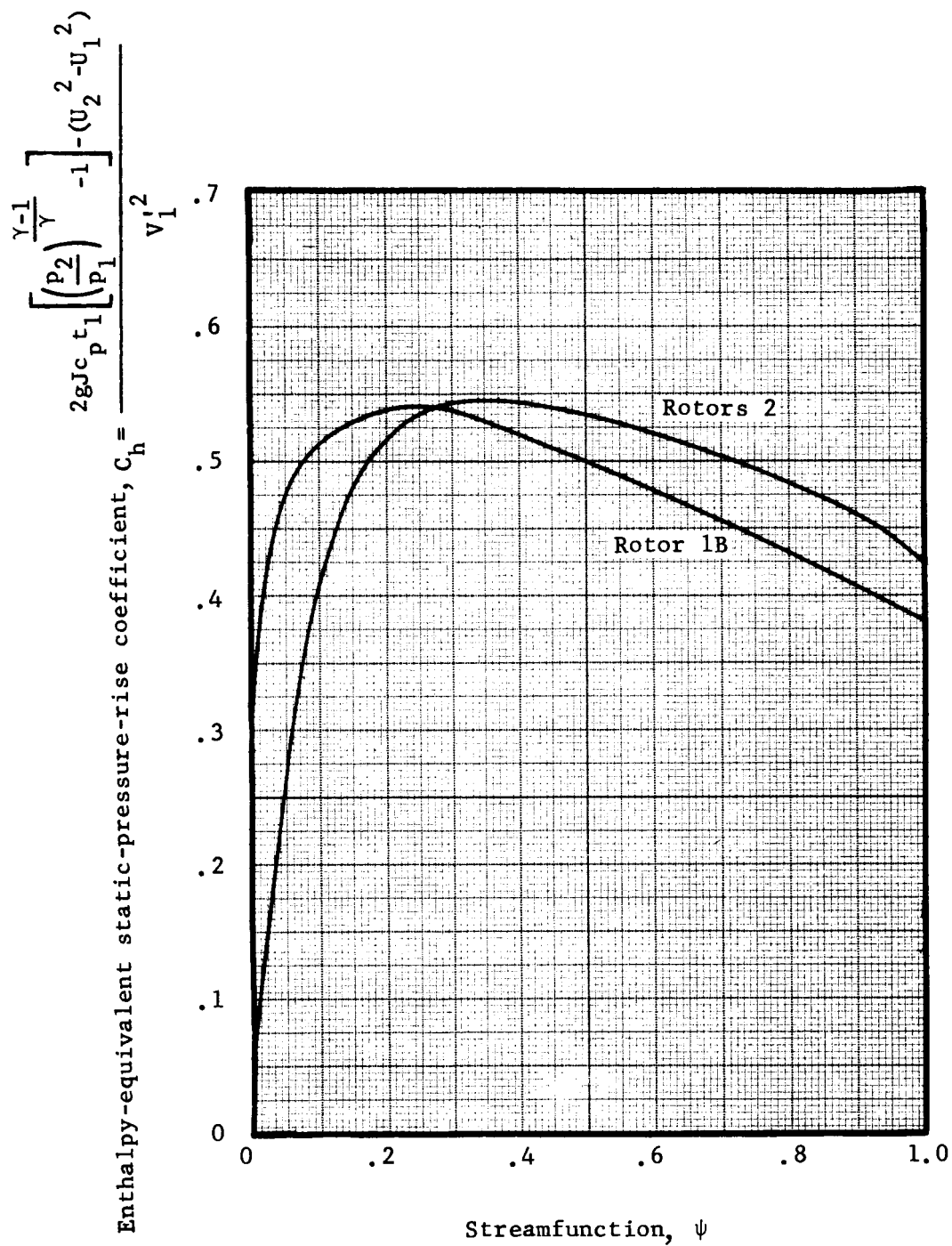


Figure 29. - Radial variation of design enthalpy-equivalent static-pressure-rise coefficient.

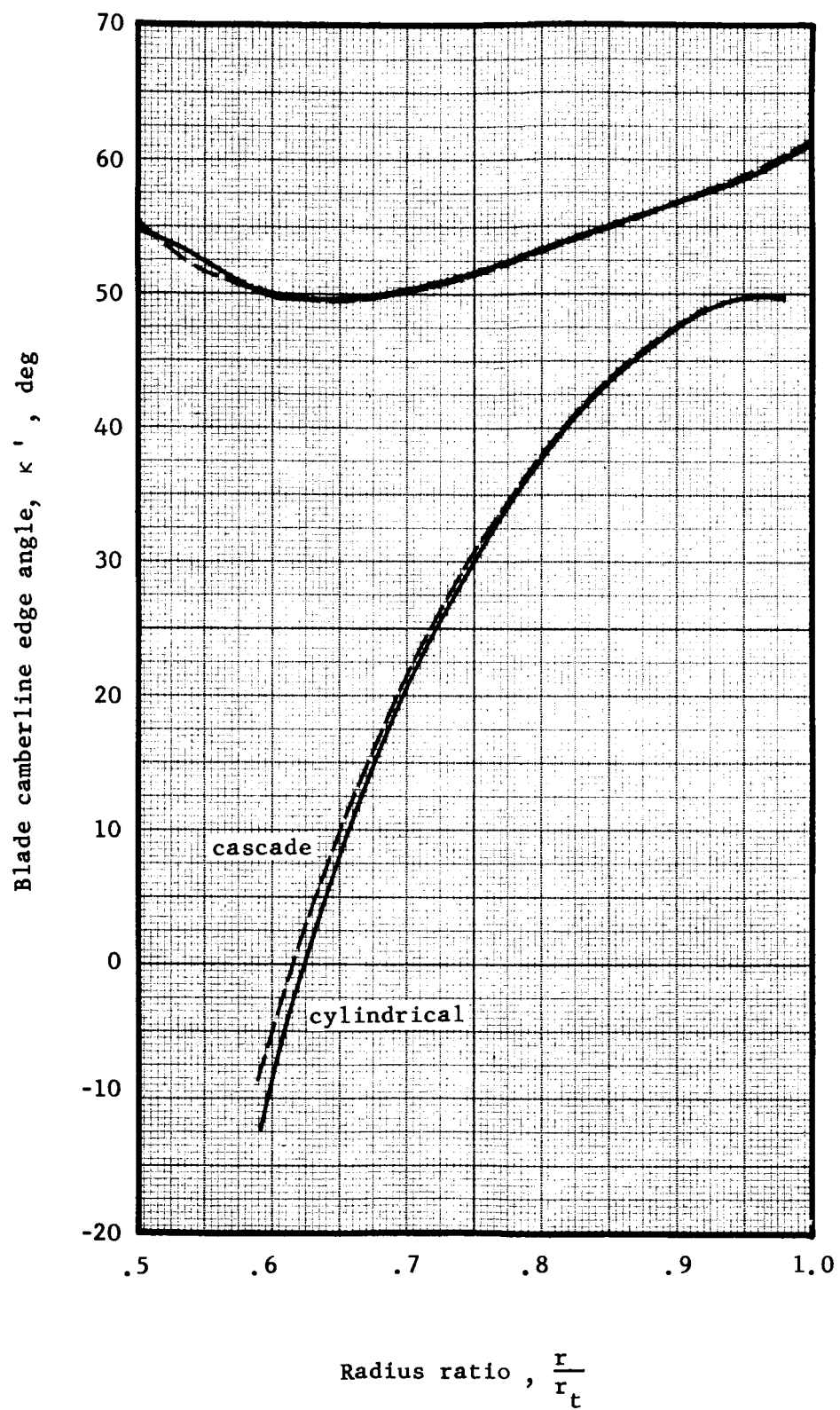


Figure 30. - Comparison of typical cascade and cylindrical edge angles.

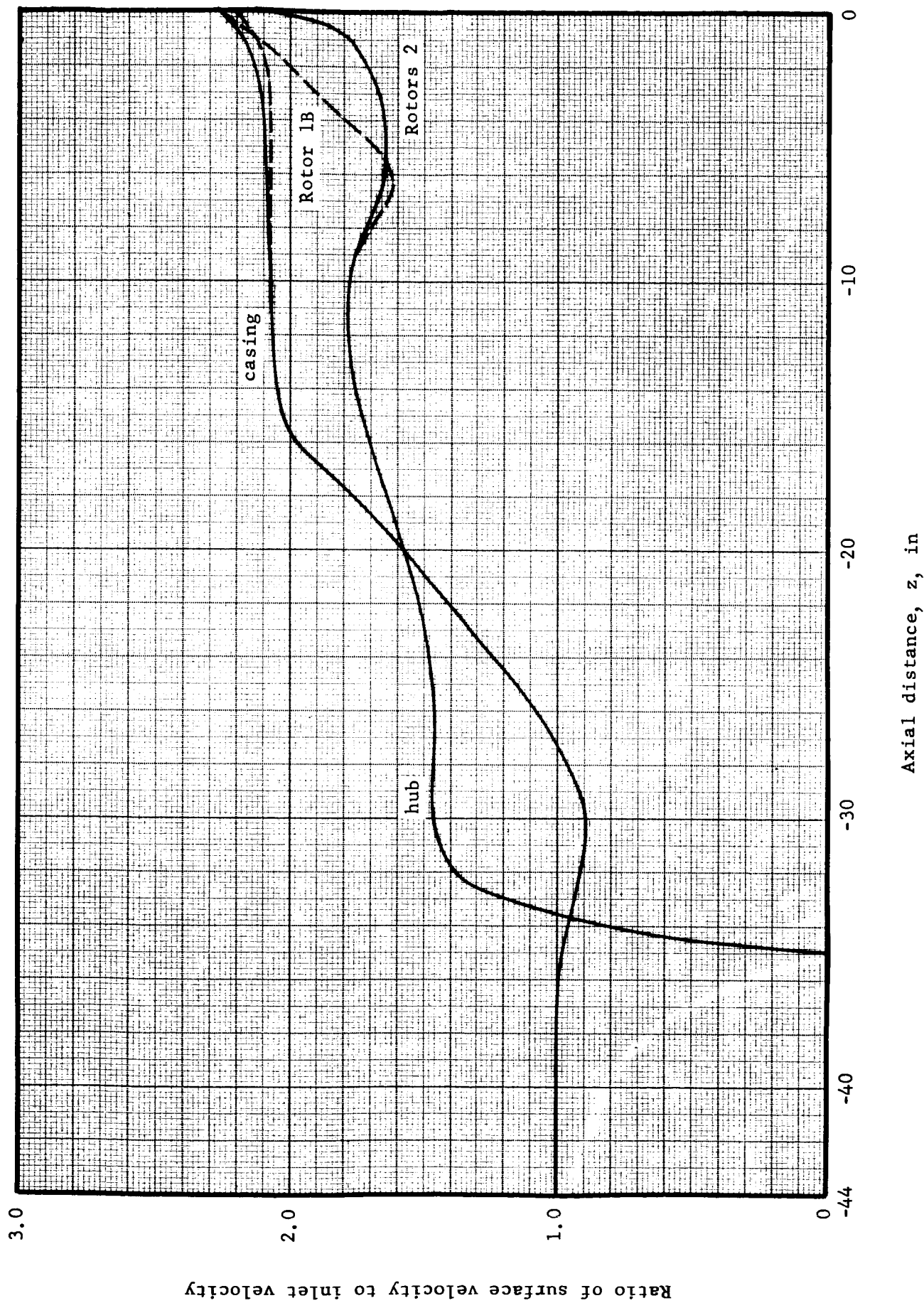
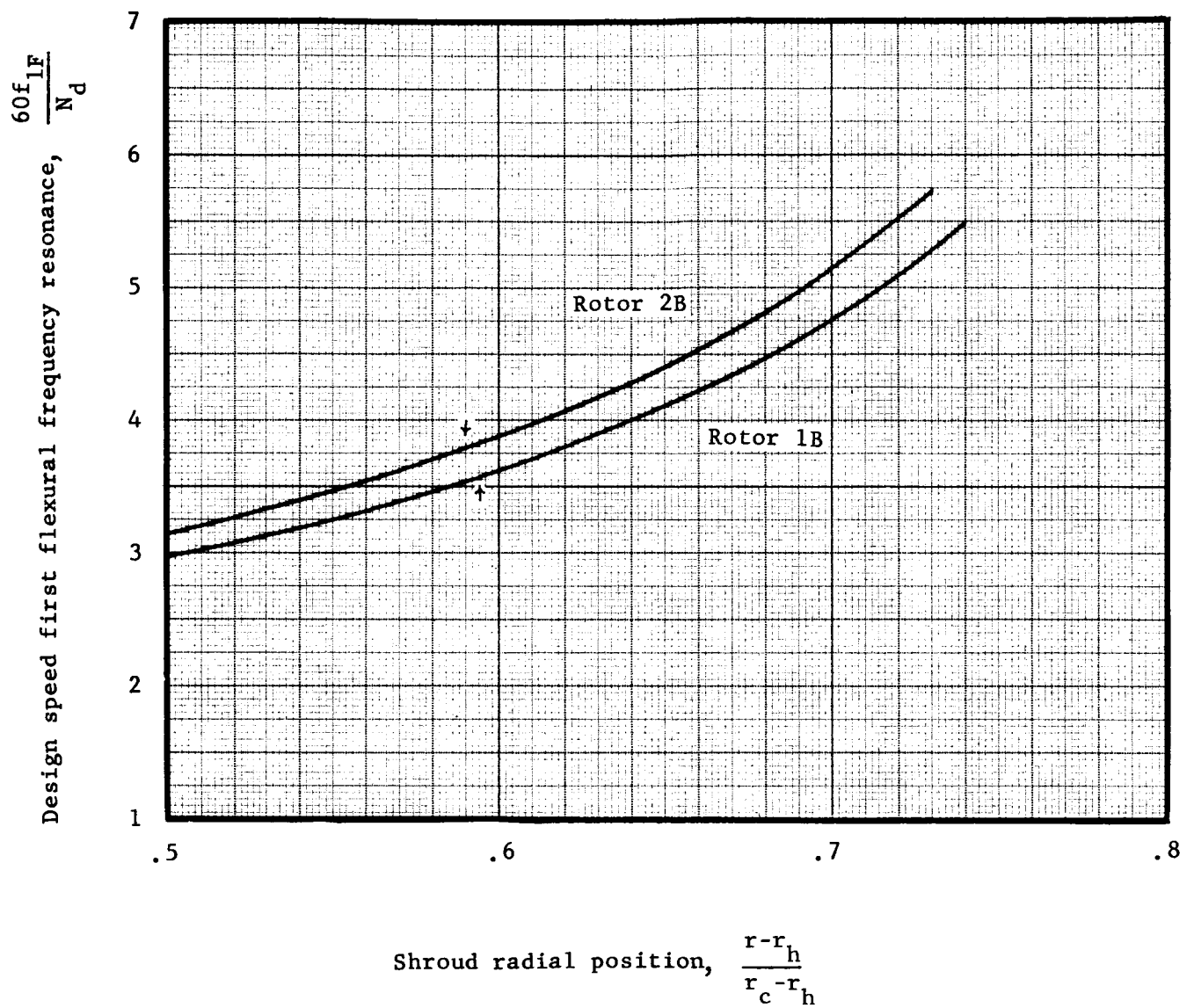
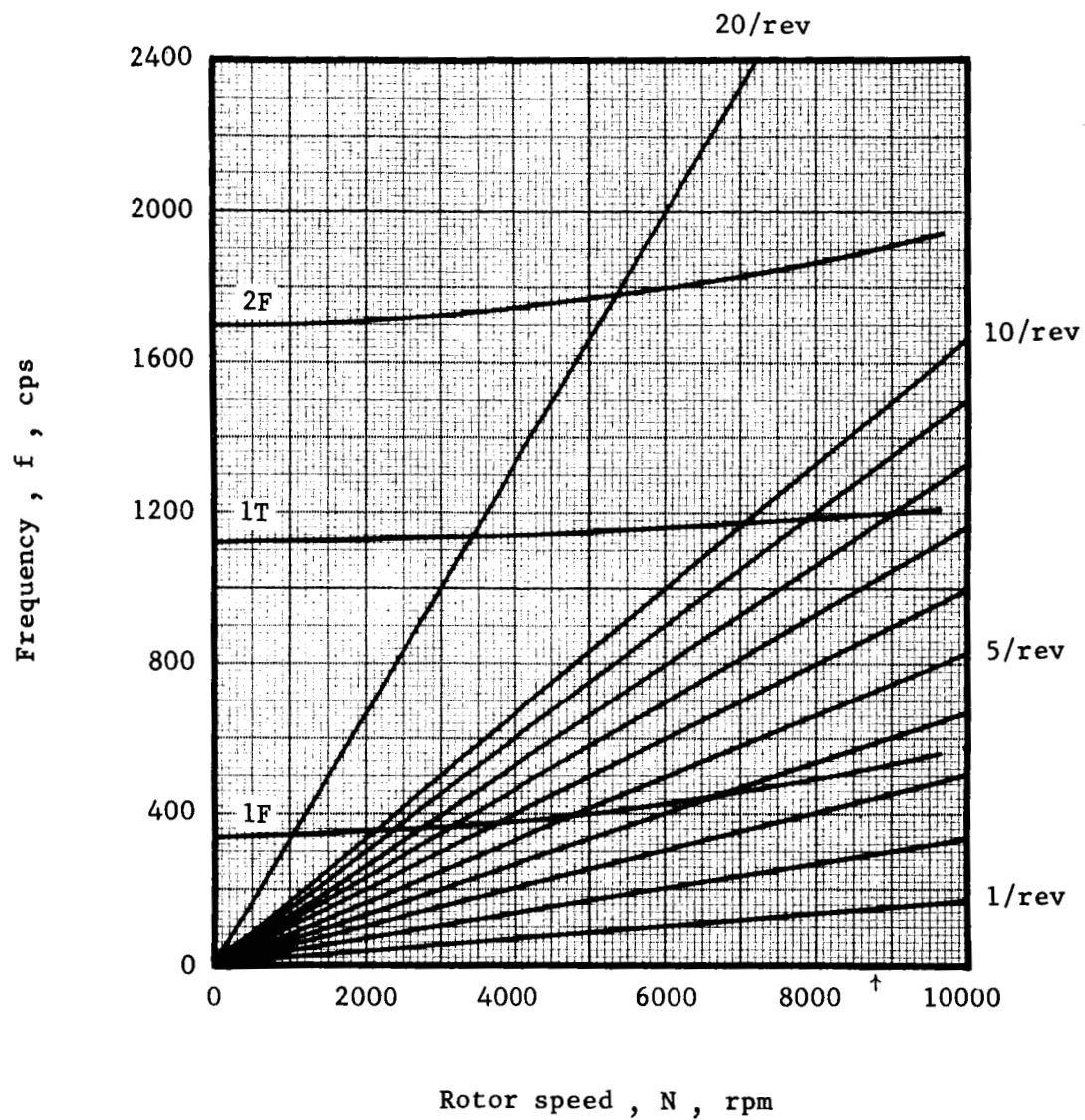


Figure 31. - Surface velocity distribution through inlet contraction region.
(Incompressible axisymmetric solution)



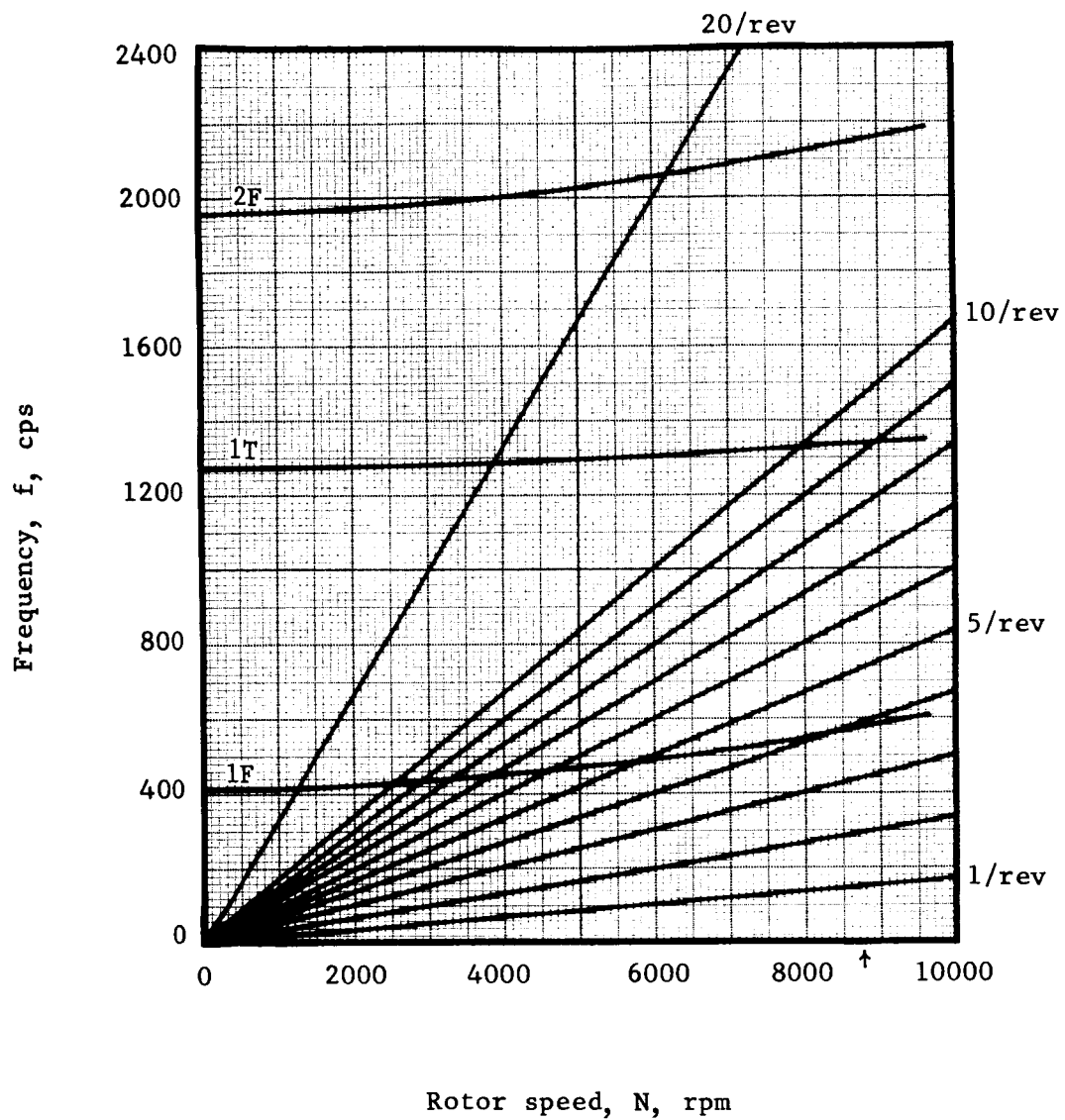
1F = 1st. flexural frequency
 ↑ selected position

Figure 32. - Part-span shroud position selection.



1F = 1st. flexural frequency
 1T = 1st. torsional frequency
 2F = 2nd. flexural frequency
 ↑ = design speed (8791 rpm)

Figure 33. - Rotor 1B Campbell diagram.



1F = 1st. flexural frequency
 1T = 1st. torsional frequency
 2F = 2nd. flexural frequency
 ↑ = design speed (8791 rpm)

Figure 34. - Rotor 2B Campbell diagram.

REPORTS DISTRIBUTION LIST FOR
SINGLE STAGE EXPERIMENTAL EVALUATION OF
HIGH MACH NUMBER COMPRESSOR ROTOR BLADING

CONTRACT NAS3-7617

1. NASA-Lewis Research Center	
21000 Brookpark Road	
Cleveland, Ohio 44135	
Attention: Report Control Office MS 5-5	1
Technical Utilization Office MS 3-19	1
Library MS 60-3	1
Fluid System Component Division MS 5-3	1
Pump & Compressor Branch MS 5-9	6
I.I. Pinkel MS 5-3	1
A. Ginsburg MS 5-3	1
P. Hacker MS 5-3	1
M.J. Hartmann MS 5-9	1
W.A. Benser MS 5-9	1
D.M. Sandercock MS 5-9	1
L.J. Herrig MS 5-9	1
C.L. Ball MS 5-9	1
J. Howard Childs MS 60-4	1
Dr. W.H. Roudebush MS 60-6	1
J.H. Deford MS 60-5	1
S. Lieblein MS 7-1	1
Projects Branch MS 60-6	16
L. Macioce MS 60-6	1

W. Beede MS 60-6	1
J. McAulay MS 60-6	1
2. NASA Scientific & Technical Information Facility P.O. Box 33 College Park, Maryland 20740 Attention: NASA Representative	6
3. FAA Headquarters 800 Independence Avenue, SW Washington, D.C. 20553 Attention: Brig. General J.C. Maxwell F.B. Howard	1 1
4. NASA Headquarters Washington, D.C. 20546 Attention: N.F. Rekos (RAP)	1
5. U.S. Army Aviation Material Laboratory Fort Eustis, Virginia Attention: John White	1
6. Headquarters Wright Patterson AFB, Ohio 45433 Attention: J.L. Wilkins, SESOS S. Kobelak, APTP R.P. Carmichael, SESSP	1 1 1
7. Department of the Navy Bureau of Weapons Washington 25, D.C. Attention: Robert Brown, RAPPl4	1
8. Department of the Navy Bureau of Ships Washington, D.C. 20360 Attention: G.L. Graves	1
9. NASA-Langley Research Center Technical Library Hampton, Virginia 23365 Attention: Mark R. Nichols John V. Becker	1 1

10. Pratt & Whitney Aircraft
Florida Research & Development Center
P.O. Box 2691
West Palm Beach, Florida 33402
Attention: R.A. Schmidtke 1
C.L. Joslin 1
W.R. Alley 1
B.N. Torrel 1
B.A. Jones 1
B.S. Saven 1
11. Pratt & Whitney Aircraft
400 Main Street
East Hartford, Connecticut
Attention: J.A. Fligg 1
A.W. Stubner 1
W.D. Harshbarger 1
P. Tramm 1
M.J. Keenan 1
B.B. Smyth 1
12. Allison Division, GMC
Dept. 8894, Plant 8
P.O. Box 894
Indianapolis, Indiana 46206
Attention: J.N. Barney 1
R.H. Carmody 1
G.E. Holbrook 1
B.A. Hopkins 1
M.L. Miller 1
Library 1
13. Northern Research & Engineering
219 Vassar Street
Cambridge 39, Massachusetts
Attention: R.A. Novak 1
K. Ginwala 1
14. General Electric Company
Flight Propulsion Division
Cincinnati, Ohio 45215
Attention: J.W. Blanton J-19 1
W.G. Cornell K-49 1
J.R. Erwin J-162 1
E.E. Hood/J.C. Pirtle J-165 1
J.F. Klapproth H-42 1
J.W. McBride H-44 1

14. General Electric Company (Cont.)
Flight Propulsion Division
Cincinnati, Ohio 45215
Attention: L.H. Smith H-50 1
S.N. Suci H-32 1
J.B. Taylor J-168 1
Technical Information Center N-32 1
15. General Electric Company
1000 Western Avenue
West Lynn, Massachusetts
Attention: D.P. Edkins Bldg. 2-40 1
F.F. Ehrich Bldg. 2-40 1
L.H. King Bldg. 2-40 1
R.E. Neitzel Bldg. 2-40 1
Dr. C.W. Smith Library Bldg. 2-40M 1
16. Curtiss-Wright Corporation
Wright Aeronautical
Woodridge, New Jersey
Attention: S. Lombardo 1
B. Provenzale 1
J. Wiggins 1
17. Air Research Manufacturing Company
402 South 36th Street
Phoenix, Arizona 85034
Attention: Robert O. Bullock 1
John H. Daman 1
18. Air Research Manufacturing Company
8951 Sepulveda Boulevard
Los Angeles, California 90009
Attention: L.C. Wright 1
19. Avco Corporation
Lycoming Division
550 South Main Street
Stratford, Connecticut
Attention: Clause W. Bolton 1
20. Continental Aviation & Engineering Corporation
12700 Kercheval
Detroit, Michigan 48215
Attention: Eli H. Benstein 1
Howard C. Wasch 1

21. Solar
San Diego, California 92112
Attention: P.A. Pitt 1
Mrs. L. Walper 1
22. Goodyear Atomic Corporation
Box 628
Piketon, Ohio
Attention: C.O. Langebrake 2
23. Iowa State University of Science and Technology
Department of Mechanical Engineering
Ames, Iowa 50010
Attention: Professor George K. Serovy 1
24. Pennsylvania State University
233 Hammond Building
University Park, Pennsylvania 16802
Attention: B. Lakshmenarayana 1
25. The Boeing Company
Commercial Airplane Division
P.O. Box 3991
Seattle, Washington 98124
Attention: G.J. Schott, M.S. 80-66 1
26. Union Carbide Corporation
Nuclear Division
Oak Ridge Gaseous Diffusion Plant
P.O. Box "P"
Oak Ridge, Tennessee 37830
Attention: R.G. Jordan 1